

**Gallium Nitride, Indium Nitride, and  
Heterostructure Development Using  
The MEAglow Growth System**

A thesis presented by

Peter W. Binsted

to

The Faculty of Science and Environmental Studies

in partial fulfillment of the requirements

for the degree of

Doctor of Philosophy

in the subject of

Chemistry and Materials Science

Lakehead University

Thunder Bay, Ontario

June 2014

# Gallium Nitride, Indium Nitride, and Heterostructure Development Using The MEAglow Growth System

Peter W. Binsted

Thesis Advisor: Dr. Dimiter Alexandrov, Dr. Alla Reznik

## **Abstract**

This thesis presents an in depth study of semiconductor development using a new process termed Migration Enhanced Afterglow (MEAglow). The MEAglow growth reactor is housed in the Lakehead University Semiconductor Research Lab. Thin films of gallium nitride and indium nitride are produced as well as heterostructures comprised of these two films and their ternary alloy InGaN. MEAglow is a form of plasma enhanced chemical vapour deposition (PECVD) employing migration enhanced epitaxy (MEE). The heterostructure is being developed for a novel field effect transistor (FET) based on the tunnelling of charge carriers which alter the channel conductivity. The configuration of this unique III-Nitride device should allow the FET to function as normally off in either n-type or p-type operation. Due to the difficulties in growing low temperature GaN, test devices of this abstract design were not previously possible. Further details on the device operation and growth parameters are included.

Samples produced by the research reactor were characterised through x-ray diffraction (XRD), ultraviolet-near infrared-visible spectroscopy (UV-Vis-NIR), Auger spectroscopy, scanning electron microscopy (SEM), and atomic force microscopy (AFM).

Film growth is accomplished by an improved form of pulsed delivery Plasma Enhanced Chemical Vapour Deposition (PECVD). The reactor features a scalable hollow cathode type plasma source.

Data obtained through characterisation is subjected to theoretical treatment which explains much not previously understood behaviour of the GaN films.

Many challenges in III-Nitride film growth have been overcome during this research project. A method of developing structures consisting of InN and GaN within the same system has been proven.

(c) Peter W. Binsted 2014

# Table of Contents

List of Figures .....	ix
List of Tables .....	xiv
Chapter 1 Introduction .....	1
1.1. Group III-V Semiconductors.....	4
1.2. Materials of Interest .....	6
1.2.1. Gallium .....	6
1.2.2. Indium.....	7
1.2.3. Aluminium .....	7
1.2.4. Nitrogen .....	8
1.3. Conclusion.....	8
Chapter 2 Review of Thin Film Deposition.....	11
2.1. Overview .....	11
2.1.1. Challenges in III-Nitride Film Growth .....	12
2.2. Methods of Thin Film Production.....	14

2.2.1.	Physical Vapour Deposition .....	14
2.2.2.	Chemical Vapour Deposition.....	14
2.2.3.	Comparison of Growth Methods .....	15
2.2.4.	MBE .....	15
2.2.5.	MOCVD.....	17
2.2.6.	PECVD .....	18
2.2.7.	MEAglow.....	18
2.2.8.	MOVPE.....	19
2.3.	Precursors.....	20
2.3.1.	Trimethylgallium (TMG).....	21
2.3.2.	Trimethylindium (TMI) .....	21
2.3.3.	Trimethylaluminium (TMA).....	22
2.3.4.	Magnesium.....	22
2.4.	Plasma .....	22
2.4.1.	Definition of a Plasma .....	23
2.4.2.	Advantages of Using a Plasma .....	24
2.4.3.	Plasma Application in Film Deposition Systems.....	24
2.4.4.	Types of Plasmas .....	25
2.5.	Buffer Layers.....	32
2.6.	Growth Regimes.....	33

2.7.	Nitridation .....	34
2.8.	Sample Preparation .....	34
2.9.	Substrates .....	35
2.9.1.	Silicon (Si) .....	36
2.9.2.	Sapphire .....	36
2.9.3.	Silicon Carbide (SiC).....	36
Chapter 3 Compounds of Interest .....		37
3.1.	Review of III-Nitrides .....	37
3.2.	Gallium Nitride .....	39
3.3.	Indium Nitride .....	40
3.4.	Aluminum Nitride .....	41
Chapter 4 Single Film and Heterostructure Film Growth by MEAglow .....		43
4.1.	Introduction .....	43
4.1.1.	The MEAglow Reactor .....	43
4.1.2.	The Gas Delivery System .....	46
4.2.	Operation of the MEAglow Reactor .....	47
4.2.1.	Temperature Calibration .....	47
4.2.2.	Chamber Preparation .....	48
4.2.3.	Sample Loading .....	49
4.2.4.	Program Operation.....	49

4.2.5.	Sample Extraction.....	54
4.3.	Gallium Nitride Film Growths.....	54
4.3.1.	General Gallium Nitride Growth.....	55
4.3.2.	GaN Grown Under Various Nitrogen Flux.....	58
4.3.3.	GaN Buffer Layers.....	64
4.3.4.	GaN Grown with Desorption Step.....	68
4.3.5.	GaN Grown Under Various TMG Flows.....	72
4.3.6.	GaN Grown Under Varying Plasma Only Time.....	79
4.4.	Indium Nitride Film Growth.....	84
4.4.1.	General Indium Nitride Growth.....	84
4.4.2.	InN Grown Under Various Plasma Only and Plasma + Setup Times.....	91
4.4.3.	InN Grown Under Various TMI Times.....	95
4.5.	Heterostructure Growth.....	101
4.5.1.	Initial Heterostructure Growths.....	101
4.5.2.	Further Heterostructure Growths.....	108
4.6.	Nanostructure Growths.....	114
4.6.1.	Experiment.....	114
4.6.2.	Discussion.....	115
4.6.3.	Results.....	116
	Chapter 5 Contact Deposition.....	117

Chapter 6 Film Analysis and Characterisation .....	121
6.1. Atomic Force Microscopy (AFM) .....	122
6.2. Hall Effect .....	123
6.3. Scanning Electron Microscopy (SEM) .....	124
6.4. Spectroscopy (UV-Vis) .....	125
6.5. X-Ray Diffraction (XRD) .....	127
Chapter 7 Theoretical Treatment of the Results .....	130
7.1. Calculation of the electron band structure of compound semiconductor alloys	
130	
7.1.1. Electron Band Structure of a Generic Crystal $A_xB_{1-x}C$ where (A and B are cationic atoms, and C is anionic atom)[67] .....	131
7.1.2. Electron Band Structure of a GaN Crystal with Defects .....	137
7.1.3. Optical properties of $GaA_yN_{1-y}$ .....	143
7.2. Structure of Isolated Oxygen Impurity States in GaN .....	145
7.2.1. Electron Band Structures of wurtzite $GaO_yN_{1-y}$ and of Non-Stoichiometric Ga:GaN	
146	
7.2.2. Electronic Structures of Isolated Oxygen Impurity States.....	149
7.3. Optical Absorption Spectra of GaN .....	153
Chapter 8 Conclusion.....	158
Chapter 9 References .....	161

Chapter 10 List of Publications.....	167
Chapter 11 Appendix .....	168
11.1. Sample Loading Procedure.....	168
11.2. Sample Unloading Procedure .....	169
11.3. Sample Baking Procedure .....	170
11.4. Chamber Cleaning .....	171
11.5. Procedure for Use of RGA During Growth.....	172
11.6. Procedures for Using RHEED System .....	173
11.6.1. Turning on RHEED system.....	173
11.6.2. Putting on Standby .....	173
11.6.3. Taking off Standby.....	173
11.6.4. Turning off RHEED system .....	173
11.7. Sample Etching.....	174

## List of Figures

Figure 1. The Langmuir probe setup used to obtain measurements[21].....	31
Figure 2. IV characteristics obtained by Langmuir probe measurements. (a) in linear form (b) by natural log. The vertical line indicates the plasma potential. ....	32
Figure 3. The MEAglow growth system model 0001.....	44
Figure 4. MEAglow System Gas Delivery System. ....	46
Figure 5. Temperature calibration data from March 6, 2012.....	48
Figure 6. Generalized metal modulated single film GaN growth. ....	51
Figure 7. Generalized InN film growth.....	53
Figure 8. 4 $\mu$ m x 4 $\mu$ m AFM Scan of 2011-06-13-1-GaN.....	57
Figure 9. XRD scan showing GaN sample with a FWHM of 0.1152. ....	58
Figure 10. Chamber Pressure vs. Nitrogen Flow for this series of experiments. ....	60
Figure 11. AFM scans showing surface morphology. ....	61
Figure 12 Growth rate and surface roughness for non-titanium backed samples vs. nitrogen flux.....	63
Figure 13. SEM images showing the profile and surface of one sample with a measured RMS surface roughness of 386 $\mu$ m. ....	65
Figure 14. AFM scan of the resulting buffer layer. ....	66
Figure 15. (a) SEM image showing a scratch on the sample shown in Figure 13. (b) The refined film showing less defects.....	67

Figure 16. XRD scan with FWHM of 0.1536 °2-theta. ....	69
Figure 17. Modified GaN film growth flow chart showing desorption step. ....	70
Figure 18. A correlation exists between the sample growth rate and resulting surface roughness. ....	71
Figure 19. Surface roughness results from various TMG flows. ....	73
Figure 20. AFM image of sample growth with 2.7 sccm of TMG. ....	74
Figure 21. AFM image of sample grown with 2.8 sccm of TMG. ....	74
Figure 22. AFM image of sample grown with 2.9 sccm of TMG. ....	75
Figure 23. AFM image of sample grown with 3.0 sccm of TMG. ....	75
Figure 24. AFM image of sample grown with 3.2 sccm of TMG. ....	76
Figure 25. Resulting surface roughness for thicker films. ....	77
Figure 26. AFM scans for (a) 2.2 sccm of TMG flow, (b) 2.25 sccm, and (c) 2.3 sccm..	78
Figure 27. Resulting XRD FWHM for the various MO duty cycles. ....	80
Figure 28. AFM scan for the 4.5 s plasma only time (0.87% duty cycle) sample.....	81
Figure 29. AFM scan for the 5.5 s plasma only time (0.85% duty cycle) sample.....	81
Figure 30. AFM for 7.5 s plasma only time (80% duty cycle). ....	82
Figure 31. Resulting band gap values. ....	83
Figure 32. XRD for 2012-01-24-3-InN showing a FWHM of 0.1152 °2-theta.....	86
Figure 33. AFM for 2012-01-24-3-InN with a surface roughness of 3,715 nm.....	
86	
Figure 34. Resulting surface roughness for the range of growth temperatures. ....	87
Figure 35. Growth rate vs. surface roughness.....	88
Figure 36. Electron mobility vs. concentration for a number of indium nitride samples.	89

Figure 37. Nanowires 2012-04-05-1-InN. .... 90

Figure 38. 2013-05-08-1-InN showing 2D island growth. ....	90
Figure 39. 15s plasma only, 10s plasma + setup time. ....	92
Figure 40. XRD of 15s “Plasma Only” and 10s “Plasma + Setup”.....	93
Figure 41. SEM image of “Plasma + Setup” at 2 seconds.....	93
Figure 42. XRD scan of 2s “Plasma + Setup”. ....	94
Figure 43. “Plasma Only” time reduced to 10 s with 5 s “Plasma + Setup”. ....	95
Figure 44. Resulting growth rate and XRD FWHM for the various metalorganic injection pulse times. ....	97
Figure 45. XRD for sample grown with 13s MO on time. ....	98
Figure 46. (101) InN Relative Intensity. ....	98
Figure 47. SEM profile image for 12s MO on time sample. ....	99
Figure 48. XRD scan of first attempt showing InGa <sub>N</sub> alloy growth with no evidence of GaN buffer layer remaining. ....	103
Figure 49. Formation of InGa <sub>N</sub> on commercial GaN substrate.....	104
Figure 50. XRD graph of sample 3 showing two InGa <sub>N</sub> peaks. ....	105
Figure 51. Sample 3 surface image at 2x magnification.....	106
Figure 52. XRD graph for Sample 4 showing strong peaks for InN and GaN indicating a sharp interface between layers with little InGa <sub>N</sub> present. ....	107
Figure 53. The desired heterostructure. ....	110
Figure 54. AFM scan of the prototype GaN film to be used for the top layer of the heterostructure.....	110
Figure 55. XRD analysis of all the grown heterostructures.....	112

Figure 56. Auger spectroscopy showing the presence of indium nitride at the surface of the sample. ....	113
Figure 57. SEM showing nanowires[5]. ....	115
Figure 58. SEM for 425 cycle samples. (a) film as grown (b) after film has been etched.[5] .....	115
Figure 59. XRD for nanopillar sample[5]. ....	116
Figure 60. Pinhole defects on the heterostructures[53]. (a) initial sample (b) improved sample .....	118
Figure 61. IV characteristics for both samples. ....	118
Figure 62. IV characteristics for the nickel contacts.....	119
Figure 63. Sample Hall effect screen. ....	124
Figure 64. Typical optical transmission data. ....	126
Figure 65. Typical optical density squared plot.....	127
Figure 66. Tunnel Optical Absorption. ....	144
Figure 67. Excitation of the structure. ....	144
Figure 68. Electron band structure for wurtzite $\text{GaO}_y\text{N}_{1-y}$ . Only the sub bands corresponding to the bottom of the conduction band and to the top of the valence band are provided. ....	148
Figure 69. Electron band structure of $\text{GaO}_y\text{N}_{1-y}$ for point only and donor level $E_d = -3.86$ eV (not to scale) .....	149
Figure 70. Electron band structure for wurtzite non-stoichiometric GaN:Ga. Only the sub bands corresponding to the bottom of the conduction band and to the top of the valence band are provided.....	151

Figure 71. Electron band structure of non-stoichiometric GaNLGa for point $\Gamma$ only and donor level (not to scale).....	151
Figure 72. Cluster of GaN and donor level $E_d = -3.79$ eV.....	152
Figure 73. Cluster of GaN and donor level $E_d = -3.86$ eV.....	153
Figure 74. Electron band structure of GaN in k-space only. ....	156

## List of Tables

Table 1. Complete List of Group III-V Binary Compounds.....	5
Table 2. Consolidated material properties for our materials of interest compiled from [8]. .....	6
Table 3. Comparison of Various Growth Techniques[12][21].....	15
Table 4. A comparison of our semiconductors of interest at 300K[42].....	38
Table 5. Comparison of Leading Power Transistor Technologies[40].....	39
Table 6. Nitrogen flow, chamber pressure, and surface roughness for the samples in Figure 11. ....	62
Table 7. Summary of GaN Sample Data. ....	156

This page intentionally left blank.

# Chapter 1

## Introduction

Since its inception in 1947 at the Bell Laboratories, to say the use of transistors within our society has skyrocketed, is an understatement. Vacuum tubes had previously been used for all amplification and processing needs however since the invention of the transistor these tubes now only see use in very specialized applications. The drive for faster, smaller, more powerful, and less energy demanding devices will never cease.

Modern transistors are by leaps and bounds more reliable, faster, and physically much smaller than vacuum tube counterparts. The semiconductor industry is constantly refining existing devices and implementing new concepts to create new devices surpassing those of previous generations.

The limits must always be pushed.

There exists an ever expanding array of semiconductor materials available for research. Some of the more common materials include but are most certainly not limited to: AlAs, AlN, AlP, AlSb, CdO, CdS, CdSe, CdTe, GaAs, GaN, GaSb, GaP, Ge, InAs, InN, InSb, InP, Si, SiGe, SiC, ZnO, ZnS, ZnSe, ZnTe. These materials have a wide range of properties and energy band gaps spanning from a narrow 0.17 eV for InSb to a very wide 6.2 eV for AlN[1]. Some materials feature direct band gaps. Of these popular

semiconductors the most common are likely Si, Ge, and GaAs. SiC is a major competitor to GaN for transistor applications.

Group III-V material based semiconductors have the capacity to surpass the current generation of semiconductor devices. It has been reported in [2] that indium nitride has a maximum theoretical electron mobility of  $2000 \text{ cm}^2/\text{Vs}$ . This figure of merit greatly exceeds that of silicon based devices.

Gallium nitride based devices, which are more mature to the industry, have the capacity for high ionization energy radiation resistance as well as higher operational temperatures making them better suited for military and space applications. This is due to the large-band gap range, large high field electron velocity, high breakdown field, and superior thermal conductivity[3].

Aluminum nitride films are popular as an electron blocking layer and insulating material. An  $\text{AlN}$  film may be used in certain situations to replace  $\text{SiO}_2$  during processing. This is gaining popularity in metal-insulator-semiconductor structures such as metal-insulator-semiconductor field effect transistors (MISFET), charge coupled devices (CCD), and metal-insulator-semiconductor (MIS) based capacitors[4].  $\text{AlN}$  is typically grown at a low temperature which is often required in the processing of III-N based devices where the high temperature growth of  $\text{GaN}$  would destroy the underlying layers.

This dissertation serves to assist in the development of future field effect transistors, light emitting diodes (LED), and solar cells which are the three main applications of the materials and technology discussed herein. A new type of semiconductor research reactor has been specifically designed and built and is housed in the Lakehead University

Semiconductor Research Lab. This reactor forms the heart of our research efforts and has been steadily generating new research since it went online in December 2010. Many advances have been realized by my peers and I through the use of this machine. It serves to alleviate some of the constraints which currently surround film growth of materials comprised of gallium nitride, indium nitride, aluminum nitride, and their ternary alloys.

One such challenge is the fundamental temperature constraints in the growth of high quality crystalline gallium nitride and indium nitride in the same system. Herein we demonstrate one method to overcome this challenge.

The aims of this body of work are three-fold:

- 1) To characterize the MEAgrow reactor.
- 2) To assist in the development of future FET devices based on III-V semiconductors, specifically those based on the modulation of the conductive channel from carrier injection arising from the destruction of excitons.
- 3) To further the development of group indium nitride based nanowires for future use in devices.

Characterizing the growth space conditions is a critical step in any new growth reactor. For the MEAgrow system it is even more essential since the system's process uses conditions different the other growth mechanisms which will be discussed. It is a new and unique process. In order to gain experience with the new system, a plethora of single film growths were performed. The growths include gallium nitride, indium nitride, indium gallium nitride, and aluminum nitride though the latter will not be detailed expansively. Growths were performed under a wide range of system conditions leading

to a deep understanding of growth parameter space. Results are detailed herein in Chapters 4 and 6.

A critical goal of this work is to provide the basis for further development of a novel unique type of field effect transistor (FET). This transistor uses group III-Nitride materials exclusively and has never been developed in any similar system in the past. Though complete realization of the device is beyond the scope of a single graduate student project, this work attempts the critical initial steps towards this end. It is hoped that the information contained herein and the associated data generated will enable future researchers to further this goal. Since the transistor is such an important part of this research Chapter 7 has been dedicated to the theory, data, and results.

During the extensive characterization of the system growth, parameter space experiments results were obtained which were proven by the scanning electron microscope (SEM) to contain nanostructures. Further investigation into these structures lead to a publication[5]. This publication along with further results is discussed in section 4.6.

## **1.1. Group III-V Semiconductors**

It is projected that the global power semiconductor market will reach \$65 billion by 2022[6]. A large portion of that market will be silicon carbide and gallium nitride based devices.

Silicon as well as conventional III-V semiconductors cannot be used in applications for optoelectronic devices in the violet and blue region of the spectrum[7]. This is due to the

band gaps for these materials not being sufficiently wide enough. Gallium Arsenide (GaAs) based devices cannot handle high temperatures.

Table 1 lists the various binary compounds possible within the group III-V. Of this list only a select few are suitable candidates for use as semiconductors. Binary compounds include boron nitride in both cubic and hexagonal phase, boron phosphide, boron arsenide, aluminium nitride, aluminium phosphide, aluminum arsenide, aluminium antimonide, gallium nitride, gallium phosphide, gallium arsenide, gallium antimonide, indium nitride, indium phosphide, indium arsenide, indium antimonide. Many ternary and quaternary compounds are also possible.

**Table 1. Complete List of Group III-V Binary Compounds**

Group III-V Binary Compounds	B	Al	Ga	In	Tl
N	BN	AlN	GaN	InN	TlN
P	BP	AlP	GaP	InP	TlP
As	BAs	AlAs	GaAs	InAs	TlAs
Sb	BSb	AlSb	GaSb	InSb	TlSb
Bi	BBi	AlBi	GaBi	InBi	TlBi

By combining various materials at selected ratios, the desired material properties of each material can be mixed to create the desired material. However, it must be understood that certain limitations are imposed and not all combinations are feasible or practical. Many semiconductors, such as GaAs have seen widespread industry use for many years and are likely to continue to do so.

## 1.2. Materials of Interest

The Lakehead Semiconductor Research Laboratory aims to further research in the group III-Nitride materials. Table 2 shows our primary materials of interest along with some of their basic properties.

**Table 2. Consolidated material properties for our materials of interest compiled from [8].**

Element	Gallium	Indium	Aluminum	Nitrogen
Atomic Number	31	49	13	7
Atomic Mass	69.723	114.818	26.981	14.007
Density ( )	5904	7310	2700	1026
Structure	Orthorhombic	Tetragonal	Cubic	Hexagon

### 1.2.1. Gallium

Gallium is typically solid at room temperature but quickly turns to liquid at slightly above room temperatures[8]. It boils at                      and melts just above room temperature at                      . Elemental gallium exists only in nature as compounds though it can be obtained easily through smelting. In metalorganic based film growth systems gallium is typically supplied as Trimethylgallium (TMG) which is discussed in section 2.3.1. It incorporates easily into other crystal lattice structures and is often used as a dopant in semiconductor based applications. At room temperature, a passive oxide quickly forms on the surface of gallium, halting any further reaction. However, at higher temperatures gallium reacts with oxygen readily and forms gallium(III) oxide                      . As such film growth systems are highly sensitive to oxygen contamination. Gallium is dissolved using

acids, a property we make use of for etching the film surfaces. By far the bulk of gallium commercially produced is used for semiconductor applications.

### **1.2.2. Indium**

Like gallium, indium is liquid over a wide range of temperatures. Indium boils at

[8]. It is stable in air but dissolves when submersed in an acid. This is an important trait as we exploit this during our etching process. Excess indium is able to be removed through etching, providing a cleaner and more stable surface for measurements and subsequent layer growths. It is interesting to note that Canada is the highest supplier of indium[8]. For use as a precursor in Chemical Vapour Deposition (CVD) systems, Indium is typically packaged as a Trimethylindium (TMI) which is discussed in 2.3.2.

### **1.2.3. Aluminium**

Aluminium is one of the most used metals on the planet. It has a plethora of applications throughout many industries, too many to list. We are interested primarily in the electrical and chemical properties of the metal. It is a highly reactive material and thus not found in an elemental state. This high reactivity causes passivation when in contact, and this is the primary reason behind the excellent corrosion resistant property of aluminium. It is extremely abundant in the earth's crust, but is produced by the refining of bauxite ore ( ). It boils at and features a low density of —. For film growth, it is packaged as Trimethylaluminium (TMA) and discussed herein section 2.3.

#### 1.2.4. Nitrogen

Nitrogen is our fourth main material of interest for this body of work. We use nitrogen not only in our plasma source but also as a carrier gas for the other precursors. We also have other uses such as chamber cleaning and purging. It is a non-metal and makes up approximately 78% of the atmosphere. It is extremely inert, and this is one of the most important properties leading to widespread use through many industries. The inertness comes from the very strong triple bond which exists between nitrogen atoms in  $N_2$ . As such it is a popular industrial gas with uses such as annealing, as a refrigerant. Liquid nitrogen has many uses. The primary use of nitrogen is in ammonia which also has many industrial and commercial applications. In the semiconductor field it is used well beyond III-V applications such as for a blanketing material in other semiconductor production[8]. It is a gas at room temperature, melts at  $-195.8^\circ C$  and boils at  $-196^\circ C$ . For film production the two main sources of nitrogen are ultra-high purity  $N_2$  and as ammonia gas ( $NH_3$ ). Refer to the section on crystal growth techniques (Section 2.2. ) for more information. III-N systems using pure  $N_2$  typically employ a plasma source to break the strong triple bond.

### 1.3. Conclusion

Having discussed the raw elements of interest in Chapter 1 we are in a better position to discuss the compounds of interest, growth of the compounds, the formation of more complex heterostructure films, and finally the embodiment of this work – the FET. This

dissertation is structured to lead the reader through the early research steps taken towards the multi-layer FET.

Chapter 2 provides a review of thin film deposition techniques relevant to this work.

Traditional film growth methods are discussed and compared to the MEAgrow growth system. The materials involved are further discussed along with substrates and precursors.

Chapter 3 provides a review of the semiconductor compounds of interest with a brief history of growth for each.

In chapter 4 the general procedure for film growth using the MEAgrow reactor is discussed followed by results obtained through many growths, broken down by growth series. Heterostructure growths, the first to be done in the system, are discussed along with published results. And finally nanostructure growth is discussed, again along with published results.

Chapter 5 discusses some preliminary results obtained through collaboration with the University of Manitoba regarding contact deposition on the films. This is a critical step towards realization of a commercially viable device.

Chapter 6 discusses the important instruments as well as techniques involved where measurements of the results are concerned.

Chapter 7 is the mainstay of this body of work. It is a discussion based on the experiments and results obtained for a new type of field effect transistor.

Chapter 8 summarizes the results discussed throughout while chapter 9 draws conclusions from these results.

A complete list of references is included in chapter 10 followed by the appendix which includes important laboratory procedures, as well as accepted-for-review and published papers.

It is hoped that the characterization of this new film growth system through hundreds of film growths will be enhanced and that future researchers of the Lakehead Semiconductor Research Lab as well as external to the school may further the development of III-N film growth. Though the primary goal of this thesis is towards the development of the FET this content, should assist future researchers in other avenues such as light emitting diodes, solar cells, and nanostructures all related to III-N films.

## **Chapter 2**

### **Review of Thin Film Deposition**

#### **2.1. Overview**

A thin film is generally taken to be as thin as a single atomic monolayer or as thick as many micrometres. It has long since been discovered that even small additions of material to a surface can greatly alter the characteristics of that surface[9]. Thin films have gained a widespread use from optical applications such as mirrors, protective, reflective and anti-reflective coatings, to industrial applications such as metal oxides, metal carbides such as hard carbon coatings, and our area of interest metal nitrides for the electronics industrial. Electronic devices use thin film layers in semiconductors, insulators, and conductors.

Production methods span an incredibly array of methods such as physical, chemical, thermal, evaporation processes, and plating. Many of these methods do not pertain particularly to III-Nitride based film production and will not be discussed. Regardless of the process used to form the thin film, the characteristics of the formed film are highly dependent on the process parameters. It is necessary to understand how the process parameters affect the film growth in order to control and optimize the film growth. This is paramount to this body of work and forms the basis for much of the methodology of the research.

### **2.1.1. Challenges in III-Nitride Film Growth**

#### **2.1.1.1. Oxygen Contamination**

Oxygen contamination is a major challenge in all film growth systems. Working with indium is a particular challenge because there exists a strong affinity between oxygen and indium[10]. When oxygen substitutes into the crystal structure the electronic properties are greatly altered. Conductivity increases. MBE is particularly susceptible to oxygen contamination through the dielectric window used in microwave plasma based systems[11]. These systems often require a number of days to pump down and reduce oxygen levels to an acceptable level[12].

Excess oxygen is typically removed from the substrate prior to film growth through elevated temperatures in the growth chamber[11].

#### **2.1.1.2. Challenges in Gallium Nitride Film Growth**

Many device designs call for an intrinsic layer of gallium nitride. It is difficult to achieve a semi-insulating layer of GaN and a large portion of this body of work has been dedicated to this goal.

#### **2.1.1.3. Challenges in Indium Nitride Film Growth**

Of our three materials of interest indium is the most volatile due to its inherent equilibrium vapour pressure[13].

The growth of indium nitride films is the subject of much controversy. Many reviews have been written on the subject[14][7], [10], [13], [15]–[18]. This controversy may be

fueled by the fact that indium nitride is very highly dependent on the growth system and parameters used. Many of the experiments in chapter 4.4. will address these issues.

#### **2.1.1.4. Challenges in Heterostructure Growth**

One of the greatest challenges we face with the III-Nitride material system is the growth of GaN on InN or vice versa. In the case of laying down a bottom layer of InN, we have to preserve and maintain the integrity of this crystal while growing the GaN on top. This is primarily due to the low dissociation temperature of the indium nitride film. This imparts the requirement that we must form our GaN layer at a lower temperature or sacrifice the integrity of the indium nitride layer. Many experiments have been dedicated to this challenge and are detailed in section 4.5.

Another challenge is lattice mismatch. This group of materials is closely lattice-matched so once a suitable set of conditions is determined, it is not overly difficult to obtain epitaxial growth. There are a number of possible solutions. One method is the growth of a buffer layer, detailed in the experiments of section 4.3.3. Another solution is to grow a thicker film which gradually reduces the strain imparted by the lattice mismatch.

However this can result in a graded material forming between the two layers (for instance InGaN in the case of InN and GaN). Experiments have been dedicated to this challenge in Chapter 4.

## **2.2. Methods of Thin Film Production**

There exists an infinite possibility of film growth methods. It is well beyond the scope of this body of work to provide background to all methods and techniques. Those closely related to the MEAglow technique shall be discussed in more detail.

### **2.2.1. Physical Vapour Deposition**

Physical vapour deposition (PVD) is a vacuum deposit method of thin film production. Gasses are general produced by evaporation, sputtering, or a non-chemical based method. Materials to be deposited generally exist in a solid phase to be sputtered or evaporated into mostly atomic species. This technique relies on the transfer of kinetic energy to overcome atomic binding energy[19]. Plasmas are often employed to assist in growth. One of the most common forms of a PVD is molecular beam epitaxy (MBE).

### **2.2.2. Chemical Vapour Deposition**

In chemical vapour deposition (CVD) the solid thin film is created from a reaction of source gasses. The materials to be deposit exist in a dense gaseous[19] phase and form a solid at the growth interface (surface). Many alterations of the basic CVD method exist operating at different pressure ranges, and using alternate types of reactants. Some systems employ the use of a plasma to further activate the reaction[20]. CVD methods have a few advantages over CVD systems. The reaction can be area selective, and is more conformal on rough surfaces. The source gasses are housed externally to the system, which prevents chamber contamination (from exposure to atmosphere) when

refilling gasses. Lower vacuum levels may be achieved. Large batch processing is facilitated. PVD systems tend to be more forgiving towards variations in process parameters[20]. Some disadvantages include the use of toxic materials, and the often required higher growth temperatures. A few common CVD methods include metal organic chemical vapour deposition (MOCVD), plasma enhanced chemical vapour deposition (PECVD), and migration enhanced afterglow (MEAglow).

### 2.2.3. Comparison of Growth Methods

**Table 3. Comparison of Various Growth Techniques[12][21].**

System	Growth Pressure Range ( )	Growth Temperature Range ( )	Growth Rate (—)	Typical Nitrogen Source
MBE				Ammonia or
MOCVD	~760			Ammonia
PECVD	to	to	to	Ammonia or
MEAglow	to	to		
MOVPE		to	to	Ammonia or

### 2.2.4. MBE

Molecular Based Epitaxy is a process based on a ultrahigh-vacuum evaporation[12]. The vacuum requirement makes it a relatively expensive process. MBE allows for low growth temperature which limits diffusion. Growth rate is limited to typically — [12].

However, this ensures a high quality 2 dimensional growth is achieved. A molecular beam is used to decompose effusion cells made up of ultra-high purity materials. The system operates via mechanical shutters which modulate the beam and this allowed for control of doping and general material composition. Modern MBE systems feature nitrogen source gas ( ) as opposed to ammonia[10]. It is a well-established process and is modelled easier than most other processes. A major advantage is the possibility for in-situ monitoring applications such as Auger Electron Spectroscopy (AES), Low Energy Electron Diffraction (LEED), Reflection high energy electron diffraction (RHEED), and Residual Gas Mass Spectrometric analysis (RGA). Operating pressures of are typical[12]. Major advantages of MBE include the possibility to grow high quality InN, not typical in other systems. Low growth temperatures allow for compatibility for the growth of InN and InGaN[10]. It also excels at providing precise interfaces between growth materials[22]. Though growth temperature is extended in the lower range, it is limited in the upper range but is typically around [22]. Using MBE for the growth of GaN at low temperatures, which is often desirable in order to remain compatible with indium based growths, tends to produce rough surfaces. This occurs because the growth is nitrogen-faced. This can be improved by switching to gallium-faced growth, however this is a challenge to accomplish with MBE[23] and is not possible directly on sapphire. Another major setback for this technology is the 48 to 72 hours required to pump down the system to remove impurities prior to growth after opening the system for maintenance[12]. This in turn raises the operating cost.

### 2.2.5. MOCVD

Metal organic chemical vapour deposition systems are a major contender to MBE. These systems operate at a much higher growth temperature often well above [22]. Operation is based on the dynamic flow of precursor gasses over the heated substrate. System orientation can be horizontal or vertical. The geometric orientation has a pronounced effect on growth. Since many different system configurations exist, it is often difficult to compare results between research groups. The reactions taking place are complex and not yet fully understood. Modelling of these systems is difficult[22]. However, this technology is well established and these systems are often used in the production of optoelectronic devices. Higher growth rates can be achieved versus MBE[22]. Ammonia is reacted with precursor gasses, typical TMGa, TMIn, or TMAI at the substrate surface.

In order for a growth to proceed, high III / V ratios are required in excess of 1000 gallium, indium, or aluminum atoms per nitrogen atom. High growth temperatures in excess of are also a must in order to encourage the reaction. And finally, high gas velocities must be maintained. These requirements indicate that the reaction itself is so inefficient that the chamber must be flooded to obtain a growth. However despite these challenges, high growth rates exceeding — are possible (for GaN). To obtain high quality films, a nucleation layer must be grown prior to the main buffer layer[22]. Finally the film may be grown on these layers.

### 2.2.6. PECVD

Plasma Enhanced Chemical Vapour Deposition combines a CVD system with a plasma source. The added complexity of a plasma source is greatly offset by the many advantages of using a plasma. The plasma may be DC, RF, or microwave based. Further discussion on the plasma sources can be found in section 2.4. Use of a plasma allows for growth at lower temperatures versus conventional MOCVD[24] extending possible low range temperatures to the to . These systems can be further classified by conventional (direct) or remote (indirect) PECVD. In a remote PECVD system the substrate is placed outside the plasma generation region[24], while the opposite is true for direct systems. The greatest contrast between remote and direct systems is the partial excitation of process gases in remote systems. Because the MEAgrow system closely relates to the remote PECVD system, we will limit our discussion to this sub classification. Chamber operating pressures are typical of to similar to MOCVD. This relatively high operating pressure (in contrast to say MBE) encourages interspecies collisions, one of the primary reaction motives. Growth rates are also comparable to MOCVD based systems, ranging from to —.

### 2.2.7. MEAgrow

The MEAgrow growth technique has been developed based on recent advances in migration enhanced epitaxy (MEE)[25]. MEE is a low temperature growth technique originally employed in MBE systems. Originally intended for the development of arsenide films, it has since been modified for use in group III-nitrides[25].

In this technique, the precursor materials are carried by adatom diffusion across the film growth front. Once a suitable lattice site is realised, the precursor is bound into the material to form the stationary molecules which make up the crystal structure of the film. One of the critical aspects differing from other growth methods is that the precursors are given extra time to migrate across the surface. This allows for enhanced two-dimensional crystal growth.

The MEAgrow system employs MEE in a system similar to MOCVD discussed above, with aspects of MBE incorporated. Higher pressure than MBE, at close to [23].

Because of the relatively higher pressures used in the system, the higher energy nitrogen compounds are reduced in number prior to reaching the growth surface due to collisions. The bulk of the nitrogen atoms remaining are atomic with low activation energy.

### **2.2.8. MOVPE**

Since its inception in the late 70s, Metalorganic Vapour Phase Epitaxy (MOVPE) has been a major process technology for the production of compound semiconductor devices, particularly those of the III-V material group[26]. It is a popular technology for optoelectronic devices. Precursors used include but are not limited to: TMI<sub>n</sub>, TMAI, and TMGa. Pure source nitrogen is often used as a carrier gas though the use of ammonia is also common. It is a chemical vapour deposition technique and synonymously referred to as OMVPE, OMCVD, and MOVPE. The growth mechanism involved relies on the formation of volatile metal halides as transport agents[26] for surface growth. Commercial systems can process up to wafers at a time, in diameter[26].

Operating pressures tend towards atmospheric, however a low pressure form exists referred to as low pressure metalorganic vapour phase epitaxy (LP-MOVPE). Indium nitride growth in these systems favours atmospheric pressure for more reactive nitrogen, or low pressure ( ) for enhanced epitaxial growth. As with other systems, the low temperature growth restricts the decomposition rate of ammonia, however increased growth temperature brings about the decomposition of InN and introduces thermal etching in the grown films[13]. Too-low temperature reduces migration of the materials and prevents epitaxial growth. As such, growth temperatures for InN are limited to with an average around [13]. Lower temperature growths require a high V/III ratio while high temperature growths require a low V/III ratio. Vapour pressure and growth temperature are the most critical operating parameters[26]. This type of system is more favourable for the growth of GaN than AlN. Reactor design (horizontal versus vertical) is critical for systems used in InN film growth. Limitations for this system include doping, composition, and film thickness[26].

### **2.3. Precursors**

The MEAGlow growth system relies on precursor gasses fed into the system chamber to react at the growth interface (substrate surface) to realize a film. The precursor gasses available for this body of work included trimethylgallium, trimethylindium, and trimethylaluminium. Each is discussed briefly. The precursor gasses are housed in the systems gas cabinet, which maintains a constant temperature and a positive pressure out the exhaust for safety. The precursors are stored in metallic bubblers with in-feed and out-feed safety valves. The canisters contents are evaluated by means of mass

measurements at the time they are received and prior to returning to the production facility. Care must be exercised when handling these bubblers as metalorganic materials exposed to the atmosphere can easily cause a fire. The precursors are fed to the main chamber by means of a nitrogen carrier gas.

### **2.3.1. Trimethylgallium (TMG)**

Trimethylgallium is the precursor source used in the MEAgrow film growth system. It is often referred to as TMG or TMGa. It is comprised of a gallium atom bound to three methyl groups [27].

Despite much research, the detailed mechanism of TMG use in the formation of films is not clear[27]. Detailing this mechanism is beyond the scope of this dissertation and will only briefly be discussed. The same is true for TMI and TMAI.

TMG must be stored at or near room temperature to avoid deterioration.

### **2.3.2. Trimethylindium (TMI)**

The makeup of Trimethylindium is almost identical to TMG, substituting the gallium atom with indium ( ) and similarly is referred to as TMI or TMI<sub>n</sub>.

The storage of TMI is more sensitive to temperature than TMG. It has a tendency to foul or plug the feed lines if the temperature drops below . As such the MEAgrow gas system features a heater on the bubbler as well as around the systems gas feed lines.

### **2.3.3. Trimethylaluminium (TMA)**

Trimethylaluminium varies from TMG and TMI in that two aluminium atoms are bound to six methyl groups i.e.  $(\text{CH}_3)_2\text{Al}(\text{CH}_3)_2$ . Two of the methyl groups are shared while each aluminium atom bonds to two of its own through single aluminium-carbon bonds[4]. Like TMG and TMI it is easily synthesised and suitable for use in MOCVD systems. The aluminium carbon bond is quite strong, and as such it becomes a challenge to use TMA for low temperature growths due to carbon contamination within the film.

### **2.3.4. Magnesium**

The MEAgrow reactor is currently configured for the injection of aluminum, indium, gallium, and magnesium into the chamber. Magnesium, with a typical oxidation state of +2 is used for p-type doping of the films. Few experiments involving doping were performed related to this body of work so it will not be discussed in detail.

## **2.4. Plasma**

Plasmas play a critical role in modern semiconductor processing systems such as plasma enhanced chemical vapor deposition (PECVD), sputter deposition, reactive ion etching, plasma etching, physical sputtering, reactive sputter deposition, and a number of ion beam based techniques[12]. Throughout the film growth industry the use of plasmas is steadily increasing. Systems are becoming more complex in an effort to produce better results.

### 2.4.1. Definition of a Plasma

Plasma refers to a gas of charged particles including electrons, ions, neutrals (atoms, molecules) and also photons[28]. Plasmas are often referred to glow discharges based on the visual aspects from photon emission[12]. Despite the charged particles, the plasma is considered neutral on the whole as the charges balance out. Plasmas are often considered the fourth state of matter. The term plasma is often used synonymously with glow discharge due to the release of photons which occurs as the charged particles experience a de-excitation[12]. This de-excitation creates the visual glow we can see. Plasma can be more conductive than the surrounding metal. Elevated temperatures and high energy densities result in particle collisions which can cause thermonuclear reactions. Though the charges balance out within the plasma the ions have more mass and thus move much slower than the lower mass free electrons. The energetic species comprising the plasma is used for the growth reactions. These species are much more reactive than can be produced by a chemical reaction. The accompanying neutral particles are also highly reactive. Due to the highly reactive nature of the plasma, undesirable physical changes such as etching may occur if conditions are not correct. Plasma-assisted processes often see an increase in efficiency of the process, or in some cases reduce the negative environmental impact[12].

One of the most critical aspects of the plasma is the operating pressure. Other factors are highly dependent on the pressure such as luminosity, energy, and temperature. Plasmas are often classified by two essential aspects: the average temperature and the density of electrons within the plasma. Typical average temperatures range from to while electron densities run from to [28].

### **2.4.2. Advantages of Using a Plasma**

Plasmas have long since been used in film processing systems because of the number of unique advantages which they provide. A typical film deposition system will often see an increase in film deposition rate along with the possibility of lowering growth temperature. The result is an increase in productivity not possible without the plasma. This in turn leads to lower operating costs for the processing system despite the additional power and equipment requirements needed by the plasma.

Plasma based systems allow for new combinations of input materials to produce unique compounds not previously possible. Substrate choices suitable for film growth are also extended and the processing plasma can lead to improved adhesion of the film to the substrate. Plasmas allows for enhanced process control leading to improved quality of the final film. And finally plasmas allow for deposition to occur under non-thermal equilibrium conditions[9].

### **2.4.3. Plasma Application in Film Deposition Systems.**

Despite the long term and widespread use of plasmas in semiconductor processing equipment the role of the plasma is extremely complex and has yet to be fully understood[9]. To enhance the reactivity, energy is supplied to the film growth species. Thus it is desired to have a high plasma density which promotes high reactivity and allows for a wide range of deposition conditions.

Plasma is generated by applying voltage across a gas. The gas becomes conductive at a certain voltage due to ionization. This threshold voltage is a function of the distance

between the electrodes, the gas pressure, and the gas material. It is an avalanche process. Electrons are accelerated by the electric field and strike atoms, releasing another electron. The original electron is still free to collide again. Steady state is reached when the number of new electrons released by collisions equals the number lost to recombination within the plasma or diffusion at the edge of the plasma. The glow is a result of recombination and an atom de-excites.

(1)

#### **2.4.4. Types of Plasmas**

There are numerous ways to produce processing plasma. One of the simplest and most reliable methods is the use of two powered electrodes separated by a distance, with the electrodes driven by a direct current (DC) source. This is termed a direct current plasma or DC diode plasma. Another method exists by which the plasma is generated indirectly by an induced radio frequency (RF) current through a non-conductive dielectric window aptly named the RF diode plasma. A third method exists by which the plasma is generated by the acceleration of electrons emitted from a hot filament. And finally the last type we shall examine is the most important for this body of work; the hollow cathode plasma – a unique configuration which may be DC or RF powered.

##### **2.4.4.1. Direct Current (DC) Plasma**

The simplest method of generating processing plasma is by application of a direct current across the growth chamber via two electrodes. It is a highly effective method and one of

the most commonly used and well-studied. The theory of the DC plasma forms the basis for other more complex sources, and will be discussed in some detail.

Upon application of the direct voltage across the anode and cathode, a non-uniform electric field is established with a number of distinct regions. Two dark regions and three glowing regions make up the plasma. Immediately adjacent to the cathode exists the cathode glow region. It is a thin, luminous region often difficult to see due to the minimal amount of collisions. The cathode dark space, termed Crooke's dark space exists adjacent to the cathode glow region and is absent of any luminosity. This is due to the large electric field which exists causing acceleration of the electrons and as a result very few electrons are available to cause excitation of the background gas atoms[12]. The terms cathode sheath or space charge sheath typically refers to this region. The negative glow region exists adjacent to Crooke's dark space and is evident by the highly intense glow caused by electron collisions to the charged particles and subsequent release of photons. In this region electrons and ions exist at roughly equal densities, which typically range from  $10^9$  to  $10^{13}$  charges/cm<sup>3</sup>[12] while electron temperatures range from 1-10 eV. Most processing plasmas use the negative glow region for growth and placing the substrate within this region. The Faraday dark space exists adjacent to the negative glow region. It is characterized by the lack of illumination. At this point in their path the electrons have lost most of their energies through collisions in the other regions and are unable to provide enough energy to the background gas atoms to cause an excitation. The positive column exists adjacent to this, which does provide illumination due to local electric fields. This region is important to plasma light sources but of little importance to processing plasmas.

The primary advantages of DC based processing plasmas are that the theory is well understood and the application is relatively simple and straightforward in contrast to other types plasma sources.

The downside to DC based processing plasmas is that other plasma sources have the potential to provide further advantages. The efficiency of DC based plasmas also suffers. For a typical DC plasma powered at only is used to generate the secondary electrons useful to the processing.

#### **2.4.4.2. Radio Frequency (RF) Plasma**

Radio frequency plasmas provide an increased level of ionization in the plasma[12].

A key difference between a DC plasma and one operated by an RF power source is the self-biasing effect. Above the slower moving ions are unable to keep up with the faster electrons. This leads to a stack up of ions while occurs on the electrode which is more negative with respect to ground[12].

RF plasmas can be very similar to DC plasmas in design of the electrodes.

Radio frequency plasmas require the use of more complex external power supplies and matching networks to properly compensate for the internal bias of the plasma as well as adjusted the forward and reflected power. The plasma source, power supply, and balancing network must all be specifically designed to work in unison under the chamber's operating conditions and plasma source atmospheric conditions. Failure to match the components together results in poor quality plasma which may not be sustainable. As such RF plasma systems can be difficult to design.

#### **2.4.4.3. Hollow Cathode Plasma**

The hollow cathode plasma source provides many of the benefits of the radio frequency plasma source and is similar in operation. The key difference from a traditional RF plasma is that both electrodes are powered by the same voltage and phase[12]. The term hollow cathode is derived from the effect on the secondary electrons. As with the case of a normal DC or RF plasma ions from the plasma cross the dark space and bombard the cathode surface. Secondary electrons are then emitted from the cathode across the sheath to the plasma. However since the two electrodes are powered equal, the secondary electrons are reflected by the identical sheath on the opposite electrode. The process then repeats many times per cycle causing a trapping effect on the secondary electrons. This increasing the probability of ionization leading to an increase in charge density by as much as a factor of 10[12]. The resulting voltage is also much lower than a DC or RF plasma at the same power level. A number of geometric variations are possible with this configuration leading to wide applications.

The hollow cathode effect is easily scaled up to provide large area deposition for large production applications[25]. Since it is comprised of a number of hollow cathodes, each one acts as an independent intense plasma source[29].

The hollow cathode effect can occur in RF plasma applications at the source gas location. This effect is typically undesired and may cause issues such as contamination[12].

Experiments relating to the hollow cathode with a DC power source have been performed and are detailed below.

#### **2.4.4.4. The MEAglow Plasma Source**

The MEAglow plasma source is a modified hollow cathode design. It may be powered from RF or DC. The plasma head is water cooled through the use of an external chiller as the heat generation during operating can be quite high. Power connections, whether RF or DC, are fed through the top of the plasma head with a nylon isolator. Care must be taken to ensure that the RF or DC connections do not come in contact with the molybdenum plasma head which is grounded. Plasma input gasses, in our case high purity nitrogen, are supplied through the top. No oxygen contamination exists since this type of plasma features no dielectric window.

The distance between the substrate holder and the plasma head is adjustable. For most film growths the substrate is located such that the damaging high energetic species generated by the plasma have decayed before reaching the growth interface (substrate surface). This is deemed the afterglow region of the plasma. No optical emission is present at this region due to the lack of high energies species. This region is located downstream of the main plasma where most of the optical emission occurs. Locating the substrate in this region reduces damage.

When the system became active in January 2011 it was immediately necessary to gather some characteristics about the new plasma head. There are a number of ways to characterize a plasma. It is relatively easy to measure some parameters including voltage, applied power, discharge current but these external parameters do little to describe the plasma within the system. The most popular method is by means of inserting a Langmuir probe into the active region of the plasma and measuring the current in response to the

voltage. From this, the electron temperature ( ) and electron charge density ( ) can be derived as well as the ion density, and plasma potential[30]. This experiment has been published[25][21] and is further detailed in this section. It must be noted that although the Langmuir probe is extremely useful in characterizing the system it also acts as a source of contamination within the system and as such it cannot be used for in-situ monitoring. It is useful only in calibrating the system and gathering characteristics of the plasma.

The electron temperature ( ) describes the amount of energy the unbound electrons within the plasma have. Typically plasmas adhere to a Maxwellian distribution of electron energy[4]. The higher the electron temperature, the higher the kinetic energy per particle and the more susceptible the system is to damaging the film or substrate.

For our experiment the probe consisted of a copper wire of diameter with an exposed length of providing an exposed surface area of approximately . The inductor used was with a resistor. The probe was mounted on the gate valve connection to the main chamber and was adjustable vertically approximately , enough to allow the probe to be inserted into the hollow cathode.

The plasma head was thoroughly cleaned prior to the experiment. The experimental setup is shown in Figure 1. The power supply voltage and nitrogen flow to the plasma were varied and the following parameters were measured: forward power, tune, load, chamber pressure. Voltage measurements were limited to the positive and negative current saturation levels.

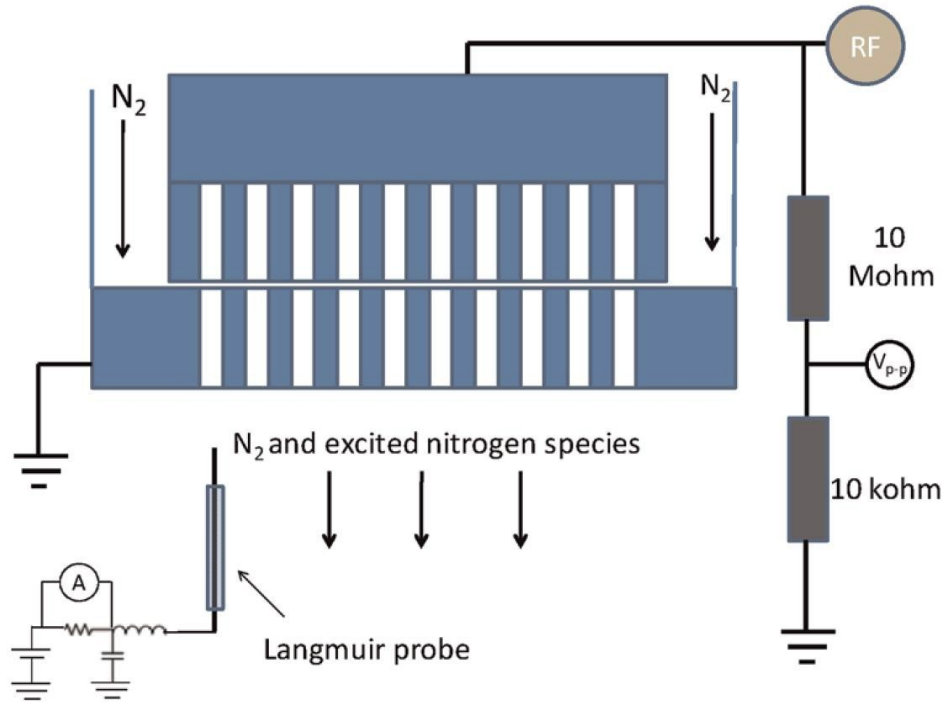


**Figure 1. The Langmuir probe setup used to obtain measurements[21].**

In order to evaluate the electron density ( ) we must use the well known equation for ion saturation current (Equation 2).

$$I_{sat} = A_p n_e e \sqrt{\frac{m_e}{m_i}} \quad (2)$$

Where  $A_p$  is the probe tip area in  $\text{cm}^2$ ,  $e$  is the electron charge,  $n_e$  is the electron density we are looking to calculate. An electron temperature of  $2\text{ eV}$  is assumed, which is a well known value for hollow cathode type plasmas[25] and finally  $m_i$  is the mass of nitrogen ion in  $\text{kg}$ . Powered by a  $100\text{ W}$  at  $13.56\text{ MHz}$ , the resulting charge density of  $10^{18}\text{ m}^{-3}$  is an reasonable value in line with other hollow cathode sources[25]. This

value is expected to be even higher when the plasma is supplied by an RF rather than DC source.

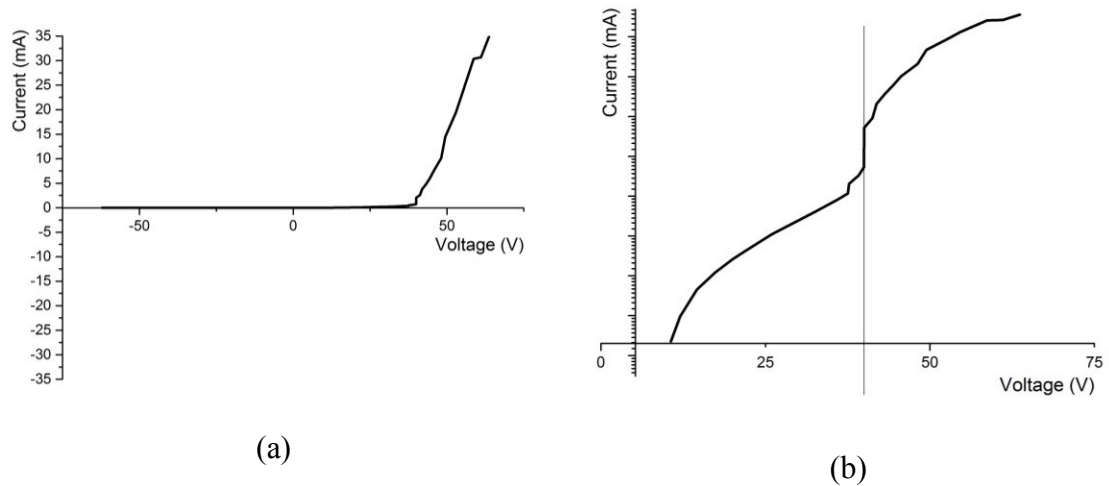


**Figure 2. IV characteristics obtained by Langmuir probe measurements. (a) in linear form (b) by natural log. The vertical line indicates the plasma potential.**

It is important to note that the use of an uncompensated Langmuir probe was used. This provides certain limitations in the accuracy of the results, however for the purposes of classifying the electron density of the plasma this method is deemed suitable.

It must be understood that the characteristics of DC plasma will vary from those of the RF plasma. For the RF plasma, the bias voltages are generally higher due to the electron temperature.

## 2.5. Buffer Layers

Buffer layers are an essential component to nitride based thin film growth. All stacked materials exhibit a mismatch in the lattice constant, causing a strain in the film layers.

The lattice mismatch also causes dislocations which may propagate, degrading the

electrical properties of the resulting film[31]. Application of a buffer layer can reduce this strain[32]. Lattice mismatch varies greatly based on the quality of the film however for GaN grown on sapphire this mismatch works out to about 13-15%[33][7]. Strain in the film is reduced as the thickness is increased. When the film reaches what is termed the critical thickness, the lattice parameters are equal. For GaN on sapphire this thickness is approximately 100nm[7]. However, the growth of a very thin AlN buffer layer reduces this thickness to 3nm. As such AlN is often used as a buffer layer below GaN. It is also an effective insulator. Buffer layers encourage two dimensional growth[34].

However with benefits come costs. Buffer layers require a two-step growth process increasing overall film growth time and cost. In general buffer layers are also grown at very low growth rates in order to achieve good monocrystal structures and reduce impurities and dislocations.

Because of the significance of buffer layers in III-Nitride based film growth some experiments have been performed and are detailed in section 4.3.3.

## **2.6. Growth Regimes**

In the growth of gallium nitride three generalized growth regimes are possible[35]. In the first regime a gallium rich environment exists in which gallium droplet formation is evident. In the second regime a nitrogen rich environment exists, and the third regime is intermediate between the two[36]. The growth regime is determined by the material which is limiting the growth rate. For example in an excess gallium regime the growth

rate will be controlled by the available nitrogen flux[7]. Throughout the experiments detailed in Chapter 4 the concept of growth regime is considered.

## **2.7. Nitridation**

Nitridation is a thermochemical process by which the application of nitrogen to the growth environment results in its incorporation in the growth surface[37]. Typically this is the substrate, but can also be the top layer in a heterostructure film growth. Nitridation is a critical step in the film growth process. Like any process it is controlled via a number of parameters. Through no specific experiments were performed directly relating to the nitridation, many experiments did alter the nitridation step of the program and as such consideration is given to these changes in the relevant experiments detailed in Chapter 4.

The advantage of the nitridation process is improved electrical and optical properties as well as improvements in the surface morphology[38]. The only disadvantage is the additional step required in the program extending the overall film development time and a mild increase in the amount of nitrogen used.

## **2.8. Sample Preparation**

Prior to each film growth the substrate must be prepared. In most cases this simply involves baking the sapphire substrate in order to remove the surface oxide which forms over time during exposure to the atmosphere. For the growth of heterostructures additional steps may be required such as etching to remove the excess metal from the

surface. Etching is detailed in the appendix. It is important to consider what the system has previously been used for. In the case of a gallium nitride growth following an indium nitride growth, the system chamber, plasma head, sample holder, and sample holder mask must be thoroughly cleaned to remove excess indium. Failure to do so results in indium incorporation into the gallium nitride film. For indium nitride growth following a gallium nitride growth this step is less critical, however the sample holder must still be cleaned as well as the mask. Initially the system employed separate sample holders for different material growths however it was found that cleaning the holder was sufficient.

## **2.9. Substrates**

The substrate serves as a mechanical support for the formation of the film. Substrates are often referred to as wafers in the semiconductor manufacturing industry. The type of substrate used greatly affects the material properties of the grown film. There are a few substrate choices for group III-Nitride growth. When choosing a substrate consideration is generally given to properties such as lattice match, thermal conductivity, electrical isolation, price, availability, quality (defects), and warping or bowing effects from heat. Lattice mismatch will cause strain in the material. Thermal conductivity affects device performance as well as film uniformity. Electrical isolation is critical to device design. Availability must be considered, as well as quality which affects the resulting film. Warping and bowing due to differences in the thermal expansion between the substrate and epilayer during growth must also be considered[39]. This condition grows worse with increasing temperature.

### **2.9.1. Silicon (Si)**

Silicon has traditionally been used for GaN devices where price is a major consideration[40]. Silicon substrates may be n-type, p-type, or semi-insulating. Due to the high lattice mismatch silicon is rarely used for InGaN or InN film growth.

### **2.9.2. Sapphire**

Sapphire (  $\text{Al}_2\text{O}_3$  ) is a widely used substrate for GaN devices as it is readily available[40]. Sapphire suffers from a relatively low thermal conductivity as compared to SiC but has a good power density of approximately  $100\text{ W/cm}^2$ . It is much cheaper than SiC.

### **2.9.3. Silicon Carbide (SiC)**

These substrates provide an advantage where high power devices require additional thermal management[40]. The disadvantage is the price. SiC substrates are used for high brightness blue and green InGaN LEDs and AlGaN/GaN HEMTs[41].

## **Chapter 3**

### **Compounds of Interest**

This chapter will discuss our primary materials of interest InN, GaN, and AlN. Each material features a direct band gap ranging from a very narrow for InN to a moderate for GaN to a very wide for AlN. These materials all feature strong bond strengths making them relatively stable.

#### **3.1. Review of III-Nitrides**

These materials are typically wurtzite in structure however cubic phase or a mix is sometimes present. In general n-type or semi-insulating films are common while p-type films are possible but present additional challenges. Carrier concentrations vary widely. The properties of each material are highly dependent on the method used for growth as well as the growth parameters. Some key material properties are listed in Table 4.

**Table 4. A comparison of our semiconductors of interest at 300K[42].**

Semiconductor	GaN	InN	AlN
Crystal Structure	Hexagonal wurtzite	Hexagonal wurtzite	Hexagonal wurtzite
Density ( )			
Lattice Constant ( )			
Band Gap (eV)		Refer to section 3.3.	
Coefficient of Thermal Expansion (a-axis, )			
Coefficient of Thermal Expansion (c axis, )			
Coefficient of Thermal Conductivity (—→)			
Refractive Index			to
Melting Point (K)			3273

The ideal crystal contains a one-to-one ratio of nitrogen atoms to metal atoms, but this is rarely achieved. Films may be polycrystalline or monocrystal.

### 3.2. Gallium Nitride

GaN based green to ultraviolet LEDs hit the market in 1994. The first gallium nitride based power device hit the market in 2010[6]. Gallium Nitride based power transistors are currently in competition with three other device technologies: Si, GaAs, and 4H-SiC. Each technology has its limitations and advantages. A summary is provided in Table 5 below.

**Table 5. Comparison of Leading Power Transistor Technologies[40].**

Material	Mobility ( , $\rightarrow$ )	Dielectric Constant ( )	Bandgap ( , )	Breakdown ( , $\rightarrow$ )	( )
Si	1300	11.9	1.12	0.3	300
GaAs	5000	12.5	1.42	0.4	300
4H-SiC	260	10	3.2	3.5	600
GaN	1500	9.5	3.4	2	700

Gallium nitride based devices are applied to a wide range of applications including pulsed radar, counter IED jammers, CATV modules, industrial, defense, medical, and commercial, traffic lights, mobile phone backlights, automobile lighting, optical storage mediums, high power microwave transmitters, and UV detectors/emitters. The application field for these devices is continually expanding as the market opens up to this new technology. Gallium nitride is used commercially for blue LEDs[27].

Gallium nitride semiconductors are said to be the second most important semiconductor technology with silicon still remaining the most important[10].

GaN features high power densities allowing for device operation at a maximum working temperature of up to  $200^{\circ}\text{C}$ , greatly exceeding that of silicon devices. GaN devices feature fast carrier transport, and high breakdown voltages. High breakdown voltages allow for large drain voltages, higher output impedance, and easier matching into circuitry[40][6]. Of particular interest to this body of work is the suitability of GaN for use as a channel material. The large sheet charge leads to large current densities reducing transistor area, imparting a higher power per area of the gate[40]. This leads to lower capacitance per output power. Devices can have lower drain to source resistances, and higher switching frequencies[6]. GaN devices have a cost advantage over SiC technologies[6].

### **3.3. Indium Nitride**

InN typically exists in the wurtzite phase though the cubic phase is common. There exists a strong controversy regarding the actual band gap of indium nitride[15]. The bandgap is often taken to be between  $0.7\text{ eV}$  and  $1.9\text{ eV}$  [4]. It has been suggested that the lower range  $0.7\text{ eV}$  band gap is due to a deep level defect in indium rich materials[15]. The actual band gap likely lies somewhere in the middle range. A complete treatment to this subject is beyond the aims of this body of work. However, it is very important to determine the band gap accurately as the band gap dictates application suitability and therefore determines research interest and direction. Many aspects of InN are yet to be fully understood including effective electron mass, defect properties, the role of oxygen within the material, the variation of decomposition temperature, and the lattice constants[10]. Some of these properties are investigated in the experiments detail in

Chapter 4. Because of the volatility of indium nitride, growth temperatures are often limited to under [10]. Applications for InN are typically optical based such as photo detectors, and LEDs though new film growth technologies and research interest are expanding applications to power devices. InN is very conductive and features a high mobility greatly exceeding that of silicon. It is not yet a widely used material in the semiconductor industry and this is likely due to the added complexities of producing quality material. To lattice match other materials such as GaN, the indium ratio must be kept low.

InN is very sensitive to the manner in which it is produced. MBE grown material varies greatly from that produced using MOCVD based methods. Thus far, MBE methods have produced the highest quality material. As such, InN suffers from a wide range of reported material properties[10]. Of all the III-V materials, InN features the theoretically highest mobility[43]. It has the lowest melting point and is the most volatile.

### **3.4. Aluminum Nitride**

Aluminium nitride has a wide range of applications including use as an encapsulant in the electronics industry, a thermally conductive base for high temperature electronic devices, a high temperature corrosion resistant refractory material, as buffer layers in a number of semiconductor applications such as LEDs[4]. It is useful as a passivant or insulating layer for compound semiconductors[4]. As an insulating layer it provides a number of advantages such as lowering device leakage currents in Metal-Insulator-Semiconductor (MIS) devices (MISFET, CCD, MIS capacitors). The high insulating property allows for

thin insulator layers reducing threshold voltages and power requires for devices such as FETs. It features a wide band gap for optical applications extending into the deep ultraviolet. Growth temperatures are low, making AlN compatible for existing processing technologies[4]. It is often used as a buffer layer to lattice match or provide an insulation between the epilayer and the substrate. Similar to the InN and GaN the structure is typically wurtzite.

# **Chapter 4**

## **Single Film and Heterostructure Film Growth by MEAglow**

### **4.1. Introduction**

One of the prime goals of this research was to obtain high quality monocrystal epitaxial films. Epitaxy describes a regular, repeating atomic crystal structure free of dislocations and other defects. High quality films are grown as two-dimensional. Three-dimensional growths lead to island formation and polycrystalline films.

#### **4.1.1. The MEAglow Reactor**

The growth of gallium nitride, indium nitride, and aluminium nitride within the same system poses a number of unique challenges. The system must be designed in such a manner as to be flexible yet sensitive to cross contamination of the metalorganic input materials. The typical growth temperature ranges for GaN and InN films are not compatible with conventional MBE and MOCVD based systems[44].

The MEAglow growth reactor became active in late December 2010. The official ribbon cutting ceremony took place on June 15<sup>th</sup>, 2011[45]. This new lab and the technology used within promises to overcome the shortcomings of existing growth technology such as MBE and MOCVD[46].

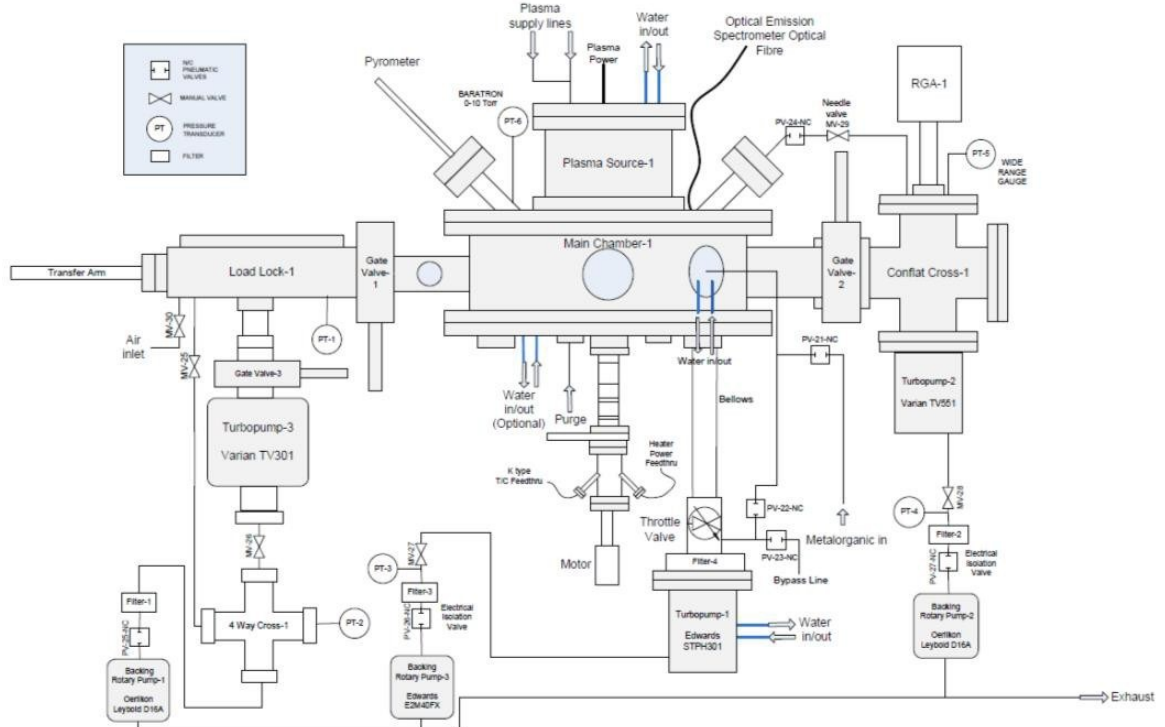


**Figure 3. The MEAglow growth system model 0001.**

The system is comprised of three main sections illustrated by the schematic in Figure 3. Each section features an individual turbo pump for maintaining the required ultra-high vacuum and each turbo pump is backed by a rotary pump. The main chamber acts as a hub for all other connections to the system. The load lock allows for loading and unloading of samples and is detailed herein. The monitor section (indicated by Conflat Cross-1 on Figure 3) allows for in-situ monitoring by a number of means. Each section is isolated by means of gate valves to the adjoining sections.

The sample holder is housed within the main chamber below where the gasses flow in. It rests atop a rotating pedestal controlled by an external motor. This pedestal allows for the installation of various accessories and was used for the Langmuir probe experiments detailed in section 2.4. The plasma system is installed above the main chamber. A number of ports exist on the main chamber to allow for the pyrometer, sight window,

RGA bypass, and Baratron pressure sensor. The chamber is air cooled by an external fan. A turbo pump is connected below the main chamber through a throttle valve to allow for pressure control. The turbo pump is backed by a rotary pump. The main chamber has a Baratron pressure sensor with a range of to and can be pumped down to as low as .

In-situ monitoring is performed by various sensors located in each chamber. The load lock must be closed during growth, and as such cannot contribute to in-situ monitoring. The analysis chamber can be pumped down to as low as and houses the residual gas analysis (RGA) which allows for detailed analysis of the gasses within the system. It is a powerful tool. Though the gate valve connecting the main chamber to the RGA chamber must remain closed during growth, a bypass line has been installed to allow for in-situ monitoring.

Switching of gas flows is performed by electric and pneumatic solenoid valves. In order to minimize oxygen contamination, the system must pump down and maintain extremely low pressures. The entire system is computer controlled for switching of gas flows, pressure, temperature, plasma, and some gate valves. The system is programmed by entering relatively simple programs, akin to recipes, into the front end software.

The use of the throttle valve allows for an operating pressure range of approximately orders of magnitude[29].

### 4.1.2. The Gas Delivery System

Metalorganic source gases are stored in a separate gas cabinet. Ultra purity nitrogen is stored externally to the system as these canisters are frequency swapped out. A mass flow controller is used between source gases and the chamber feed lines to control gas flow to

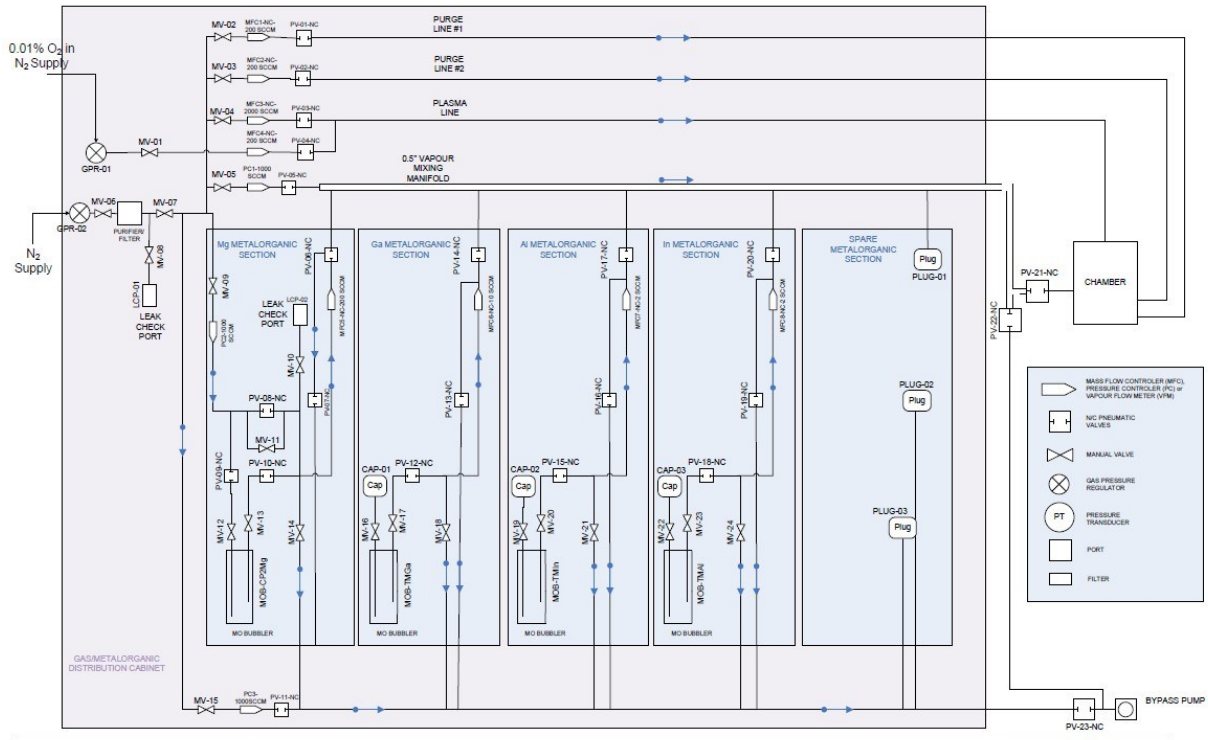


**Figure 4. MEAglow System Gas Delivery System.**

The gas delivery system for the metalorganic sources is direct without the use of a carrier gas[29]. The system is water cooled. The sources are maintained at to . Source gas is introduced in the active plasma region.

## **4.2. Operation of the MEAglow Reactor**

This section is intended to introduce the reader the MEAglow system operation but is not intended to be a full user manual. The appendix offers additional details specific to each operation.

### **4.2.1. Temperature Calibration**

The growth system does not allow for in-situ measurement of the operating temperature at the substrate growth interface. As such there are a number of temperature probes located within the system. When a system modification occurs, it is necessary to recalibrate in order to obtain accurate temperature readings. The procedure is fairly straightforward.

The system contains a total of three temperature probes. Probes T1 and T2 are thermal type probes located within the system while the Pyrometer is an infrared type externally mounted to the system. The infrared is viewed through a glass access port into the chamber and positioned such that it is centred on the substrate holder.

Temperature calibration is performed by physically mounting a fourth probe on the sample holder. No growth may occur with such a setup. This probe measures the actual temperature which the substrate would be subjected to under normal growth conditions.

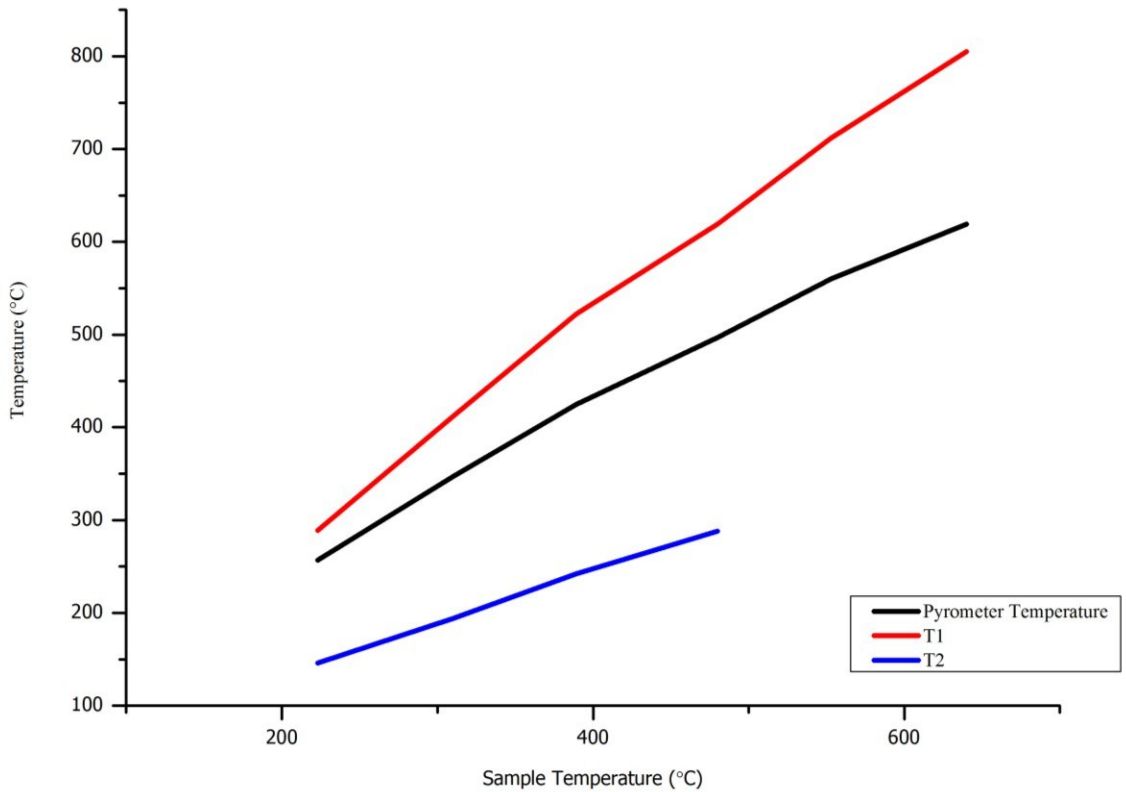


**Figure 5. Temperature calibration data from March 6, 2012.**

Data is collected for a series of temperatures and the results are stored similar to what is shown in Figure 5. Figure 5. Temperature calibration data from March 6, 2012. The probe is then removed from the system allowing for the typical growth setup. Once a growth has been completed, it is simply a matter of cross referencing the average temperature of temperature probe T1 with the latest calibration data curve to obtain the average sample growth temperature.

#### **4.2.2. Chamber Preparation**

In contrast to typical MBE systems, the MEAgrow growth reactor can be ready for growths after being exposed to atmosphere in just a few hours. Chamber preparation varies based on what the system has previously been used for. When the chamber has

been exposed to atmosphere it is recommended that a sacrificial sample run is performed in order to get the oxygen in the system. For a GaN growth following a GaN growth, little if any preparation is required. For a GaN growth following an InN growth, more care must be taken. The plasma head and chamber should be run through a heating cycle in order to purge the system of excess indium.

#### **4.2.3. Sample Loading**

The system chamber is connected to a load lock chamber with isolation provided by a lift gate valve. The load lock, or sample exchange chamber, is pumped down by a turbo pump and a separate rotary pump. It is critical that the two chambers have a similar pressure prior to opening the lift gate or the sudden rise in chamber pressure will trigger the turbo pump safety. Detailed sample loading and unloading procedures are included in the Appendix. With the sample loaded the system is now ready for film growth.

#### **4.2.4. Program Operation**

Each unique film growth requires a unique program. It is not be feasible to detail each program however the programs can be explained through generalized flow diagrams for each type of growth. The basic programs are shown below while major discrepancies warrant further explanation as per each series of growth experiments.

#### **4.2.4.1. GaN Single Film Growth Procedure**

A generalized single film GaN program is shown in Figure 6. The program begins by sealing the chamber. Initial conditions are established and the chamber is filled with nitrogen while impurities such as oxygen are pumped out. The heater is started and generally takes about an hour to heat to full operating temperature. We also adjust our operating pressure. In the final setup step prior to actual film growth, we purge out all the metalorganic gas lines so as to not contaminate our new sample and open the bypass lines in order to establish a stable flow of metalorganic material.

The heart of the program is the growth steps. Most experiments were performed by adjusting this part of the program to measure results. Growth occurs through a loop of program steps. Gas line flows and pressures are set, the plasma is started, and the gasses are injected into the chamber at a fixed duty cycle and the process is repeated a fixed number of cycles. Each loop of the program can grow as little as one atomic layer or for faster growths multiple atomic layers. Programs which pulse the metalorganic while the plasma remains constant are referred to as metal modulated. Programs which cycle the plasma on and off are referred to as migration enhanced.

Once the loops are complete the program prepares for shutdown. The gas lines are flushed out and the system is allowed to cool generally with nitrogen flowing. The chamber is evacuated. Once cool the sample may be removed. Refer to the appendix for this procedure.

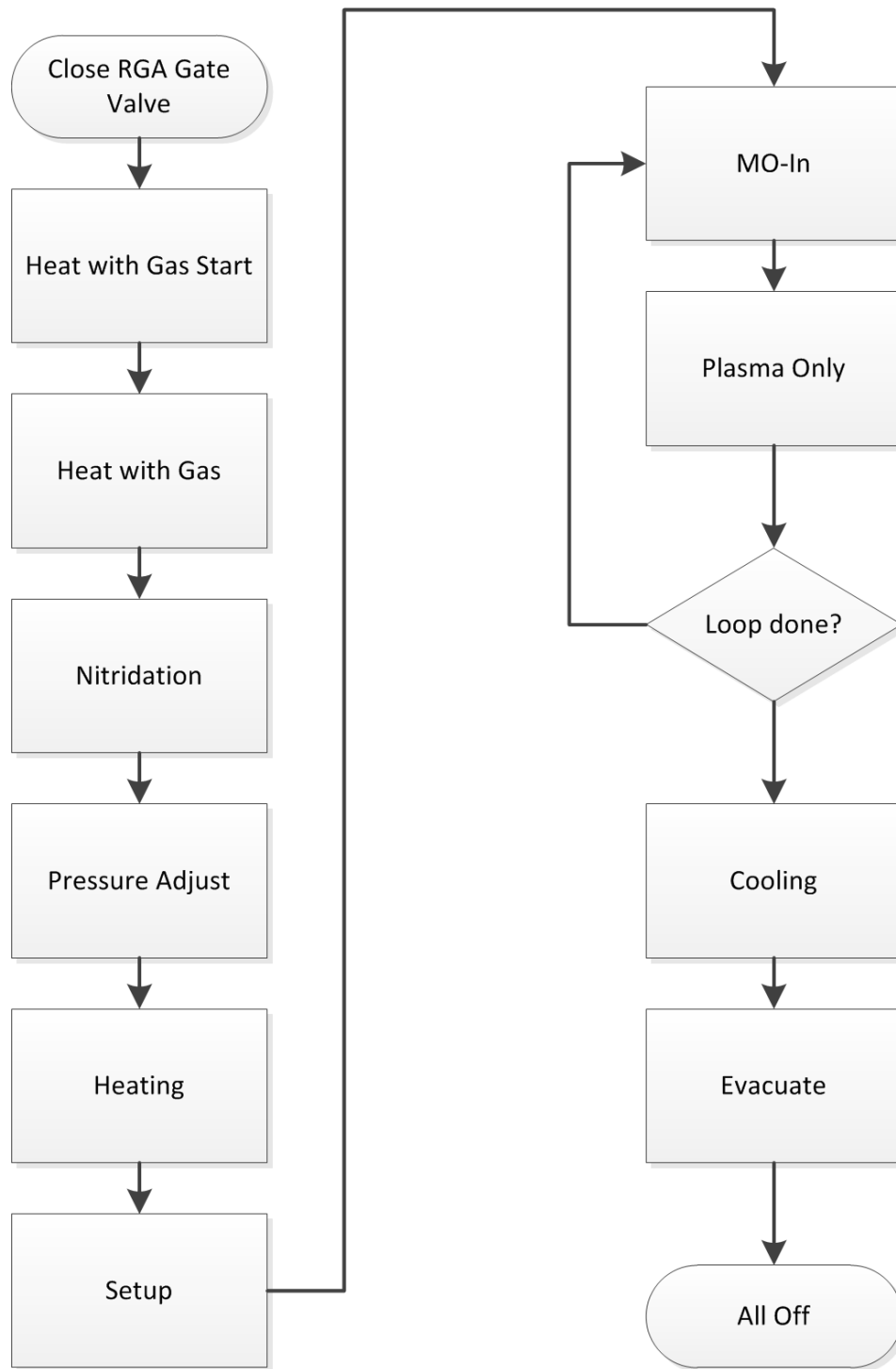


**Figure 6. Generalized metal modulated single film GaN growth.**

When exposed to the atmosphere an oxide will form on the surface. For most of the analysis this oxide has little effect. However in certain cases etching is required, especially if the sample has aged.

#### **4.2.4.2. InN Single Film Growth Procedure**

Growth of InN proceeds in a manner similar to GaN as shown in Figure 6. However some key differences must be explained. For most InN growths the shown in Figure 7 apply. Steps 1-4 have been grouped for illustration purposes.

It was discovered that InN film growths benefit from additional program steps. Specifically after a set number of growth cycles have completed, the injection of metalorganic halts while the plasma continues. A set of experiments relating to this were performed and further details may be found in section 4.4.

#### **4.2.4.3. Heterostructure Growth Procedure**

Heterostructures were grown by a few methods. Initial experiments had the first layer grown as a separate uncorrelated program while in later experiments the programs were combined into one large program allowing for more automation in the process. In certain cases, single films were grown and removed from the system for measurements later to be returned for subsequent film growth.

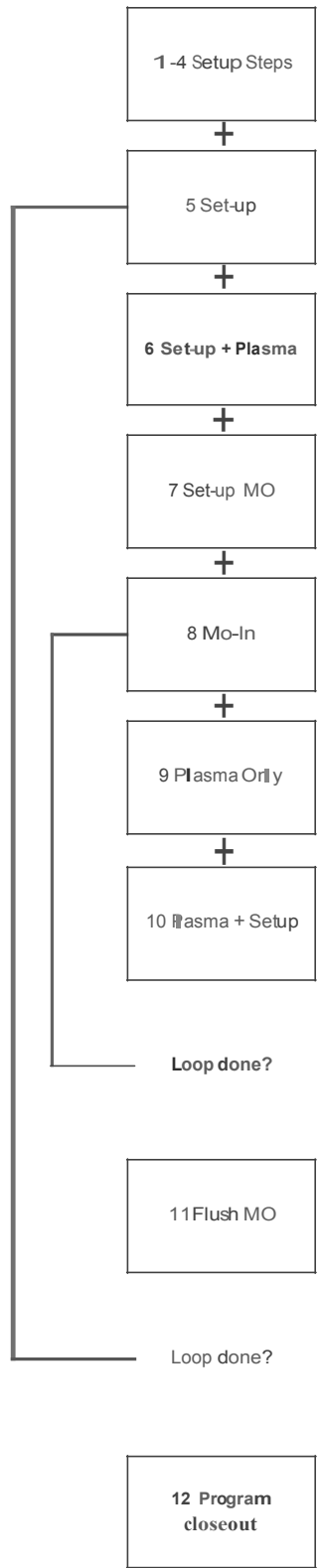


**Figure 7. Generalized InN film growth.**

#### **4.2.5. Sample Extraction**

Sample extraction is similar to loading except reversed. A detailed procedure is listed in the Appendix. Some critical points to remember are that the load lock chamber must match the growth chamber in pressure before the lift gate is accessed. The sample itself must be allowed to cool to a reasonable level for safety prior to handling.

### **4.3. Gallium Nitride Film Growths**

Since the opening of the Lakehead University Semiconductor Research lab hundreds of films have been grown. In the early days many leaps and bounds were being made at an intense rate for both gallium nitride and indium nitride. Some of these results have been published such as [25], [47], [21]. This section will outline some of the results from these publications as well as other not yet published results. Because the experiments performed in the early days varied so greatly and to a certain extent were uncontrolled the results varied widely. Organizing these early growths is no simple task. Section 4.3.1. addresses many of the GaN films grown in the general sense. Each section following will address a specific series of growths more correlated into a single experiment, for example varying one growth parameter such as pressure or temperature. Results ranged from extremely thin and smooth polycrystalline films to rough films containing nanostructures. Nanostructures will be discussed in section 4.6.

### **4.3.1. General Gallium Nitride Growth**

These growths took large leaps and cover a wide range of parameter space. They form a loosely correlated series. The goal in this early work was to achieve good results in a timely manner, and to provide a basis for further research. These experiments include much of the early results obtained.

The system has and will continue undergo changes as is the nature of a research reactor. At the time of these growths it is important to note that the grid was not installed. The high energy species flowing from the plasma head were not reduced through any active means and were simply allowed to de-energize through the process of collisions with neighbouring molecules. This leads to an elevated level of high energy species reaching the growth interface as compared to later growths with the grid installed. It is also important to note that the throttle valve was not installed in the system. This indicates that no pressure control is available other than through the control of flux of gasses into the chamber. This implies that the chamber pressure is a critical parameter for growth. Nonetheless, during these early days many good results were obtained.

#### **4.3.1.1. Experiment**

For this series TMG flows ranged from      to      .      is a unit of flow which refers to Standard Cubic Centimeters per Minute and is typically used where low flow levels are compared. Temperature ranged from      to      . This type of growth is termed metal modulated because the plasma remains on at a constant power throughout the entire growth while the metal organic precursor (TMG in this case) is pulsed. The

initial program structure was equal to that shown in Figure 6 with some alterations implemented which are discussed below. For this series the radio frequency plasma was used at the maximum power of \_\_\_\_\_ with a constant flow of nitrogen (constant nitridation). Films were grown on c-axis oriented sapphire substrates with no use of buffer layers.

Substrates were checked for cleanliness and quality by means of the system's integrated Reflection High Energy Electron Diffraction (RHEED) system. Refer to appendix 0 for details on this piece of equipment. Substrates with a weak RHEED pattern or an amorphous surface were degreased and etched (Appendix 11.7. ).

Prior to each growth the sample holder was cleaned as per the procedure in the appendix.

Upon being placed in the chamber, the chamber is heated to the target growth temperature. Each sample was then nitrided for one-minute with a flow of \_\_\_\_\_ of nitrogen flowing through the RF plasma which was set at \_\_\_\_\_ which resulted in a chamber pressure was \_\_\_\_\_ .

#### **4.3.1.2. Discussion**

Evidence of yellow films was indicative of damage to the film caused by excess high energy nitrogen species combining at the growth interface. It was found that increasing the system pressure helped to reduce the high energy species and alleviate damage from the film. This is due to the increase in pressure causing additional collisions prior to reaching the film growth interface[29].

Figure 8 shows an AFM scan of sample 2011-06-13-1-GaN which featured a remarkably low RMS surface roughness of only .

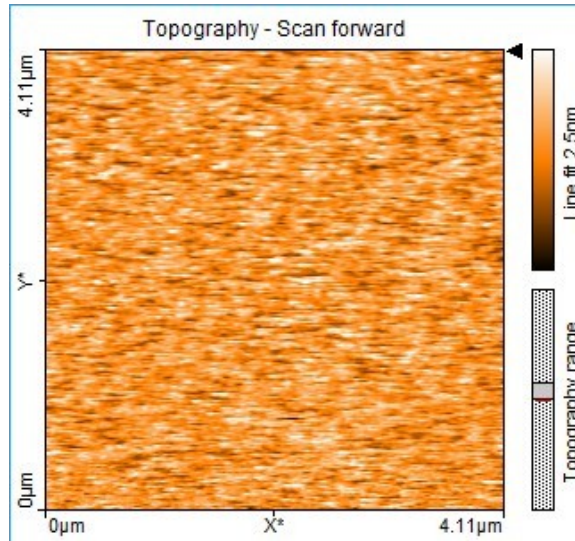


**Figure 8. 4 μm x 4 μm AFM Scan of 2011-06-13-1-GaN.**

A number of samples showed incredibly low surface roughness values. Thin films under tended to show a strong presence of powder on the surface. This powder was found to be excess metal and the implementation of a cooling cycle during film growth assisted in reducing the powder build up. Etching the sample post growth completely removed the powder on the surface.

#### **4.3.1.3. Results**

Results from this series of experiments have been published in [29] and [39]. High quality gallium faced GaN was successfully grown directly on sapphire at . Growth rates varied from to —.

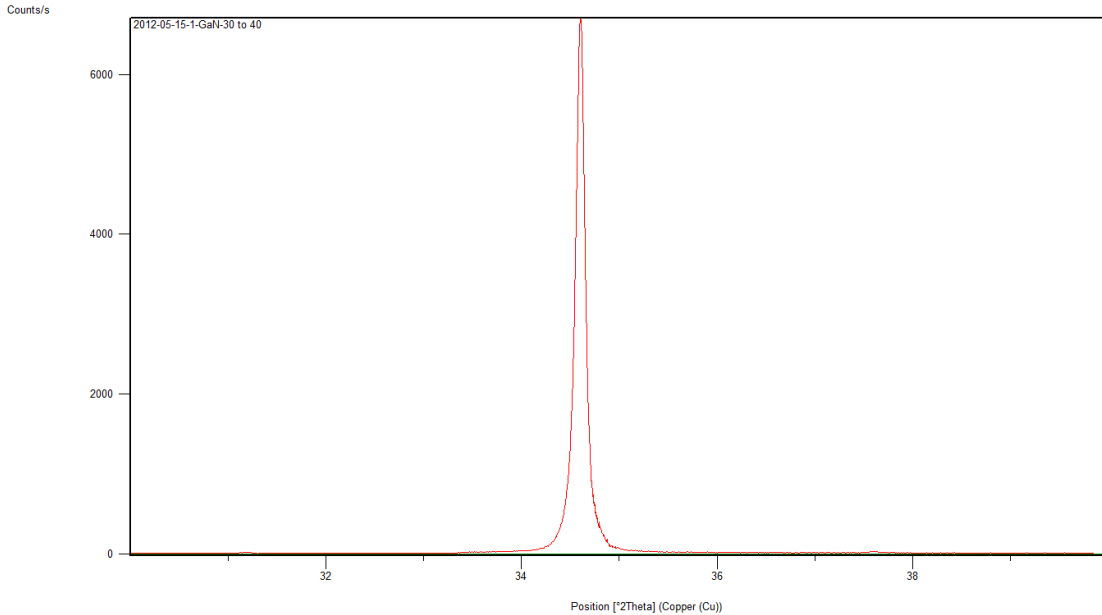


**Figure 9. XRD scan showing GaN sample with a FWHM of 0.1152.**

Surface roughness values varied widely, with samples as low as . High energy damaging nitrogen species have been reduced by increasing the system pressure. The issue of metal powder forming on the surface was improved by application of a cooling cycle.

#### **4.3.2. GaN Grown Under Various Nitrogen Flux**

In order to obtain the highest quality GaN growths the best results from the experiments detailed in section 4.3.1. were used as a basis for further refining. It is important to note that for these growths the throttle valve was not operational therefore the system could not regulate the chamber pressure. Instead the desired chamber pressure was achieved by applying a specific nitrogen flow to the system. The objective of this series of experiments was to determine what effect the chamber pressure and nitrogen flow had on the films and ultimately to refine the surface morphology and roughness of the films.

Through varying the nitrogen flux the stoichiometry of the film is altered. The GaN films grown in this series are semi-insulating with no intentional doping applied.

#### **4.3.2.1. Experiment**

For these experiments no buffer layer was used. Bare substrates as well as substrates with an titanium backing were used. Titanium backing provides an effective means of heat transfer and has been used effectively in MBE systems[22]. Bare substrate samples are analysed first. TMG flow was fixed at providing a gallium rich environment, while the nitrogen flux was varied from to . Program growth cycles were fixed at with a second time per cycle. Each cycle featured seconds of metalorganic flow followed by a plasma only nitridation for the remaining seconds. Full RF plasma power was applied and no cooling or desorption step was used. Growth temperature ranged slightly from to with an average of .

#### 4.3.2.2. Discussion

A mostly linear relationship exists between the chamber pressure and the nitrogen flow into the chamber as illustrated in Figure 10, except at the lower nitrogen flow range. This is likely due to changes in the laminar flow of the nitrogen into the chamber.

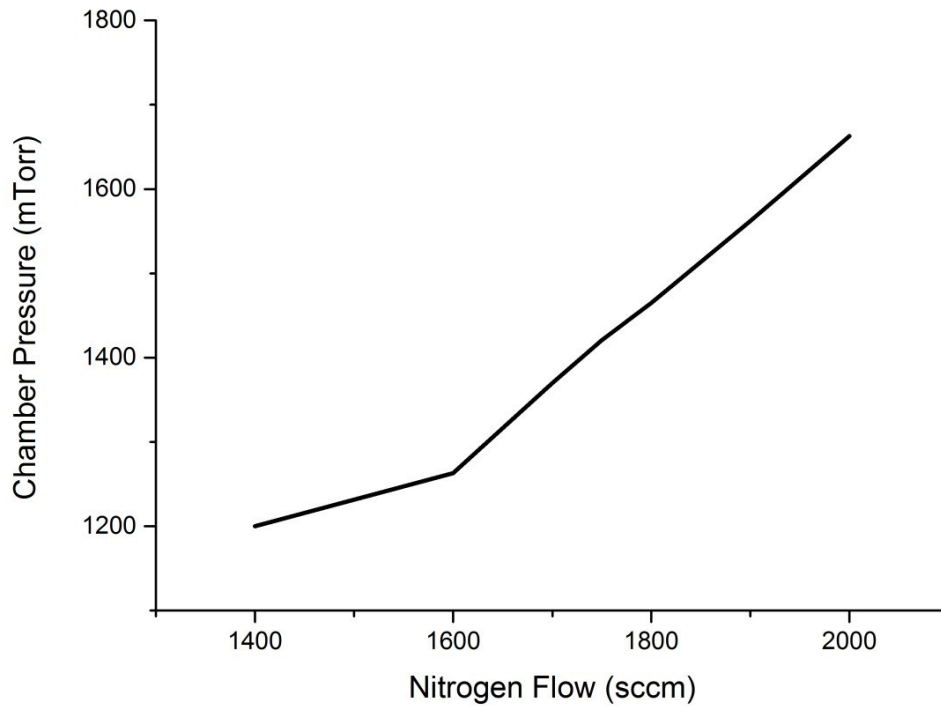


**Figure 10. Chamber Pressure vs. Nitrogen Flow for this series of experiments.**

Figure 11 shows AFM scans for this series of experiments. The corresponding nitrogen flux, chamber pressure, and resulting surface roughness are shown in Table 6.

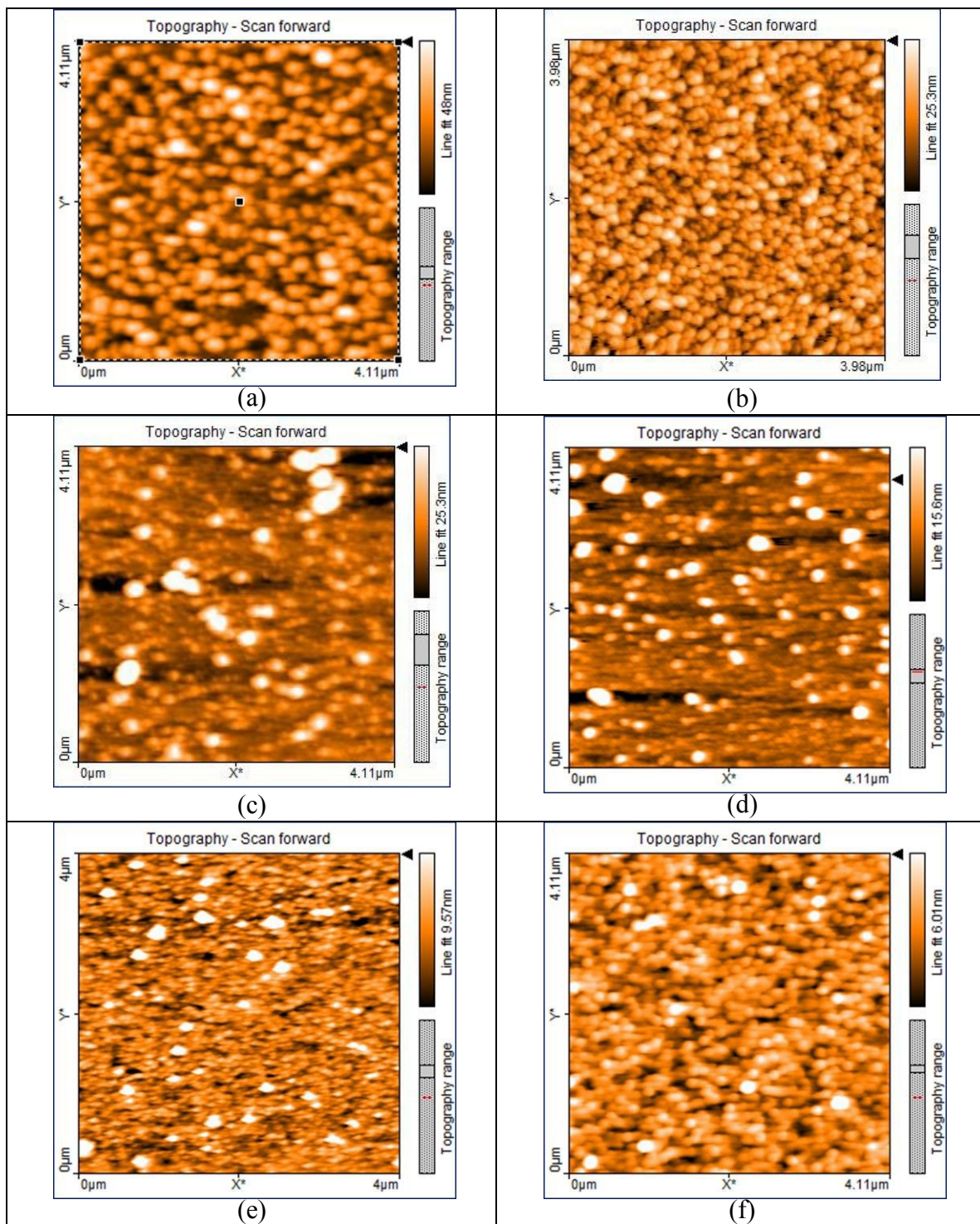


**Figure 11. AFM scans showing surface morphology.**

**Table 6. Nitrogen flow, chamber pressure, and surface roughness for the samples in Figure 11.**

Sample Label	Sample Name	Nitrogen Flow ( )	Chamber Pressure ( )	Surface Roughness (RMS, )
(a)	2012-04-09-1-GaN			
(b)	2012-04-24-1-GaN			
(c)	2012-04-24-2-GaN			
(d)	2012-04-10-1-GaN			
(e)	2012-04-16-2-GaN			
(f)	2012-04-10-2-GaN			

The mid-range flows of (c) and (d) show evidence of surface droplets formation which correlates with the roughness of the surfaces. All samples show the presence of droplets. however these droplets vary in count and size.

Looking at Figure 12 below, the rise in growth rate correlates to the rough surface morphologies for samples among the mid-range of nitrogen flux. This is likely due to the rise in droplet formation as evidenced by the AFM scans in Figure 11. The maximum growth rate for this set of conditions occurred at of nitrogen flux.

Interestingly this sample actually showed a drop in surface roughness. Referring to the AFM image in Figure 11 (b) it is clear that this sample exhibits the smallest crystals with little to no droplet formation.

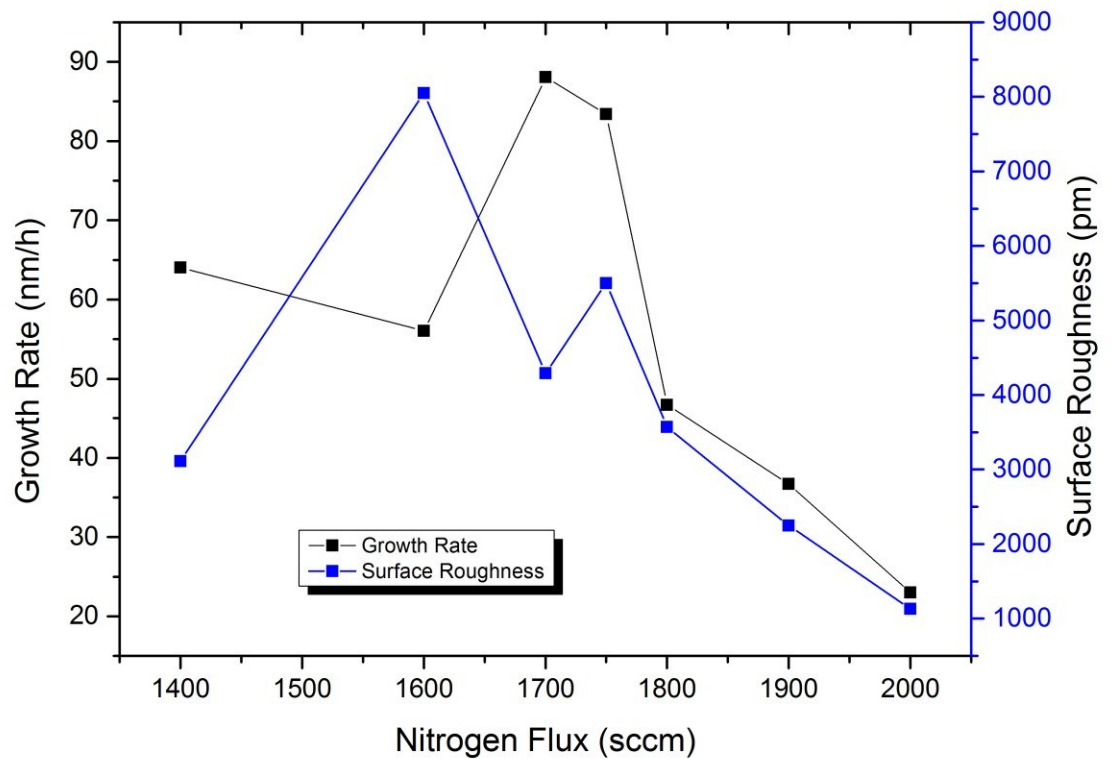


**Figure 12 Growth rate and surface roughness for non-titanium backed samples vs. nitrogen flux.**

For many growth systems, the growth rate will increase as a function of the nitrogen flux[48]. This has proved true in this experiment to a point. Once droplet forming begins to occur the growth rate decreases however the underlying crystals remain small. It is clear that a critical operating point has been identified for these particular growth conditions at around 1700 of nitrogen flux.

**4.3.2.3. Results**

With no active control the system pressure varied directly with nitrogen flux. These experiments have mapped out this parameter space. Variation of the growth rate as it

relates to system pressure has been observed with growth rates varying from to — with a peak growth rate occurring at a system pressure of . This critical parameter space point was used as a basis for further experiments.

### **4.3.3. GaN Buffer Layers**

In this series of experiments the possibility of growing very thin film buffer layers to improve subsequent film growth layers has been evaluated along with the effects of GaN buffer layers on the overlying films. Bare sapphire substrates as well as those with various thickness of titanium backing were evaluated. Buffer layers are typically grown very slowly in order to maximize the quality of the film and are undoped. GaN buffer layers are used as templates to improve the quality of the overlying InN or GaN films[34].

#### **4.3.3.1. Experiment**

Chamber pressure was held constant by means of the throttle plate and nitrogen flux was fixed at for most samples. Growth temperature range from to . Growth cycle counts and times ranged from to cycles and to —. No outer cycle wait period was featured in these growths. Most samples featured a total growth time. Metalorganic injection times ranged from to seconds. RF Power was held constant at full . Most samples featured a TMG flow of and all samples were grown metal modulated.

#### 4.3.3.2. Discussion

A basis for comparison was selected from previous work with a low surface roughness of [redacted] and sharp XRD peak of [redacted]. Figure 13 (a) shows the side profile of this sample and indicates a very smooth surface. Though difficult to quantify, the resulting film was smooth and uniform throughout the scanned area.

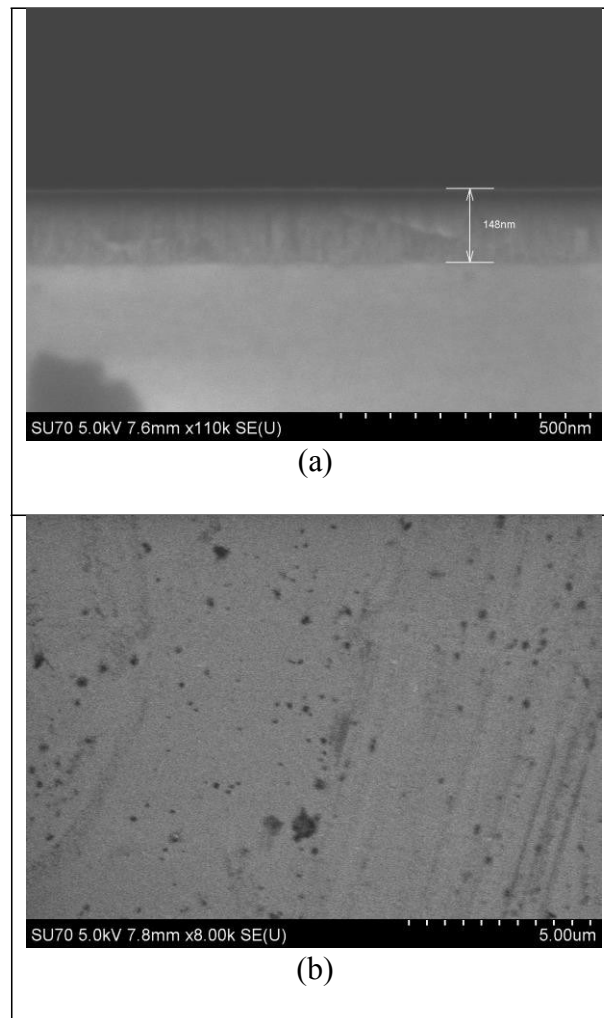


**Figure 13. SEM images showing the profile and surface of one sample with a measured RMS surface roughness of 386  $\mu\text{m}$ .**

This particular sample was grown on a titanium backed substrate. The heat distribution during growth is improved for titanium backed samples reducing heat island effects and improve the surface morphology of the resulting film. However Figure 13 (b) shows evidence of pitting on the surface, which may be indicative of v-defects. This sample was then used as a basis for further refinements. As a limited quality of titanium backed substrates were available, further attempts to improve the film used non-backed substrates. The time per cycle and metalorganic duty pulse were adjusted. The optimal time per cycle appeared to be seconds based on surface roughness, apparent bandgap (through optical measurements) and XRD peak analysis. The metalorganic duty pulse was then adjusted to further improve the surface with the optimal time found to be seconds. An AFM of the resulting film is shown in Figure 14.

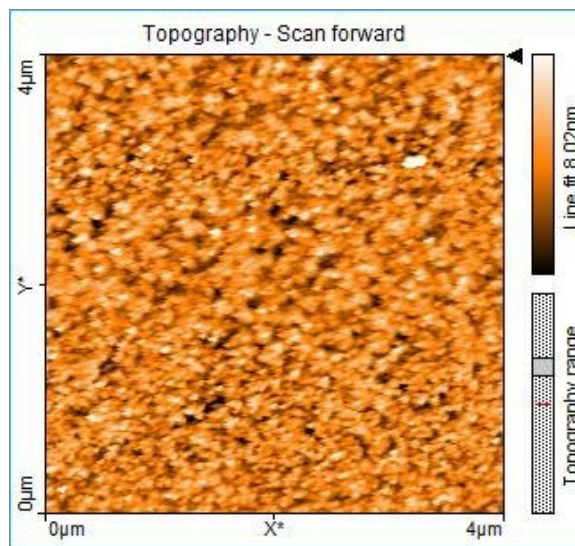
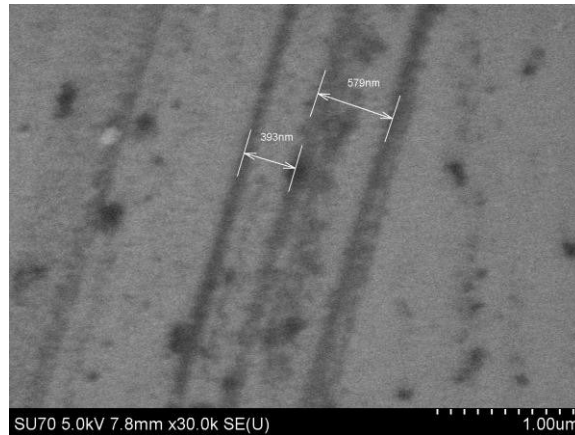


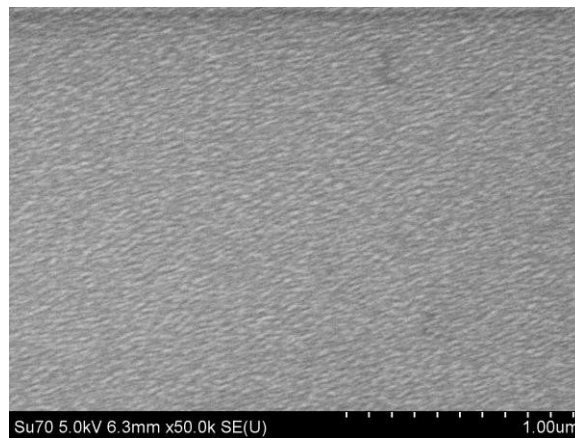
**Figure 14. AFM scan of the resulting buffer layer.**

The improved film was grown without a titanium backing on the substrate. Adding a titanium backing and reducing the cycle count by a factor of 10 produced the film shown

in Figure 15 (b). Though this film is only 34 nm thick, implying a great degree of strain must exist, it is very defect-free and shows great promise for use as a buffer layer.



(a)



(b)

**Figure 15. (a) SEM image showing a scratch on the sample shown in Figure 13. (b) The refined film showing less defects.**

#### 4.3.3.3. Results

A suitable buffer layer has been grown with and without a titanium backing. Though optical measurements are not possible with titanium backed samples, the non-backed sample showed a band gap of            at a thickness of            with a surface roughness

of \_\_\_\_\_ and a sharp XRD peak at 0.1152 FWHM. Growth rates ranged from \_\_\_\_\_ to \_\_\_\_\_.

#### **4.3.4. GaN Grown with Desorption Step**

In this series of experiments, attempts were made to apply a desorption step to gallium nitride growth. This is a popular technique in MBE systems for indium nitride growth[13]. The added delay allows for additional adatom diffusion at the surface[34]. The desorption rate of GaN films is highly dependent on system parameters (such as pressure, nitrogen flux) and increases with temperature[14]. It is therefore anticipated that some desorption will occur at a growth temperature of approximately \_\_\_\_\_. With other parameters fixed, a desorption step was added to the standard GaN film program listed in Figure 6. The step consists of an outer loop utilizing a waiting period to allow for the desorption occur. The waiting time was varied and the results were observed. Samples were grown on bare sapphire – no titanium backing was used.

##### **4.3.4.1. Experiment**

A basis for comparison was selected based on previous growths. The sample featured a relatively smooth surface at \_\_\_\_\_, with a band gap of \_\_\_\_\_. Thickness was approximately \_\_\_\_\_ with an XRD FWHM of \_\_\_\_\_ shown in Figure 16.

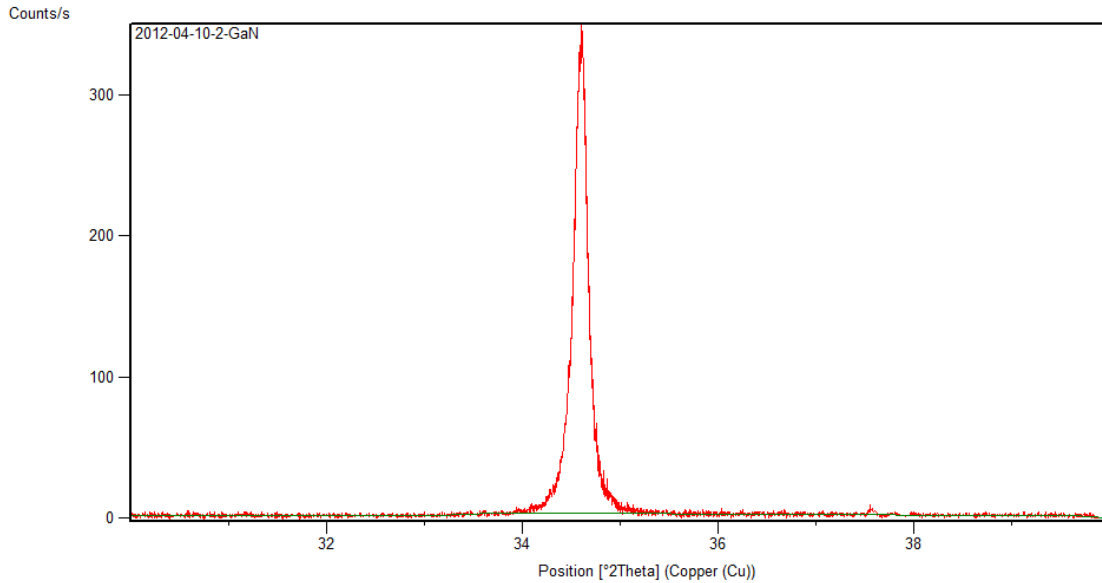


**Figure 16. XRD scan with FWHM of 0.1536 °2-theta.**

The modified program flow chart is shown in Figure 17. All samples were grown metal modulated with —, and at of metal organic pulse time representing a duty cycle. Growth temperatures were relatively similar varying between and . Nitrogen flow was fixed at while the chamber pressure was held at . TMG flow was fixed at . Total growth times varied accordingly as the desorption step was adjusted. The desorption step occurred once every ten growth cycles for all samples.



**Figure 17. Modified GaN film growth flow chart showing desorption step.**

#### 4.3.4.2. Discussion

Figure 18 shows the resulting surface roughness for each desorption time attempted along with the resulting growth rate.

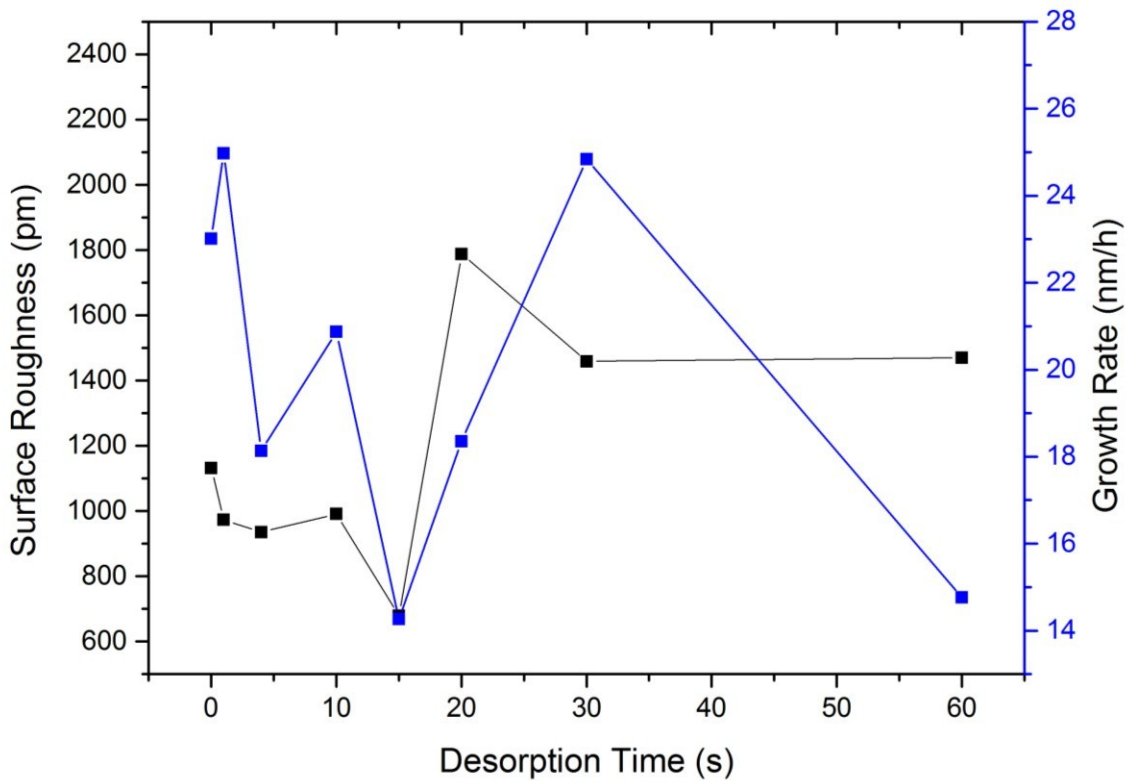


**Figure 18. A correlation exists between the sample growth rate and resulting surface roughness.**

An optimum desorption step time of 15 s was evident based on surface roughness measurements. It is clear that the surface roughness and growth rate share a correlation with the smoothest samples occurring at the lowest growth rates. This is common for this type of growth system. Both the growth rate and surface roughness share a common minimum point, indicating that this may be a critical operating point. Many factors affect the growth rate and one of the greatest influences is temperature. Lower temperatures see lower growth rates. It is interesting to note that for this sample the growth temperature

was right in the middle range of the temperature variation throughout the sample set. We can thereby conclude that the slow growth rate is not a result of the growth temperature in this case.

#### **4.3.4.3. Results**

It has been shown that implementation of a desorption step during growth can improve the surface morphology of the film at the cost of reduced growth rates. An optimal desorption step time of was found for this set of growth conditions.

#### **4.3.5. GaN Grown Under Various TMG Flows**

For this series of experiments the effect of TMG flow during growth is evaluated for two sets of growth conditions on bare sapphire substrates with no titanium backing. In the first set of experiments the effect is evaluated to quickly grown samples with a low cycle count. The optimum condition is then applied to a higher cycle count sample. For the second phase of the experiment the effect is evaluated on thicker samples with much longer growth times and cycle counts.

The resulting surface morphology and roughness are compared as well as the resulting film band gap, overall film thickness, and XRD peaks.

##### **4.3.5.1. Experiment**

In the first phase of this experiment samples are grown quickly on monocrystal substrates with a low cycle count of and a duty cycle MO on-time. Average growth

temperature for these films was . Total time per cycle was with no outer cycle waiting period. Chamber pressure was maintained at with nitrogen flow at . TMG flows were evaluated through a range of to . Full RF power was employed in the plasma head.

The second series of films were grown with no titanium backing but at a slightly elevated temperature of . Cycle counts were increased to with per cycle and a MO duty cycle. Chamber pressure and nitrogen flux remained the same. TMG flows range from to . Full RF power was used.

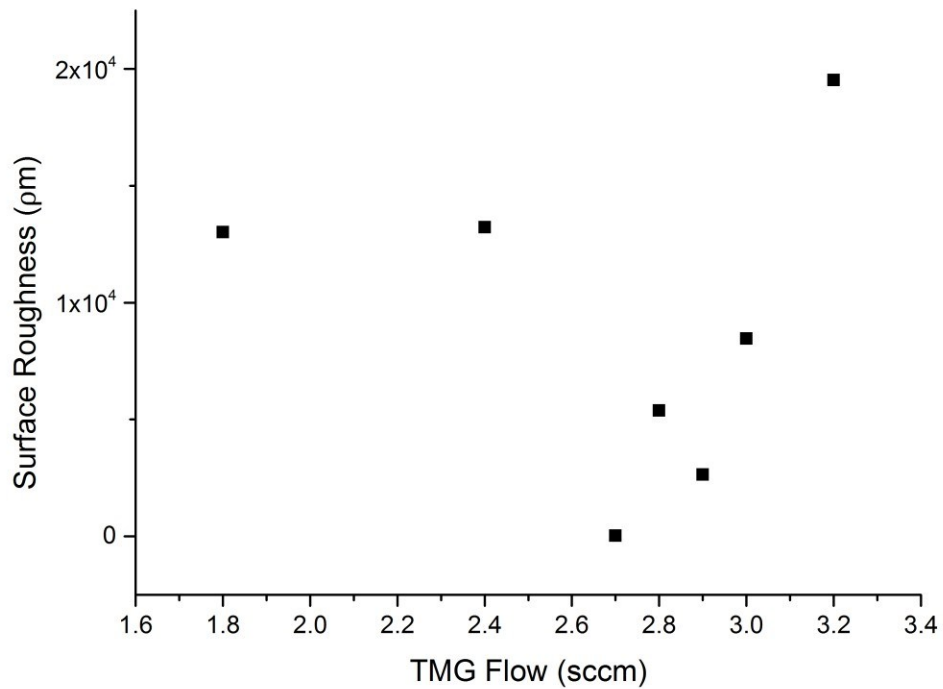


**Figure 19. Surface roughness results from various TMG flows.**

#### 4.3.5.2. Discussion

The resulting surface roughness versus input TMG flow is shown in Figure 19.

The surface roughness increased with TMG flow but quickly dropped after .  
The smoothest surface was recorded for a TMG flow before quickly rising. A  
closer look at the surface morphology is warranted.

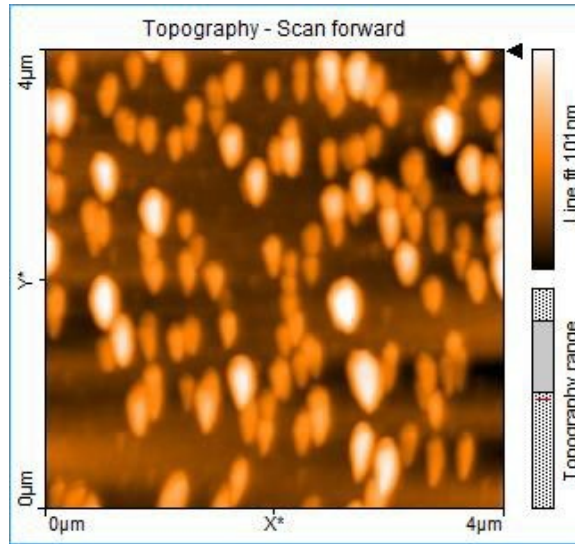


**Figure 20. AFM image of sample growth with 2.7 sccm of TMG.**

Observing Figure 20 grown with of TMG, we can see droplets have formed on  
the surface with a smooth surface morphology existing in between. Because of the  
droplets the roughness is quite high at .

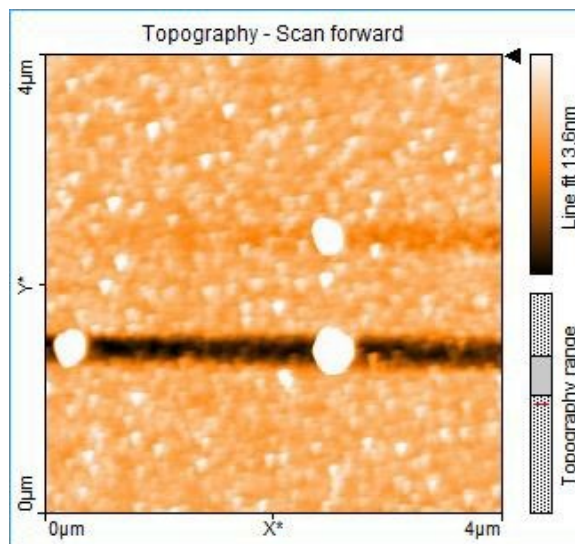


**Figure 21. AFM image of sample grown with 2.8 sccm of TMG.**

The film in Figure 21 with a TMG flow of \_\_\_\_\_ shows an improved surface morphology with less droplets, however some are still present. The roughness improves accordingly to \_\_\_\_\_.

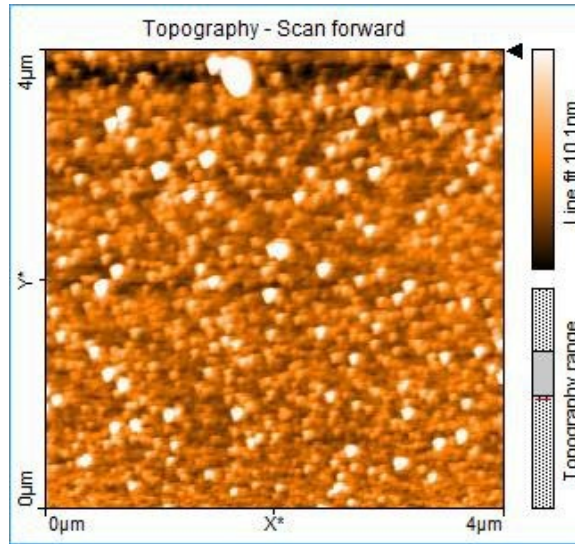


**Figure 22. AFM image of sample grown with 2.9 sccm of TMG.**

Further increasing the TMG flow to \_\_\_\_\_ results in the improved film observed in Figure 22 with a roughness of \_\_\_\_\_.

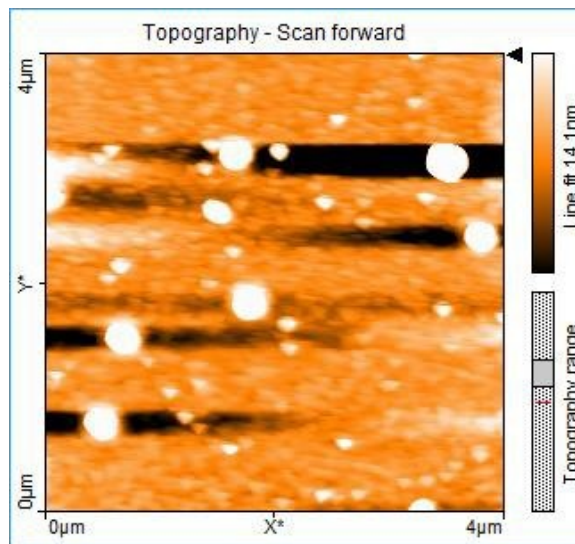


**Figure 23. AFM image of sample grown with 3.0 sccm of TMG.**

Upon increasing the TMG flow further however, the droplets again start to form.

Roughness increased to

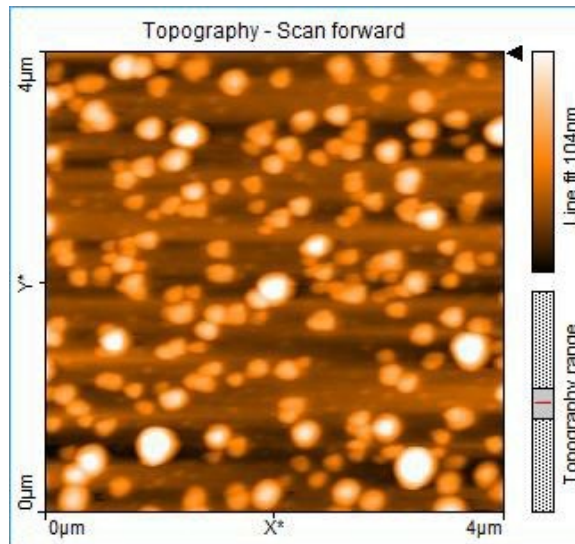


**Figure 24. AFM image of sample grown with 3.2 sccm of TMG.**

Increasing the TMG flow to further promotes droplet formation resulting a surface roughness of . It can then be deduced that for the first set of growth conditions using a low cycle count of only , the optimum TMG flow is approximately . Having now established a suitable TMG flow condition, the application of this flow was applied to a thicker film.

We now wished to establish an optimum TMG flow for thicker films grown through many more cycles. The thicker films produced rougher surfaces as expected with the results shown in Figure 25.

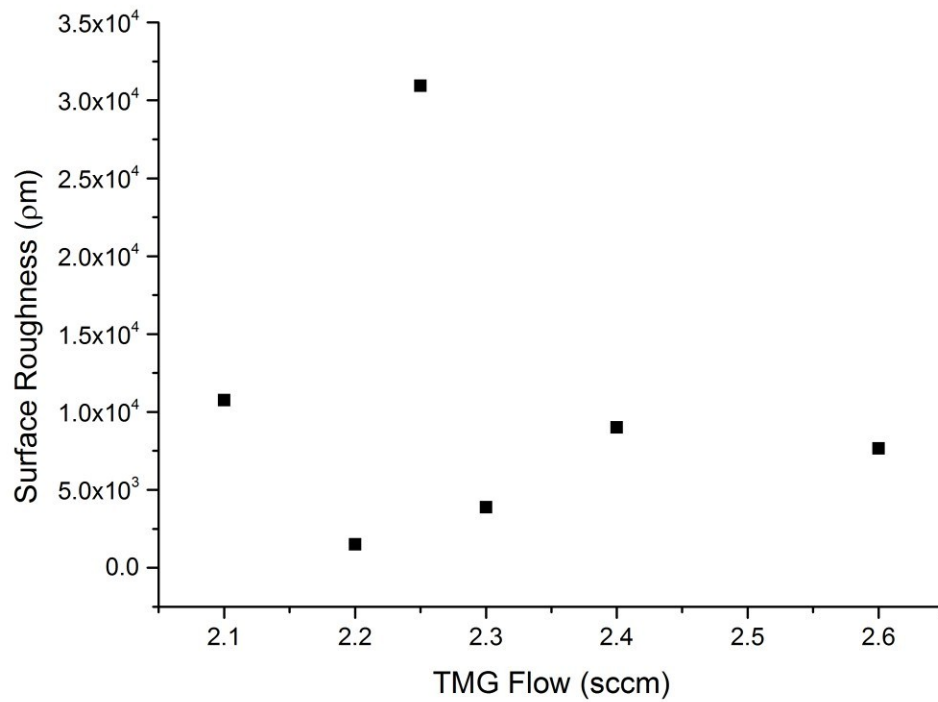
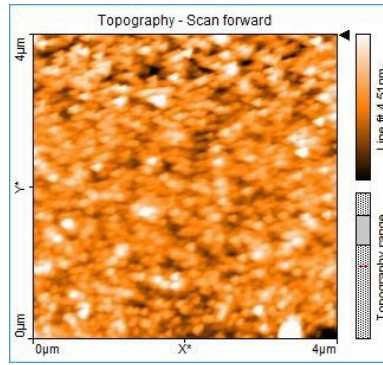
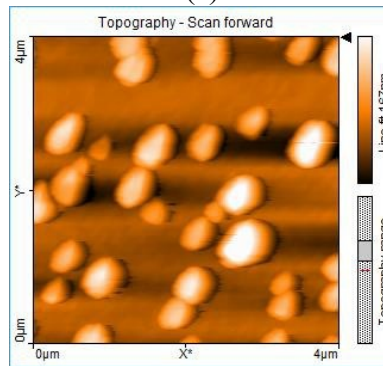


**Figure 25. Resulting surface roughness for thicker films.**

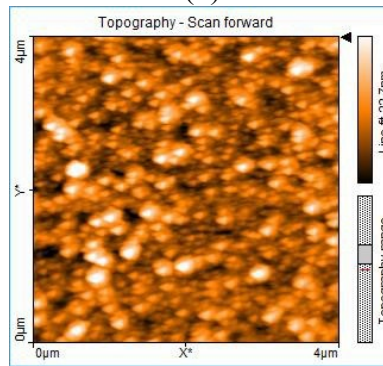
Peak roughness occurred at 2.25 of TMG flow indicating some operating critical point. Either side shows improved roughness.



(a)



(b)



(c)

**Figure 26. AFM scans for (a) 2.2 sccm of TMG flow, (b) 2.25 sccm, and (c) 2.3 sccm.**

The highest surface roughness occurred with the sample shown in Figure 26 (b) with clear droplet formation though a very smooth film exists between droplets measured at

. Figure 26 (a) and Figure 26 (c) show a vastly improved surface roughness with relatively small crystals and little droplet presence.

#### **4.3.5.3. Results**

An optimum TMG flow has been established for thin films grown under long cycle times at . The thicker films showed a preference for a lower TMG flow with a critical point established at . It is suggested that future work involve the application of a TMG flow which is reduced as the film grows thicker.

#### **4.3.6. GaN Grown Under Varying Plasma Only Time**

In this series of experiments the metalorganic on-time was fixed while the plasma only time varied. The effect of the plasma only time is evaluated on sample morphology through the use of XRD, and AFM. Monocrystal substrates with no titanium backing were used for all growths.

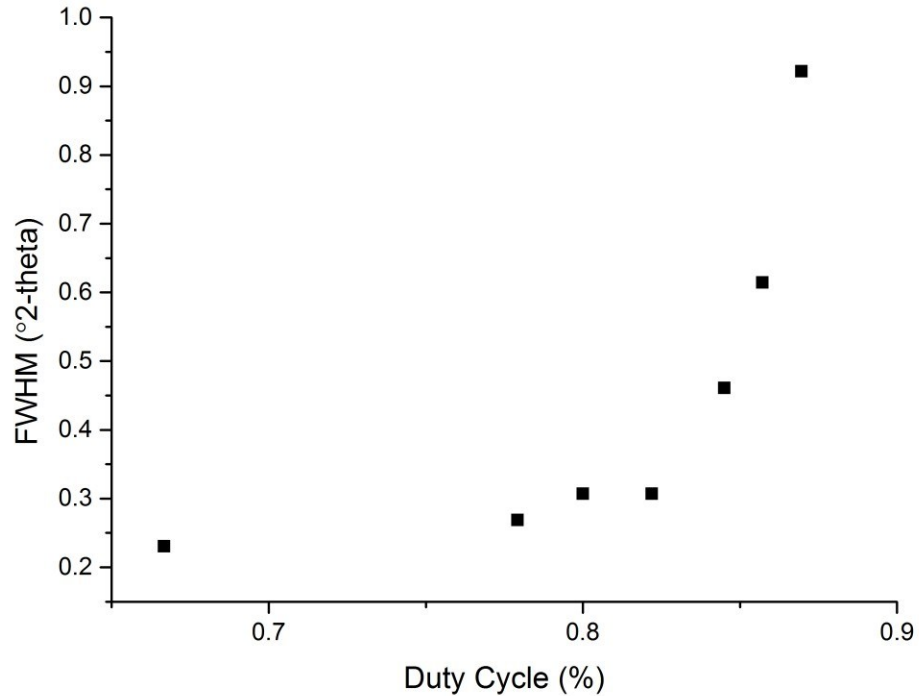
##### **4.3.6.1. Experiment**

Growth temperature was held constant at approximately for all growths. All growths featured cycles except for the duty cycle sample which had only one cycle and the growth time was set to be comparable to the other samples. Chamber pressure was fixed at and nitrogen flux through the plasma head was . MO flow rate was set to .

The MO off time is expressed as a duty cycle for each growth loop. was selected as a starting point.

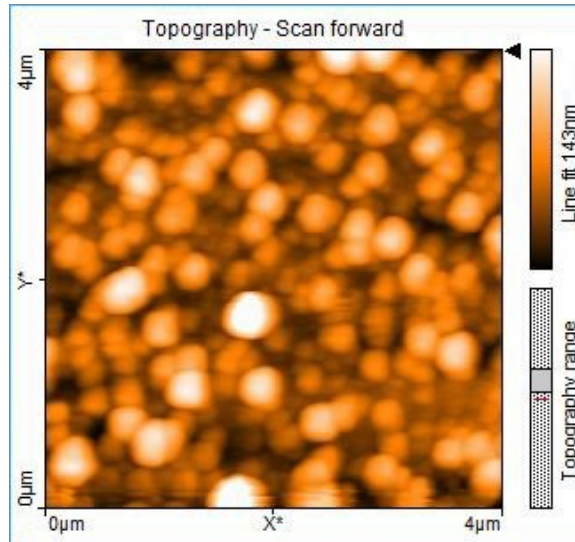
#### 4.3.6.2. Discussion

As the MO off time is reduced, the duty cycle increases resulting in a shorter plasma only time per cycle.



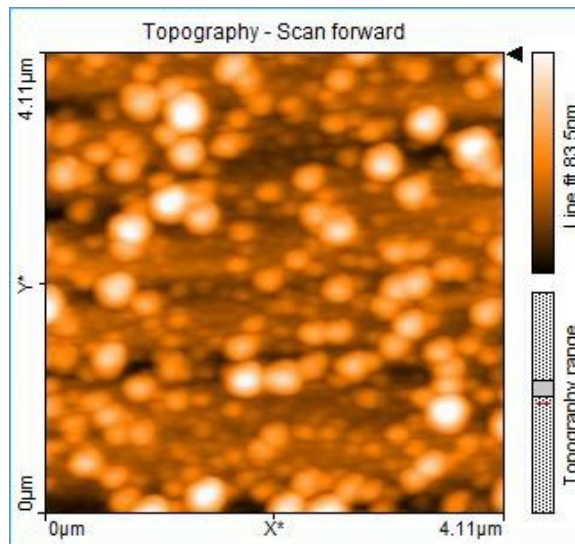
**Figure 27. Resulting XRD FWHM for the various MO duty cycles.**

Figure 27 shows the XRD FWHM increasing with increasing duty cycle. This implies that the film becomes more polycrystalline as plasma only time is reduced. The sample with no plasma only time ( duty cycle) had no detectable XRD peaks, indicating a sample of very poor quality crystal structure. AFM for the duty cycle sample is shown in Figure 28.



**Figure 28. AFM scan for the 4.5 s plasma only time (0.87% duty cycle) sample.**

The surface appears very polycrystalline and shows a very poor surface roughness at  $4.5 \mu\text{m}$ . This sample featured a plasma only time of  $4.5 \text{ s}$ . Increasing the plasma only time to  $5.5 \text{ s}$  per cycle resulted in the film shown in Figure 29.



**Figure 29. AFM scan for the 5.5 s plasma only time (0.85% duty cycle) sample.**

This film has a slightly improved surface morphology showing some smaller crystals present and a smoother surface at  $5.5 \mu\text{m}$  over two times improved by the application

of merely second of additional plasma only time. Increasing the plasma only time second further results in an even smoother surface at similar in appearance to Figure 29. However upon increasing the plasma only time further to does not realize any further improvement in surface roughness. The result is shown in Figure 30.

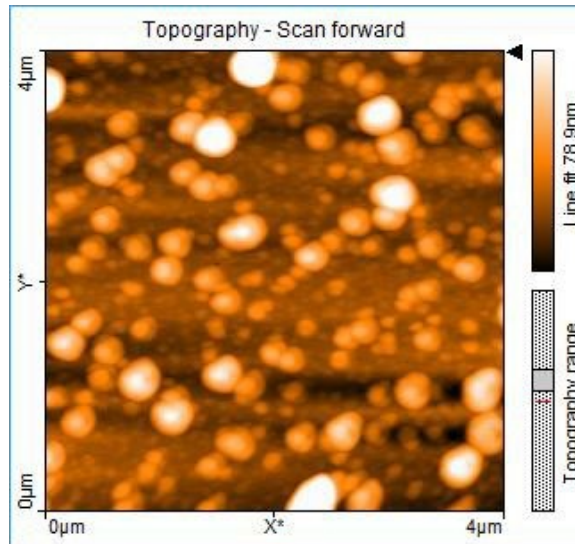


**Figure 30. AFM for 7.5 s plasma only time (80% duty cycle).**

The plasma only time sample showed a rough surface of and yielded little if any improvement in the XRD. An additional second of plasma only time did improve the XRD FWHM from to , however surface roughness remains poor.

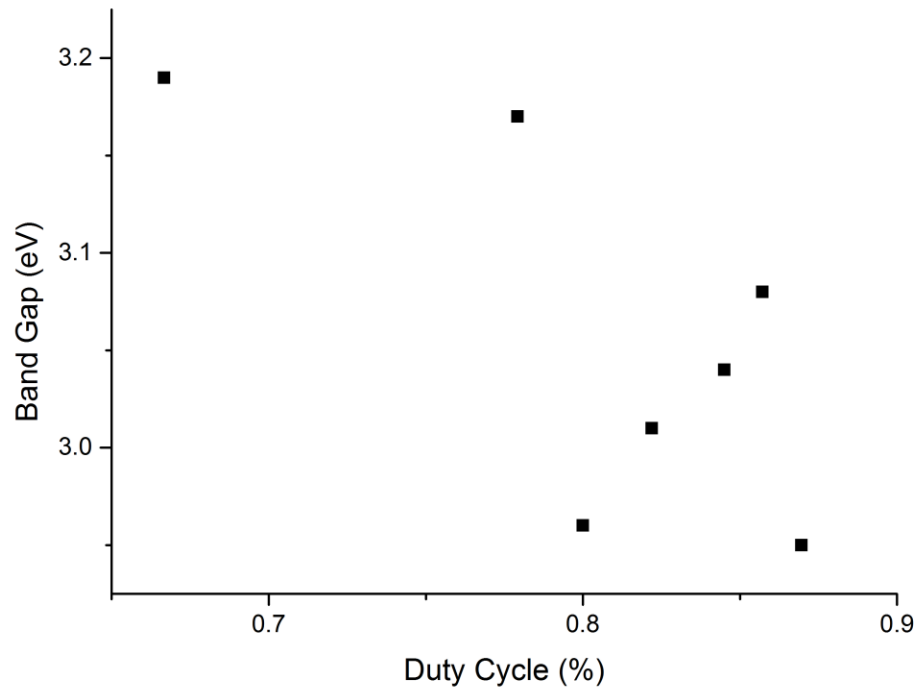


**Figure 31. Resulting band gap values.**

Looking at the band gap values shown in Figure 31 we can see that the lower duty cycle samples tended to have band gaps closer to the true value for a GaN film.

#### **4.3.6.3. Results**

Complete removal of the plasma only nitridation time during growth resulted in a film of incredibly poor quality and polycrystalline makeup. The addition of the plasma only time improves bulk crystal growth quality though the surface may suffer due to droplet formation. As XRD shows improvements in crystal quality, the band gap also increases towards an ideal value.

## **4.4. Indium Nitride Film Growth**

Early work in the growth of indium nitride at the Lakehead University Semiconductor Research Lab was an especially exciting time. Much like the early growths of GaN many large leaps and bounds were made. Growth parameters were largely being modified to hone in on good starting points for further experiments.

InN growth poses a number of particular challenges further to those in the growth of GaN, some of which were discussed in Chapter 2. The experiments in this section hope to overcome some of these challenges using the MEAgrow growth reactor.

InN is a conductive material and as such allows for further analysis over GaN through the use of electrical measurements to assist in classifying film quality. Specifically we employ the use of Hall Effect and conductivity checks to characterize films.

Film growth results which have been published range from smooth monocrystal films showing 2D growth [49] to the formation of nanostructures[5].

### **4.4.1. General Indium Nitride Growth**

As with GaN film growth, early work film growth was very much an effort in educated guesswork by varying growth parameters largely to obtain starting points for further more correlated growths. This section discusses some of these loosely correlated experiments.

Grown films vary between smooth films tending towards 2D single crystal growth to rough polycrystalline films, while other growth conditions cause the growth of nanostructures. Most growths were metal modulated.

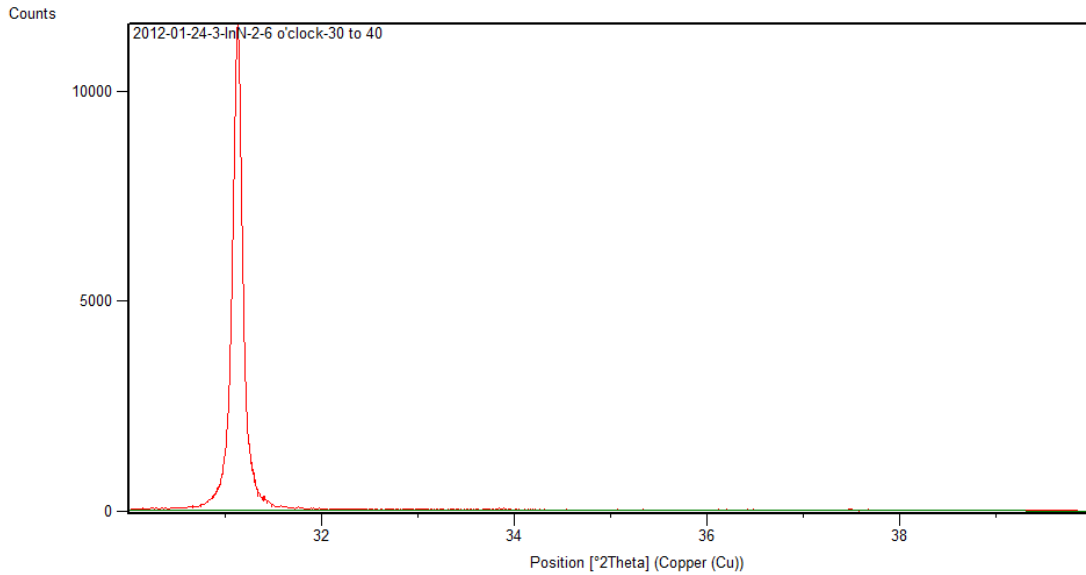
#### 4.4.1.1. Experiment

A wide range of growth conditions were employed during these growths. The system also went through a number of changes such as the addition of an electrostatic grid, which is able to be biased with a DC power supply. In general InN growths are much lower temperature than GaN ranging from      to      . Some growths use an outer cycle waiting period. Substrates used include monocrystal sapphire, commercial TDI GaN templates, and re-used lab grown GaN templates. Chamber pressures between      and      were used. Most growths used the maximum      RF power, however some improvements to the RF connector allowed for more power to be applied to the plasma head (reduced losses in transmission), and as such the power during growth was reduced accordingly to comparable levels.

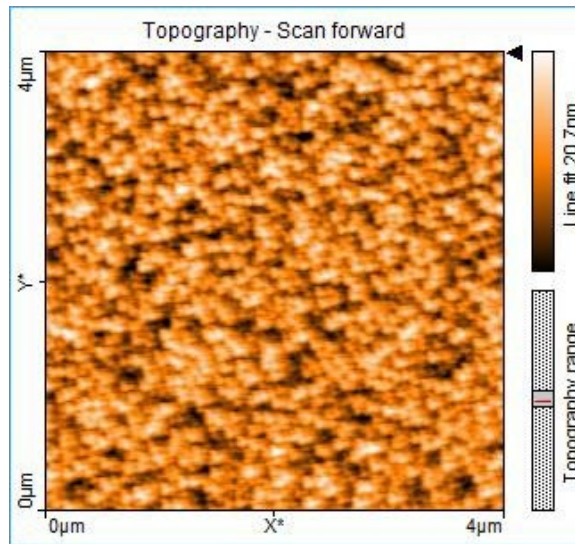
#### 4.4.1.2. Discussion

One of the most important samples produced due to its many applications throughout this body of work is shown in Figure 33. Though not entirely optimized, this sample was produced using the program structure which became the template for much of the later work. This particular sample and many repeats of it were used as the basis for many of the heterostructure growth experiments discussed in section 4.5. It is a low temperature growth at      employing no outer cycle wait period, a cycle time of      with a MO on time of      . A low chamber pressure of      along with a nitrogen flow of      and      of TMI is used. Full      RF power is applied. The sample is relatively smooth (      ) for its thickness at an estimated      based on UV-

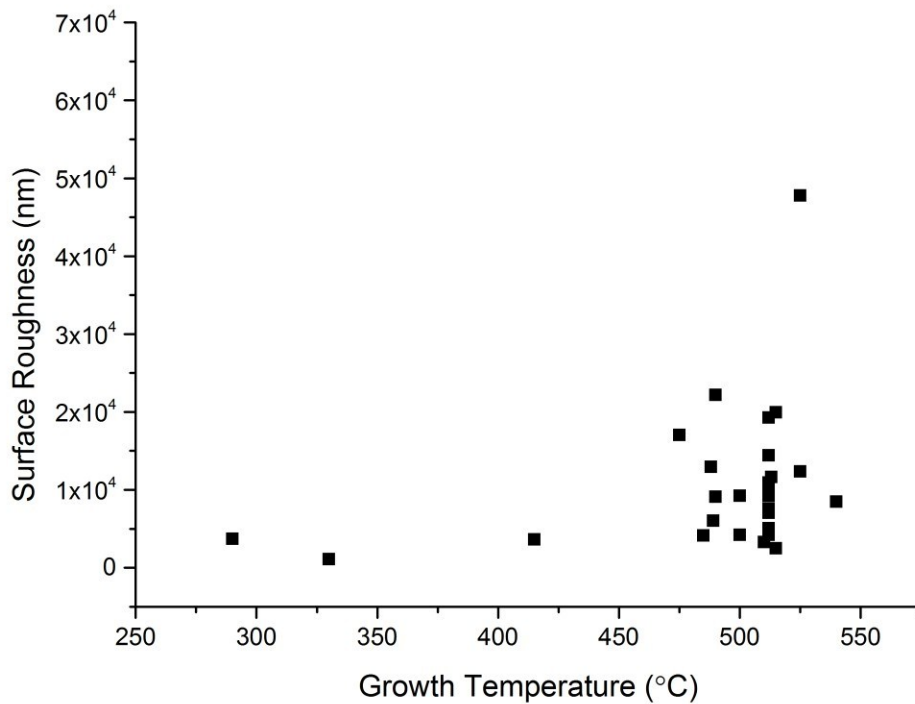
Vis analysis. XRD analysis shows a sharp (002) InN peak at a FWHM of shown in Figure 32.



**Figure 32. XRD for 2012-01-24-3-InN showing a FWHM of 0.1152 °2-theta.**

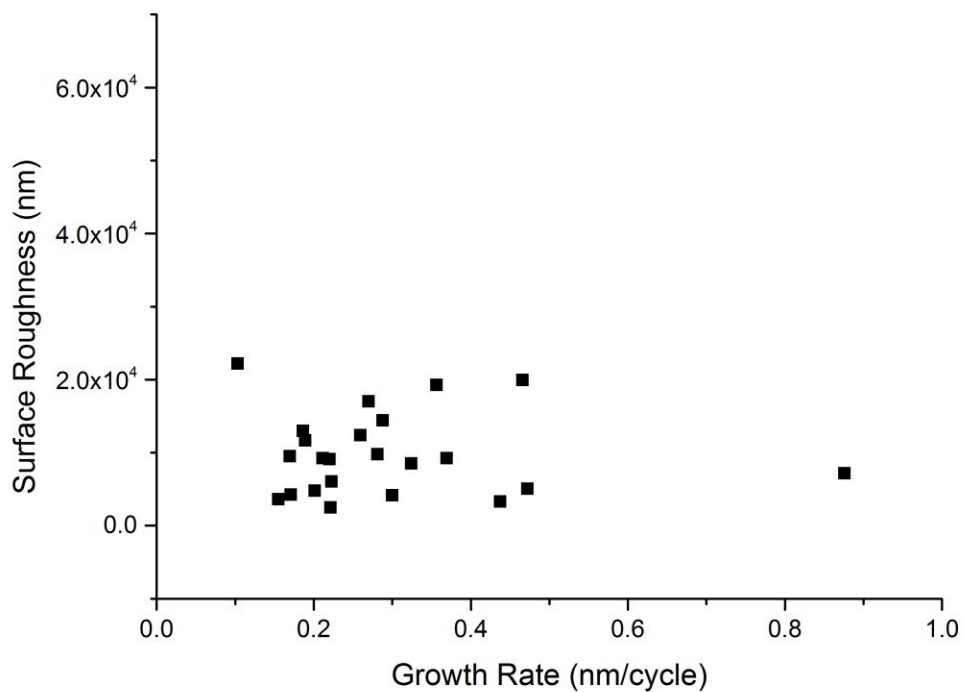


**Figure 33. AFM for 2012-01-24-3-InN with a surface roughness of 3,715 µm.**



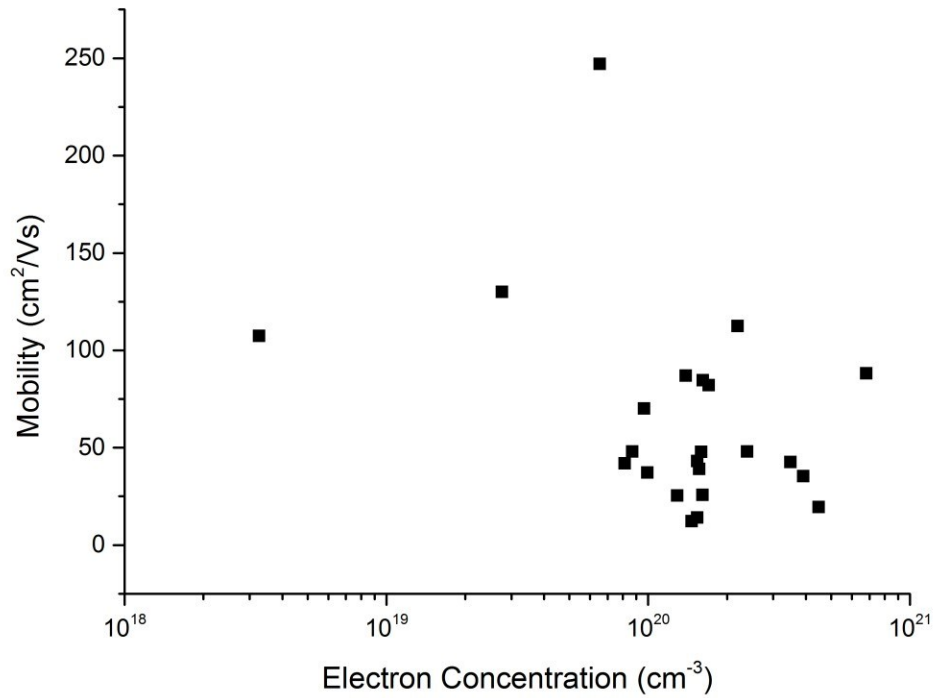
**Figure 34. Resulting surface roughness for the range of growth temperatures.**

Figure 34 shows a large number of general indium nitride film growths with the resulting surface roughness based on growth temperature. Most growths occurred around . At this temperature range some desorption of the indium nitride can be expected and this attribute is used to improve surface morphology. Surface roughness generally can be expected to improve as the growth temperature is lowered, however the surface roughness does not dictate that the film is of better quality in terms of electrical characteristics.



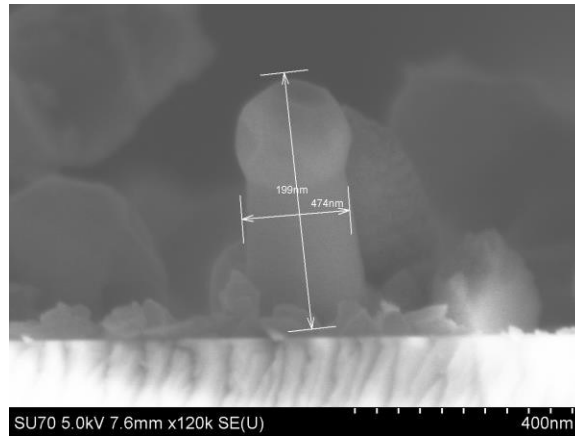
**Figure 35. Growth rate vs. surface roughness.**

Too high a growth rate can often lead to compromised film crystallinity. Surprisingly there does not appear to be a tight correlation between growth rate and the resulting surface roughness. This may be due to the wide range of growth conditions employed.



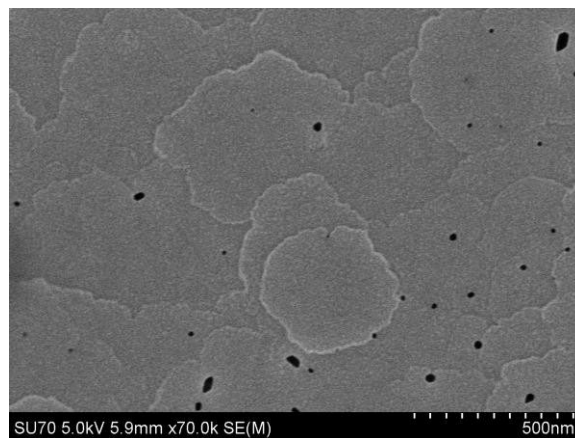
**Figure 36. Electron mobility vs. concentration for a number of indium nitride samples.**

Figure 36 shows a quick snapshot of some of the obtain indium nitride results based on a popular method of classifying electron concentration vs. mobility. Most samples featured carrier concentrations in excess of  $10^{20}$  cm<sup>-3</sup>. Samples exhibiting a high mobility with a low carrier concentration indicate a lower compensation level[10].



**Figure 37. Nanowires 2012-04-05-1-InN.**

Certain growth conditions have led to the formation of nanostructures on the surface. Pyramids, orbs, pillars, and wires have all been formed. Figure 37 shows one such nanopillar which formed. This growth featured a long one-minute cycle time with a MO duty cycle. Chamber pressure was high at \_\_\_\_\_ with \_\_\_\_\_ of nitrogen and \_\_\_\_\_ of TMI. Nanostructure growths are further discussed in section 4.6.



**Figure 38. 2013-05-08-1-InN showing 2D island growth.**

Another important film is shown in Figure 38. This film clearly shows the growth of 2D islands indicating epitaxial growth and good surface morphology. However pitting defects are clearly evident. XRD scans show a very sharp 0.0312 FWHM InN peak indicating a high quality monocrystal structure. This quality film was obtained using a

GaN template for growth at a moderately high temperature of . A relatively low chamber pressure of and low nitrogen flow rate of were used. TMI input was set at .

#### **4.4.1.3. Results**

The wide range of growth conditions and system changes throughout these growths has led to a wide range of films from single crystal to nanostructures forming on the surface.

Conditions have been established for the growth of nanowires which is further explored.

Monocrystal films with smooth surfaces require a high quality buffer layer.

Complete optimization of the indium nitride films was not the goal of this work, rather these early indium nitride growths served to provide a template for future experiments in the growth of heterostructures.

#### **4.4.2. InN Grown Under Various Plasma Only and Plasma + Setup Times**

Referring to Figure 7, these growths varied the “Plasma + Setup” and “Plasma Only” steps of the film growth. In the “Plasma Only” step the plasma head is on with no metalorganic flowing through the feed lines. During the “Plasma + Setup” step metalorganic is introduced to the feed lines to allow for flushing and stabilization of flow within the feed line. The MO however is not injected into the chamber at this time since the bypass is enabled. In this step the plasma is on with a constant nitrogen flow while the metalorganic lines are prepared/flushed. Some desorption of InN can be expected during

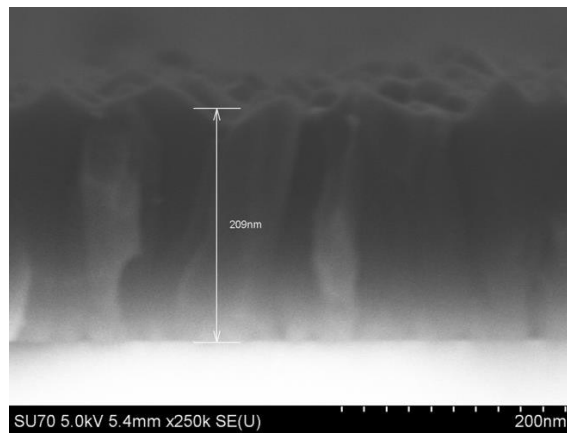
this step despite the relatively low average growth temperature of causing the formation of metallic indium[50].

#### 4.4.2.1. Experiment

Fixed growth parameters include a continuous RF plasma, seconds of metalorganic input time, chamber pressure fixed at , a nitrogen flow of , and TMG input was set to . The plasma only time was varied between and seconds. Outer loop counts were adjusted to keep total growth time approximately the same.

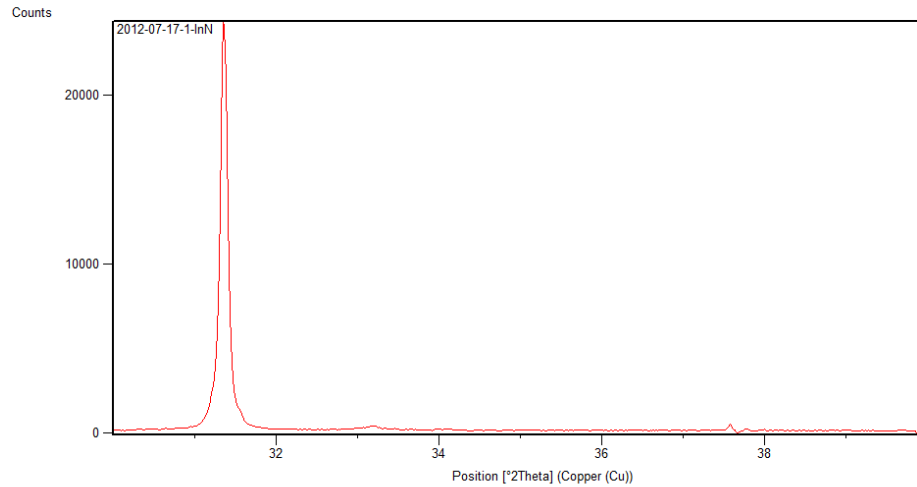
#### 4.4.2.2. Discussion

The “Plasma only” time was set to 15s with an initial “Plasma + Setup” time set to 10s. The resulting indium nitride film is shown in Figure 39.



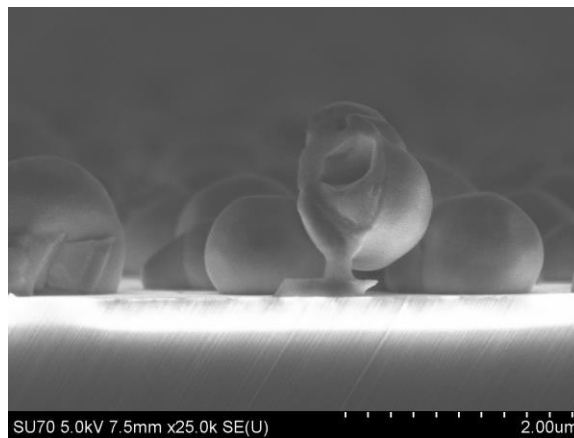
**Figure 39. 15s plasma only, 10s plasma + setup time.**

The resulting film shows a fairly rough but uniform film approximately thick. AFM roughness was measured to be . An XRD scan is shown in Figure 40.



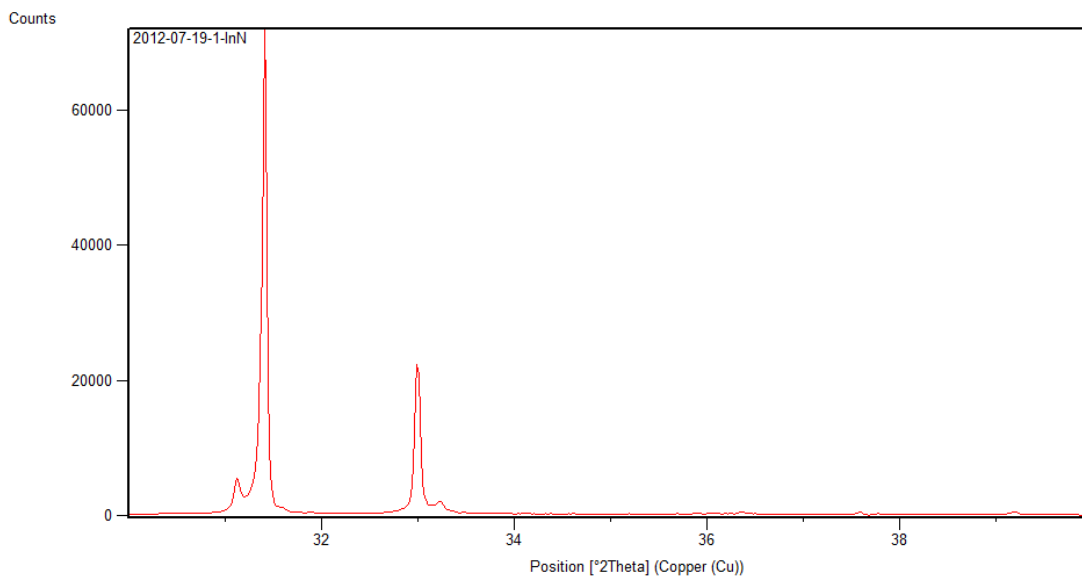
**Figure 40. XRD of 15s “Plasma Only” and 10s “Plasma + Setup”.**

This film shows a strong (002) indium nitride peak with slight indications of further peaks. Decreasing the “Plasma + Setup” step from to seconds yielded little change in the morphology of the film as evidenced through SEM and XRD. The film thickness as well the growth rate remained unchanged. Further decreasing the “Plasma + Setup” time from to seconds in major changes to the film.



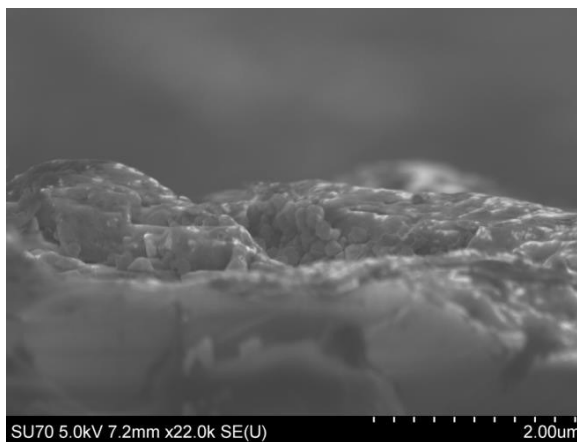
**Figure 41. SEM image of “Plasma + Setup” at 2 seconds.**

Figure 41 shows the SEM image of the resulting film. It is clear that large droplets have formed on the surface of the sapphire. These droplets ranged from under  $\mu\text{m}$  in diameter to well over  $\mu\text{m}$ . And XRD scan, shown in Figure 42 reveals additional peaks indicating a strong presence of tetragonal indium along with a strong indium nitride peak. This suggests that these droplets are not necessarily pure indium metal but rather the starting point of nanostructures composed of indium nitride along with indium droplets. Further investigation into this phenomenon is discussed in section 4.6.



**Figure 42. XRD scan of 2s “Plasma + Setup”.**

The “Plasma Only” time was then reduced from  $\mu\text{s}$  to  $\mu\text{s}$  while the “Plasma + Setup” time was increased to  $\mu\text{s}$  to mitigate the effects of non-laminar flow through the MO feed lines. The resulting film is shown in Figure 43.



**Figure 43. “Plasma Only” time reduced to 10 s with 5 s “Plasma + Setup”.**

The films structure is very non-uniform with a very rough surface. The XRD scan reveals similar peaks to the previous film. It is clear that nanostructures have begun to form.

#### **4.4.2.3. Results**

Relatively small changes in the “Plasma Only” time results in major changes to the films morphology and phases of the material within the film. Film crystallinity is greatly improved by the “Plasma Only” time employed in all of the indium nitride growths throughout this body of work. A starting point for future work with nanostructures has been identified.

#### **4.4.3. InN Grown Under Various TMI Times**

In this series the effects of additional metalorganic input times are evaluated on the growth of indium nitride. TMI input pulse time is adjusted while other parameters remain fixed. The effects are evaluated based on surface morphology, optical transmission, film thickness, and XRD peak characteristics. SEM images are also discussed.

#### **4.4.3.1. Experiment**

For this series of growths the metalorganic off time (plasma only time) is fixed at seconds while the TMI input time is varied between and in one second increments. Growth temperatures were controlled tightly with little variance averaging

. Bare sapphire substrates with no titanium backing were used. Growth times were adjusted by altering the outer loop count to keep total growth times comparable between samples. All growths featured 20 inner loops and a outer wait period was used. A low chamber pressure of along with of nitrogen flow through the plasma were employed. TMI flow was set to . The electrostatic grid was biased to . These growth conditions were inherited from previous indium nitride film growths showing good characteristics.

#### **4.4.3.2. Discussion**

Previous experiments produced an indium nitride film of relatively large thickness (503 nm) with good electrical characteristics and a reasonable growth rate. This was used as the basis for this set of experiments.

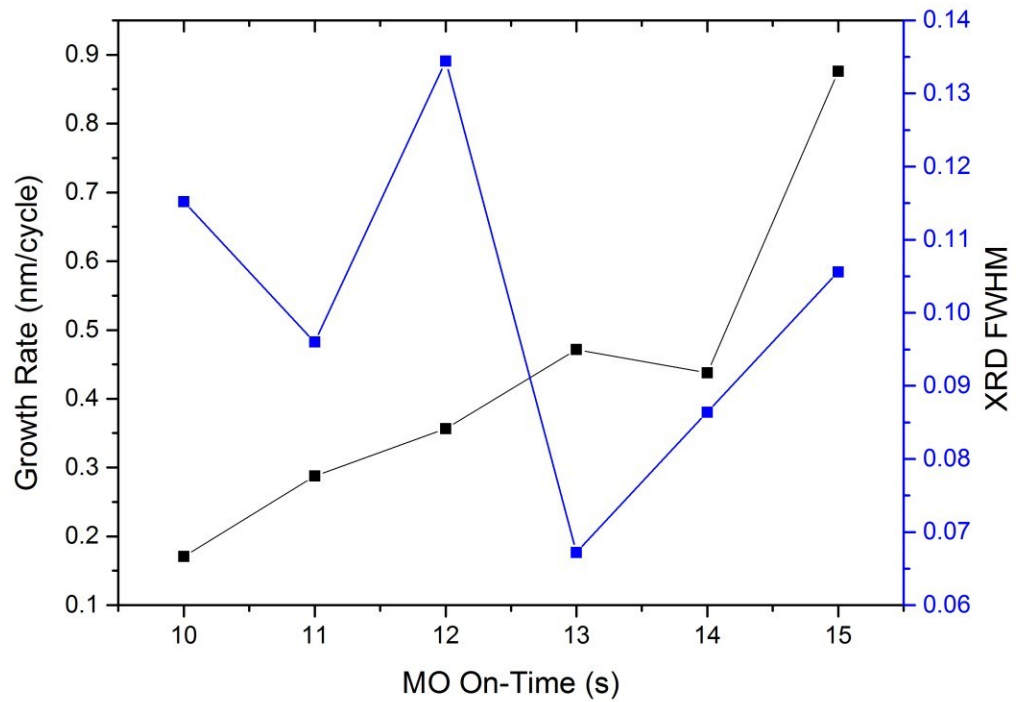


**Figure 44. Resulting growth rate and XRD FWHM for the various metalorganic injection pulse times.**

It is clear that the growth rate is severely impacted by small changes in MO on time. The thickness of the film varies accordingly. Growth rate also has a major impact on the XRD peaks. The minimum XRD FWHM occurred for the 13 s MO on time sample and is shown in Figure 45. This sample exhibits a strong (002) InN peak but a (101) InN peak is also clearly evident.

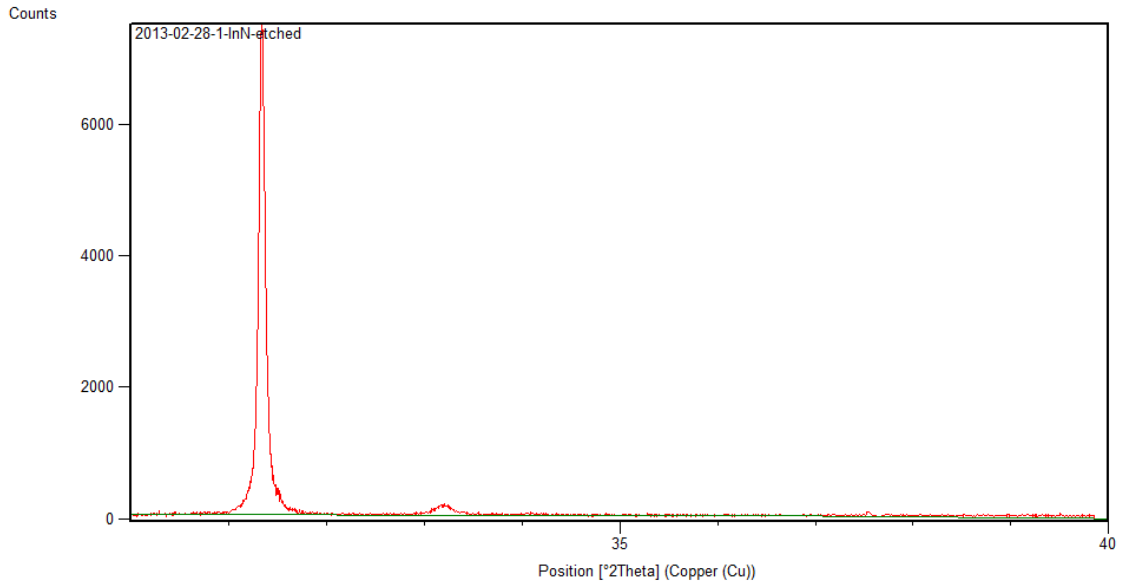


**Figure 45. XRD for sample grown with 13s MO on time.**

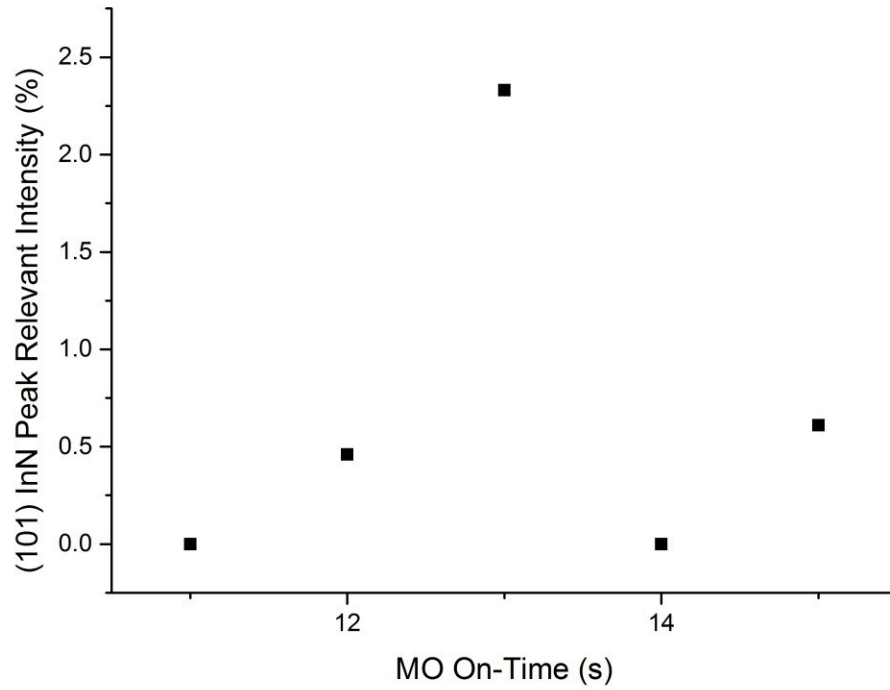


**Figure 46. (101) InN Relative Intensity.**

Figure 46 shows the relative intensity (to the (002) InN peak ) of the (101) InN peak. Though the minimum FWHM occurred for the 13s sample, the 14s sample has no detectable (101) InN peak. This suggests that epitaxial growth is maximized at this value, despite the higher FWHM value. This could likely be improved by use of a buffer layer. Looking at the SEM images, those with small MO on times feature more uniform films showing good coalescence at the surface resulting in a smooth surfaces with the exception of some droplets present. As growth rate increases with the 12s MO on time sample shown in Figure 47, the apparent crystal size also increases and less coalescence is observed towards the surface resulting in a rougher surface and a polycrystalline film.

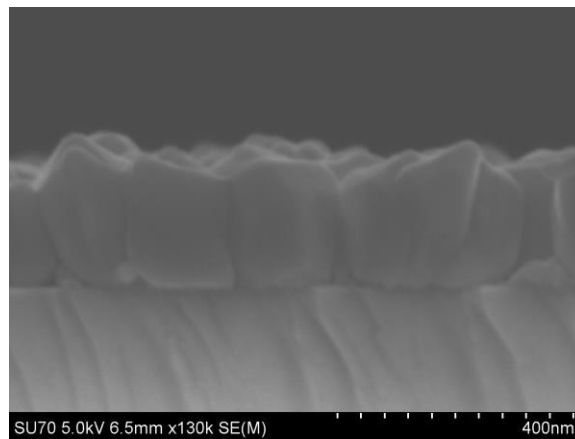


**Figure 47. SEM profile image for 12s MO on time sample.**

Further increasing the growth rate actually decreases the crystal size and promotes more coalescence of the surface but the sample is plagued with the presence of the additional (101) InN phase. At the maximum value of 15s an interesting phenomenon is observed. The crystal size is smaller towards the sapphire substrate but much larger near the surface as the crystals begin to coalesce. The resulting film is not as smooth as previous films, but has doubled in thickness despite having a slightly reduced total growth time.

#### **4.4.3.3. Results**

A range of TMI on times has been evaluated on the growth of relatively thick InN films. This time has a critical impact on the resulting film. Growth rate increases with increased TMI times. Crystal size and coalescence varies greatly with growth rate. Crystallinity is also greatly affected and films grown with high growth rates suffer in epitaxial quality.

## **4.5. Heterostructure Growth**

Heterostructure growth is similar in concept to single crystal growth. The adjacent layer acts as a template for growth. Extra care must be taken with samples exposed to the atmosphere as an oxide will quickly develop on the surface. Aged samples were etched prior to subsequent growth stages.

Prior to the development of the MEAgrow growth reactor growth of indium nitride and gallium nitride within the same system was not possible. This is due to the difference in growth temperature required for the two materials. Traditional MBE and MOCVD based systems could not provide suitable growth conditions compatible with both materials.

Obtaining suitable growth conditions for high quality films are restricted due to temperature limitations of indium nitride which limits growth temperature to the range [10] and is typically grown in MBE systems. High quality gallium nitride has typically required higher temperatures and is usually grown in MOCVD based systems.

The first publication [51] from the experiments detailed herein was based on results presented at the 2011 Material Research Society Fall Conference in Boston, MA.

A second publication followed [52] with results presented at the 10<sup>th</sup> Internal Conference on Nitride Semiconductors in Washington, DC.

### **4.5.1. Initial Heterostructure Growths**

Improving the fabrication of device quality heterostructures is crucial to the advancement of III-V semiconductors and forms a major component of this research project. Lower

temperature growth will allow for a greater amount of indium incorporation. The goal for the conductive indium nitride layer was a minimum of                    in thickness while the top GaN insulating layer goal was                    .

The analysis of four samples is described along with modifications to the process between each sample.

#### **4.5.1.1. Experiment**

Initial experiments used a bare sapphire substrate while later attempts used a commercial GaN buffer layer on silicon, and finally a lab grown GaN template was used. No substrates featured titanium backing. All growths were metal modulated.

#### **4.5.1.2. Discussion**

Our initial attempt to grow a conductive layer of InN on top of a smooth GaN buffer layer (                    RMS surface roughness) produced a thick InGaN alloy beneath the InN. XRD analysis is shown in Figure 48. As there is no evidence of the initial GaN layer, it was postulated that the deposition of a substantial indium metal pulse prior to complete nitridation of that layer converted the entire GaN buffer layer to InGaN through diffusion of the indium metal into the relatively thin (                    ) GaN buffer layer. This XRD data indicates that indium metal diffusion into the GaN is a severe problem for film growth under these conditions, even at the relatively low InN film growth temperatures of                    .

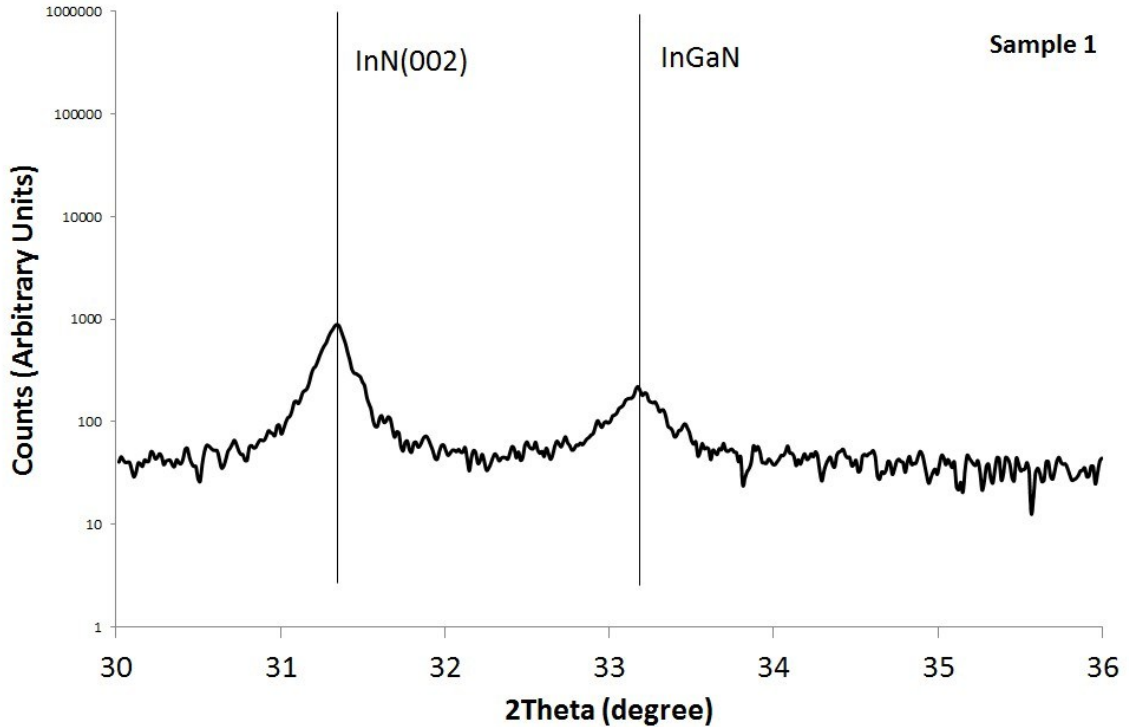


**Figure 48. XRD scan of first attempt showing InGaN alloy growth with no evidence of GaN buffer layer remaining.**

The surface roughness as high at . Hall Effect measurements indicate a mobility of —. However, since the thickness of the remaining GaN layer was negligible after growth (indicating that the integrity of the buffer layer had been severely compromised) it was decided to attempt a similar film growth using a third party commercially grown GaN on sapphire substrate. This substrate was used as a buffer layer to verify whether the integrity of the insulating GaN layer of sample 1 was at fault. This substrate had a 4 $\mu$ m thick GaN layer, much thicker than that used for sample 1. The resulting XRD graph for this sample 2 is shown in Figure 49. The results were similar save for a graded intermediary InGaN layer being formed. This graded layer appears as a plateau beginning at approximately with a high fraction of indium in the InGaN and continues

towards the GaN(0002) peak with an increasing fraction of gallium. The high GaN (0002) peak remained due to the much thicker initial layer of GaN.

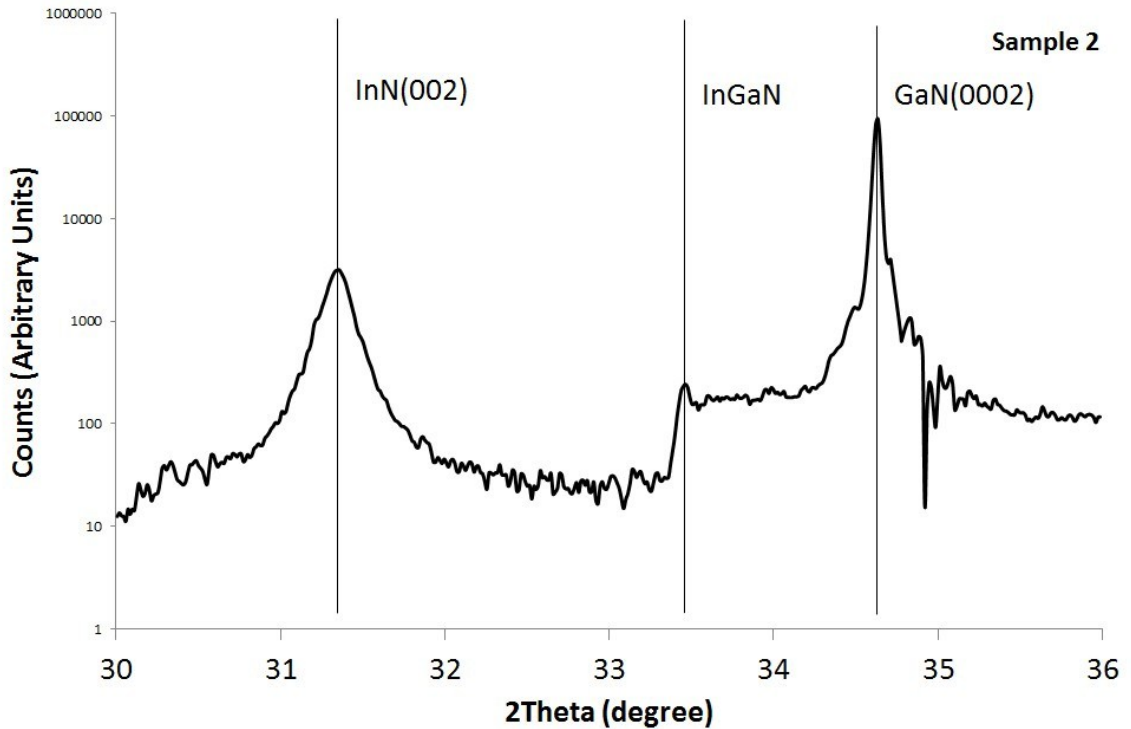


**Figure 49. Formation of InGaN on commercial GaN substrate.**

surface roughness by AFM for sample 2 was again high at . Hall Effect measurements indicated a mobility of —.

To promote a sharper interface between the GaN and InN layers, a reduction in the supply of indium during the initial metal deposition was employed in the program. Sample 3 produced the XRD graph results shown in Figure 50.

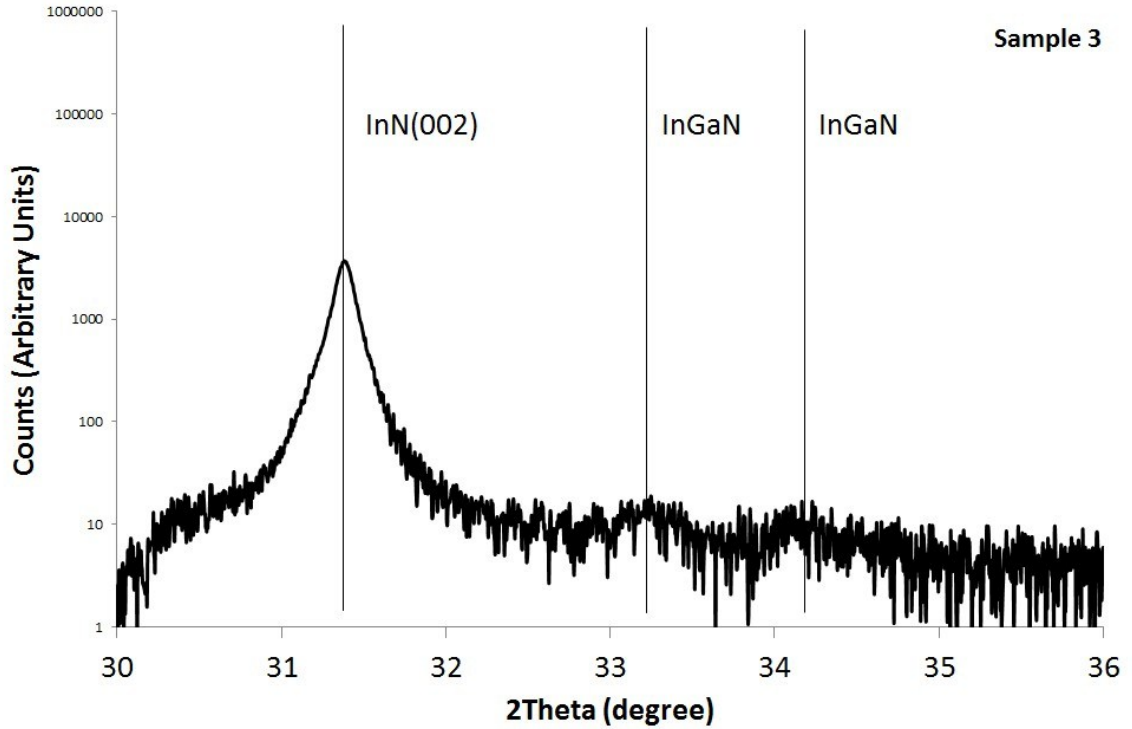


**Figure 50. XRD graph of sample 3 showing two InGaN peaks.**

AFM measurements indicated a higher surface roughness of . Mobility measurements did not improve remaining at —. The surface of the sample took on a mosaic appearance perhaps due to the nucleation of individual islands during growth due to incomplete nitridation. The resultant surface is shown in Figure 51.

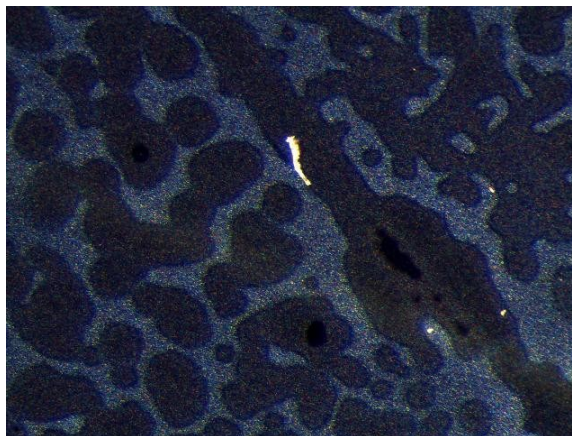


**Figure 51. Sample 3 surface image at 2x magnification.**

Despite this phenomenon the InN layer produced for sample 3 shows a marked improvement over samples 1 and 2. XRD results show two minor peaks for InGaN however a very strong peak for InN is now visible. For samples 1-3 the FWHM of the InN(002) peak remained essentially unchanged. The uniformity of all the samples 1-3 was relatively poor. We believe this was due to excess metal deposition at the edges of the substrate near the hotter metal surface of the substrate holder. We also noted that the plasma above the sample and substrate was not uniform. To improve the uniformity of the InN film surface for sample 4 an alumina mask was installed on the metal sample holder covering all but the substrate. This improved the uniformity of the plasma above the sample holder (as the sapphire and alumina had similar resistivity) and the plasma appeared closer to the sample. There also appeared to be no excess metal deposition at the edges of the sample. The resulting XRD spectrum for sample 4 is shown in Figure 52.

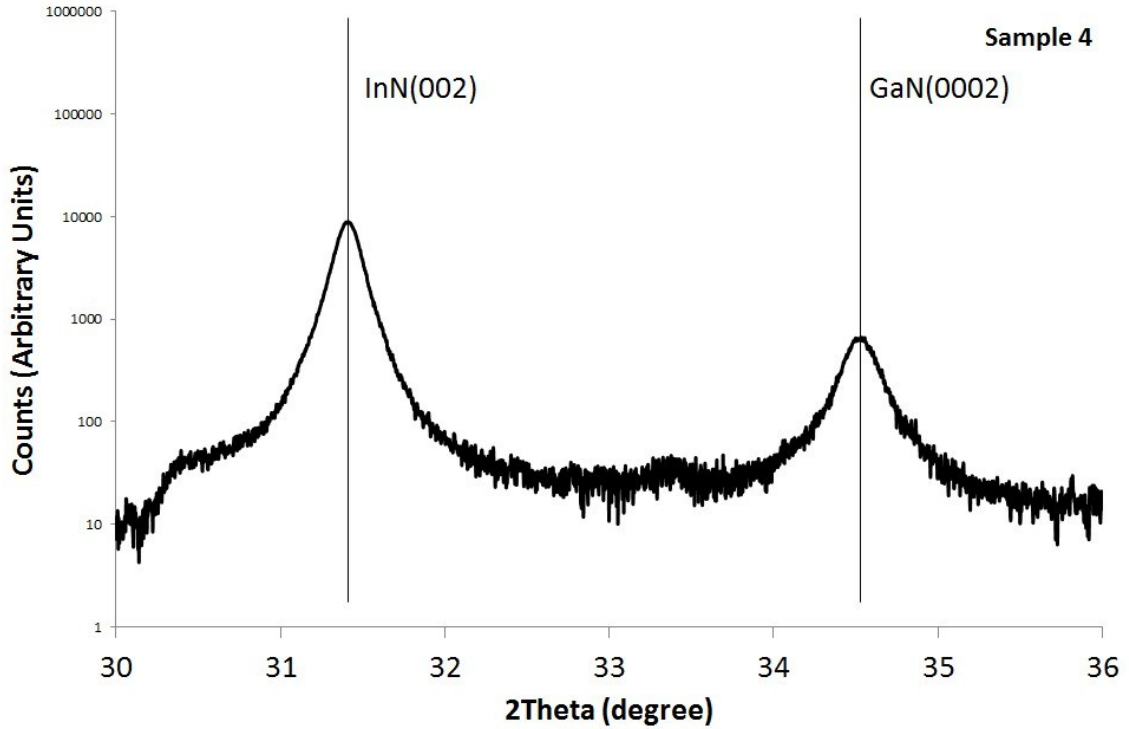


**Figure 52. XRD graph for Sample 4 showing strong peaks for InN and GaN indicating a sharp interface between layers with little InGaN present.**

From Figure 52 it can be seen that the interface between the GaN and InN was very abrupt with little InGaN being formed. The RMS surface roughness of the sample was lower at  $0.16 \mu\text{m}$  though this still indicates that further improvements in epitaxial quality can still be achieved. XRD results indicate a FWHM of  $0.16^\circ$  consistent with samples 1-3. Hall Effect measurements indicated an improved mobility of approximately  $100 \text{ cm}^2/\text{Vs}$ . The sample surface also appeared to be visually more uniform than for the previous samples.

#### **4.5.1.3. Results**

The results of these experiments have been published[51]. XRD results indicate that a sharp interface can be achieved between the semi-insulating GaN buffer layer and conductive InN films. The use of an alumina mask around the sample which shielded the metalorganic from the hotter surfaces of the substrate holder and provided a more uniform plasma distribution also provided marked improvement in our ability to grow a sharp interface between the indium nitride and gallium nitride. The electron mobility of the samples improved with this methodology. Growth of the InN appears to be c-axis oriented though epitaxial quality requires further improvement. Many of the improvements developed here were used in subsequent film growths.

#### **4.5.2. Further Heterostructure Growths**

To further increase the quality of the critical film interface samples have been grown without being removed from the system preventing the formation of indium oxide.

Sample growth was achieved using sapphire substrates. Some substrates featured a titanium backing provided by the University of Manitoba.

##### **4.5.2.1. Experiment**

Many more gallium nitride films were grown in order to evaluate suitable growth conditions for an optimum film. Substrates were heated to                    to reduce damage from the polishing process. After the substrate is loaded into the system, the chamber is heated to                    under a constant nitrogen gas flow for    hours. Each sample is then

subjected to one minute nitridation at \_\_\_\_\_ of nitrogen and a pressure of \_\_\_\_\_ with the RF plasma set low at \_\_\_\_\_. Actual growth temperature was varied between samples from as low as \_\_\_\_\_ to \_\_\_\_\_. Initial growth temperatures exceeded the critical threshold temperature for maintaining the structure of the underlying indium nitride films while later growth temperatures were reduced to prevent indium nitride desorption.

Metal modulated growth was employed. Gallium nitride layers were grown using a range of metalorganic to nitrogen plasma duty cycles ranging from \_\_\_\_\_ to \_\_\_\_\_ with the length of each cycle set to \_\_\_\_\_ seconds. Initial growths had the nitrogen plasma set at \_\_\_\_\_, while later growths featured \_\_\_\_\_. Two flow rates were used for the TMG source with initial growths at \_\_\_\_\_ and later growths increased to \_\_\_\_\_. The number of cycles used for each growth was based on the growth rate and the desired thickness of the resulting film set for \_\_\_\_\_. Growth times varied accordingly.

Indium nitride layers were grown under similar conditions to the gallium nitride but with some notable differences. For indium nitride growths an outer cycle wait period was added to help purge excess TMI. Growth temperatures ranged from \_\_\_\_\_ to \_\_\_\_\_. Some substrates again featured a titanium backing, as well as gallium nitride buffer layers. Cycle counts ranged from \_\_\_\_\_ to \_\_\_\_\_ with times per cycle ranging from \_\_\_\_\_ to \_\_\_\_\_ seconds. TMI duty cycles ranged from \_\_\_\_\_ to \_\_\_\_\_ with flow rates set at \_\_\_\_\_ and \_\_\_\_\_. Growths were attempted at pressures of \_\_\_\_\_ and \_\_\_\_\_, and nitrogen flows were tested from \_\_\_\_\_ to \_\_\_\_\_.

The desired heterostructure is shown in Figure 53. The gallium nitride layer is grown directly on the indium nitride layer.

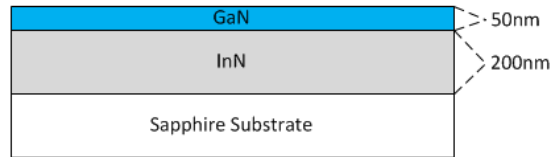


**Figure 53. The desired heterostructure.**

#### 4.5.2.2. Discussion

Initial attempts to produce a high quality, highly resistive layer of gallium nitride resulted in the film shown in Figure 54.

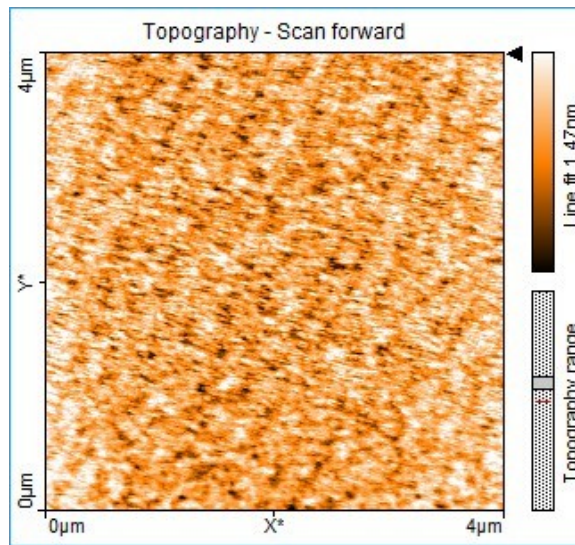


**Figure 54. AFM scan of the prototype GaN film to be used for the top layer of the heterostructure.**

This film achieved the required thickness of approximately , while maintaining an incredibly smooth surface roughness. Visible terracing is evident due to the

smooth surface and low thickness of the film, despite the strain caused by the lattice mismatch between the gallium nitride and the underlying sapphire substrate. However, the growth temperature was where desorption of indium nitride would be evident. To facilitate growth on an existing indium nitride layer the growth temperature was lowered to . The resulting film showed an increase in surface roughness to , with an expected decrease in growth rate.

Our initial InN layer grown at showed a surface roughness of , and an XRD FWHM of . The apparent band gap was calculated to be .

Improvements to the film were obtained by using a gallium nitride buffer layer prior to growth, increasing the growth temperature and adding an outer cycle wait period. This period allows for excess indium to desorb from the surface, improving smoothness and providing a more stoichiometric film. The resulting film in Figure 38 clearly shows 2-dimensional growth. The FWHM improved to .

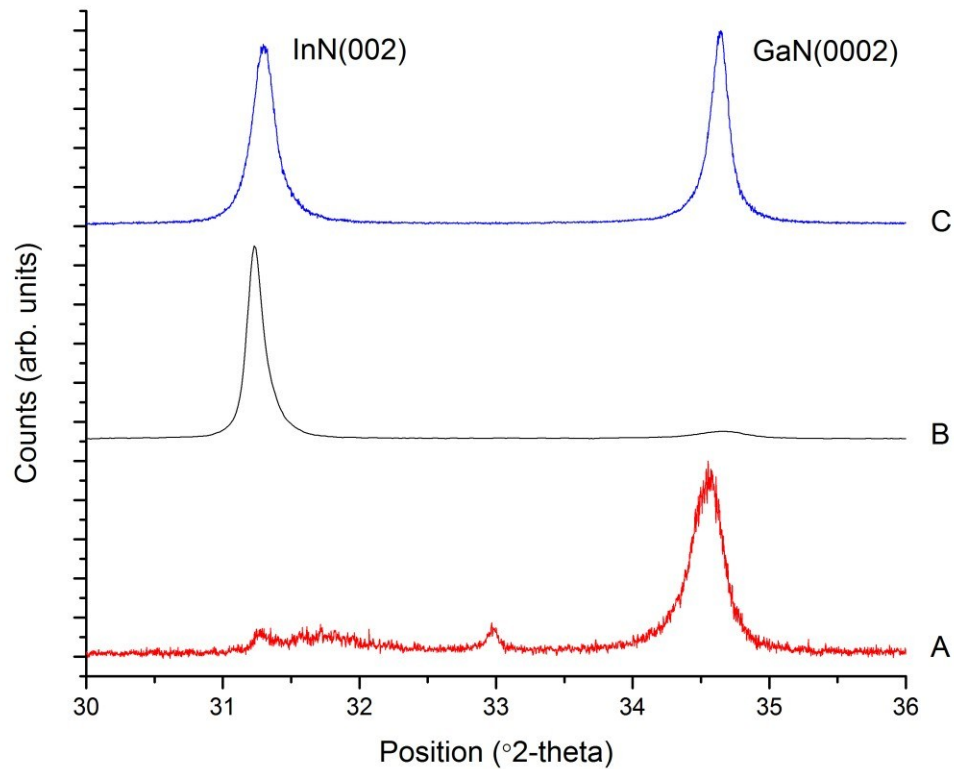


**Figure 55. XRD analysis of all the grown heterostructures.**

The first heterostructure grown, shown as plot A on Figure 55 resulted in the almost complete desorption of indium nitride from the film, during the higher temperature GaN deposition. A slight peak indicates that some indium nitride remains while a peak between the GaN(0002) peak and the expected In(002) peak indicates the presence of the ternary compound InGaN; evidence of some alloying of the materials. Growth temperature was . To reduce the desorption rate of nitrogen and prevent indium droplets from forming, the growth temperature was reduced to . The resulting film, shown as plot B on Figure 55, resulted in a surface roughness of with a strong indium nitride peak.

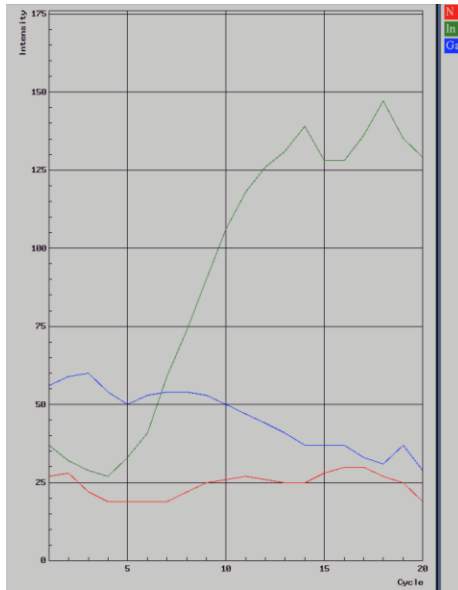


**Figure 56. Auger spectroscopy showing the presence of indium nitride at the surface of the sample.**

The GaN peak is evident but weak. Auger spectroscopy, shown in Figure 56, revealed the presence of indium nitride at the surface indicating a pinhole defect from the film surface down to the sapphire substrate. Growth temperature was further reduced to for film C in Figure 55. Both peaks are strong with a sharp interface between film layers. Surface roughness was .

#### **4.5.2.3. Results**

It has been demonstrated that the MEAgrow growth reactor is capable of producing structures containing both gallium nitride and indium nitride layers. High quality gallium nitride films have been epitaxially grown on indium nitride. The top layer gallium nitride films were grown at temperatures to prevent the desorption of indium in order to preserve the underlying indium nitride layer – a process not previously possible using MBE or MOCVD based systems. Though much future work remains for optimization of the films, a number of obstacles in these film growths have been overcome.

## 4.6. Nanostructure Growths

During the experiments detailed previously, a number of nanostructures were observed using the SEM. Nanostructures tended to form during indium nitride film growth but some gallium nitride nanostructures have also been observed. Nanostructures are a rapidly growing area of research due to their potential electronic and optical properties. This is particularly true for indium nitride and high indium content InGaN.

It is common to differentiate between nanostructures grown by a catalytic method in which a 3<sup>rd</sup> party catalyst is employed to assist in growth, and those deemed self-catalytic which require no additional material. Self-catalytic growth has the advantage of less impurities in the film. All growths herein are self-catalytic and are grown under metal rich conditions.

The results have been published[5].

The longer adatom diffusion time which is characteristic to the MEAgrow growth technique allows for nanowire formation at lower temperatures. The use of plasma for an activated nitrogen species promotes a higher diffusion rate of the nitrogen into the droplet allowing the atom to reach the In/InN growth interface, where the nanowire is formed.

### 4.6.1. Experiment

Substrates are heated to                    prior to film growth to eliminate polishing damage.

Prior to growth the substrate is heated for    hour under a nitrogen flow at           before being nitrided for    minute under a nitrogen flow of                    with a           RF power

to the plasma head, and chamber pressure of . During growth the temperature is fixed at . Growth is metal modulated with the plasma remaining on at a flow of and . MO on time was with a flow of of TMI. Total cycle time was with the number of cycles set to . Pressure was maintained at .

#### 4.6.2. Discussion

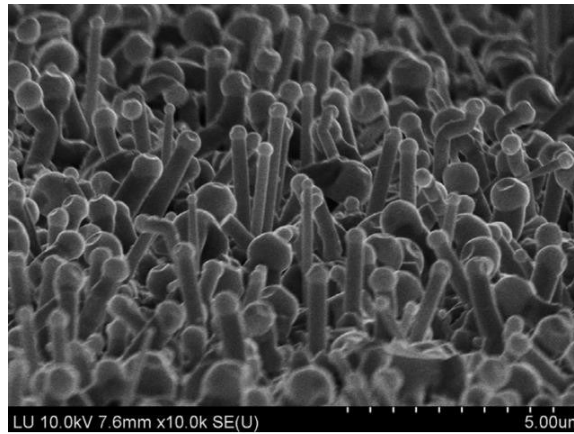


**Figure 57. SEM showing nanowires[5].**

Figure 57 shows the resulting nanowires grown under the conditions described above.

These nanopillars are about in length and to in diameter. It is evident that coalescence occurs where they tops touch during growth.

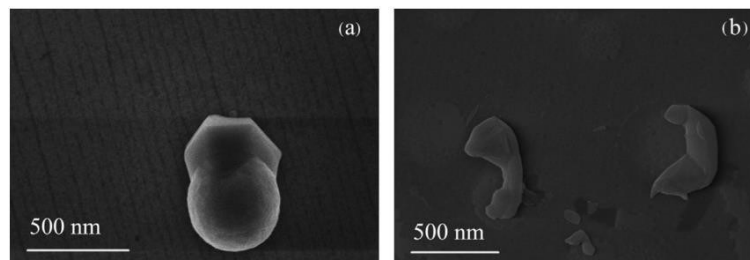


**Figure 58. SEM for 425 cycle samples. (a) film as grown (b) after film has been etched.[5]**

Lowering the cycle count to      cycles and lowering the RF plasma power to produced the sample shown in Figure 58. It is evident that the base is hexagonal and the shaft is cylindrical. Etching the film removes the metal, leaving only the showing, indicating that the top is indeed a metal droplet. The diameter of the nanopillar is determined by the diameter of droplet.

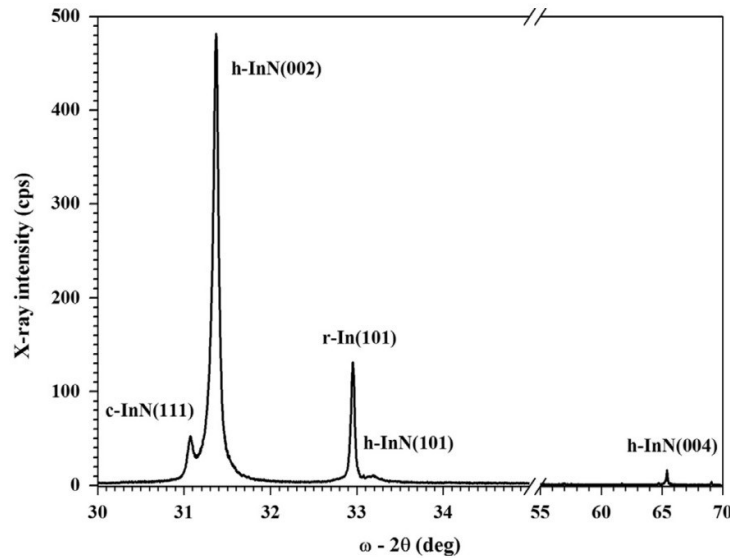


**Figure 59. XRD for nanopillar sample[5].**

XRD for a nanopillar sample is shown in Figure 59. It is evident that hexagonal InN as well as cubic InN are present along with rhombohedral indium. The sharp peaks indicate that the nanopillars are of good crystallinity and stress free.

#### 4.6.3. Results

Self-catalytic indium nitride nanopillars have been produced using the MEAgrow growth technique on bare sapphire substrates. Metal rich conditions are required for nanopillar growth.

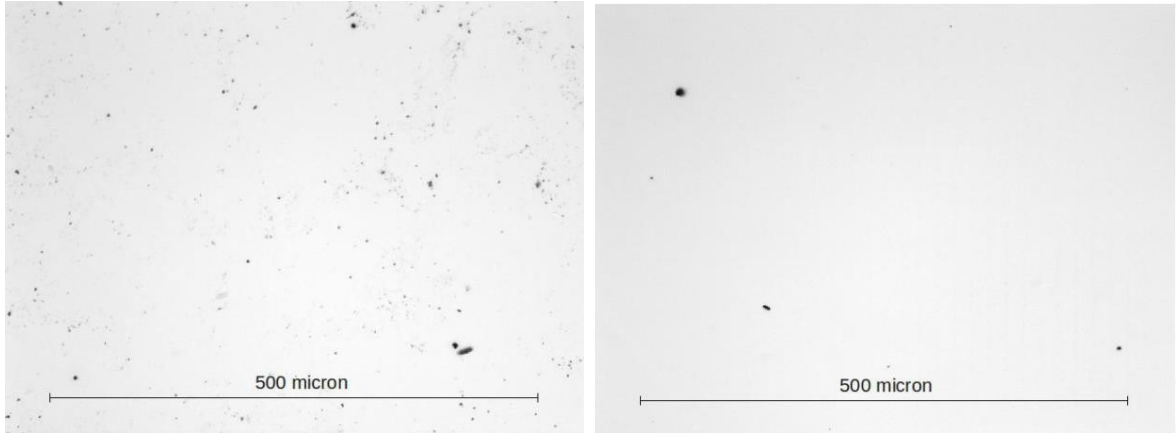
## **Chapter 5**

### **Contact Deposition**

In this section the collaboration which began in 2012 between the University of Manitoba and the Lakehead University Semiconductor Research Lab is detailed. Samples generated by the MEAglow reactor were sent to the University of Manitoba for further analysis and characterisation. Specifically our interest was in heterostructures and the composition and integrity of the films. A critical step in development of the FET described in Chapter 1 is the application of contacts to the films.

The heterostructure is shown in Figure 53. To evaluate the characteristics of the top GaN film, the samples is first examined under a microscope. Following that titanium/aluminum/gold contacts are deposited and the electrical performance is measured. A four point probe station is then used with no contacts and the results are compared to literature values. Finally nickel contacts are deposited and the IV characteristics are evaluated for ohmic behavior.

The initial heterostructures sent to the University of Manitoba were suspected to have indium contamination within the top GaN layer. The surface of the first two samples were examined under a high power microscope, shown in Figure 60.

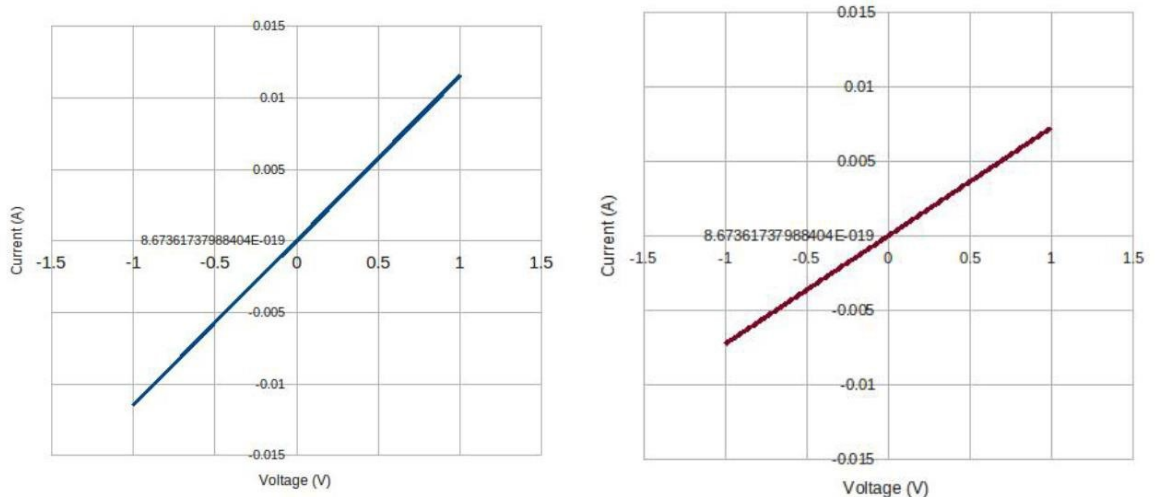


(a)

(b)

**Figure 60. Pinhole defects on the heterostructures[53]. (a) initial sample (b) improved sample**

Figure 60 (a) shows the first structure with clear evidence of pinhole defects leading down to the underlying GaN film and possibly the sapphire substrate. Improvements to the heterostructure lead to the film shown in Figure 60 (b). These improvements have been detailed in Section 4.5.2. Despite the marked improvement, pin holes are still present in the film.



(a)

(b)

**Figure 61. IV characteristics for both samples.**

Contacts were then sputtered onto the samples using an MRC-8667 with the method described in [53]. A two-point contact probing station was used to take IV measurements across the contacts. The results revealed ohmic behaviour for both samples, as shown in Figure 61. The improved film had a slope of  $1.5 \times 10^{-4} \text{ A/V}$  – equating to a resistance of  $6.67 \times 10^3 \Omega$ .

Though the second film showed an improvement, both films showed ohmic behaviour which implies contamination in the GaN film, most likely from indium, causing the film to be unintentionally doped. However, it was postulated that the method of contact deposition could be causing diffusion in the film.

For validation a four-point probe station was employed to test the resistivity of the GaN layer. Results indicated a resistivity of  $1.5 \times 10^{-4} \Omega \cdot \text{cm}$ , much lower than the value taken from literature to be  $1.5 \times 10^{-2} \Omega \cdot \text{cm}$ . This suggests that the probe tip was likely penetrating through the top GaN layer into the conductive InN layer.

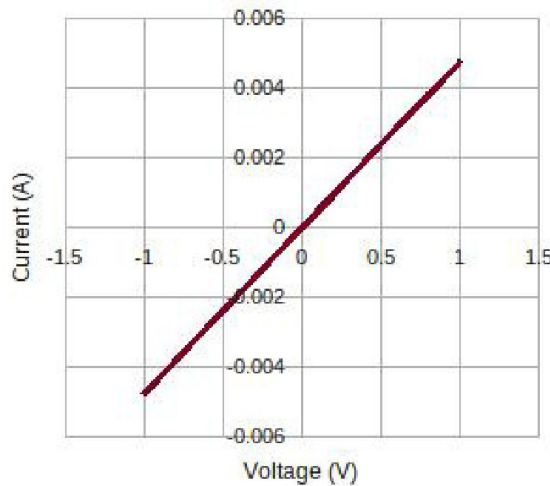


**Figure 62. IV characteristics for the nickel contacts.**

Further valuation was provided by depositing two                    thick nickel contacts onto the sample. The workfunction of nickel (                    ) is much higher than GaN (                    ). This means contacts deposited should exhibit a Schottky like IV characteristic. The resulting IV characteristic is shown in Figure 62. It is clear that the contacts were in fact ohmic in behaviour.

Contacts have been successfully deposited onto the films. All of testing done reveals that further work needs to be done in order to obtain a heterostructure containing an intrinsic undoped GaN top layer with a conductive InN layer underneath with no contamination within the top GaN layer. Future work should test a thick top GaN layer which may be tested with the four-point probe station without breaking through the top film. Films should be further optimized through growth parameter changes to eliminate as much as possible the pinhole defects.

## **Chapter 6**

### **Film Analysis and Characterisation**

The formation of high quality films in terms of physical, structural, and electrical properties would be impossible without the use of high quality instrumentation equipment. In this section a description of each instrument is given along with basic theory, method of operation, and an explanation of potential inaccuracies in the measurements. Non-destructive analysis is first performed, followed by any required destructive analysis.

In general the first step towards analysis of a grown film is to gather the topography of the surface using the AFM available in CB1040. There is an exception if it is known beforehand that the sample likely contains nanostructures which are too rough to measure using the AFM. If the film is single crystal or polycrystalline AFM measurement should be possible. Having acquired a successful AFM image, the next step is analyse the result using the UV-Vis-NIR spectrophotometer. This is only possible in the case that the sample has no titanium backing, which would block the transmitted light giving no result. XRD is then performed on the sample to obtain information regarding the samples crystallinity and chemical makeup followed by analysis by SEM. Conductive films, generally those with an indium nitride top layer, are measured by Hall Effect.

## 6.1. Atomic Force Microscopy (AFM)

AFM provides an accurate method for examination of the films surface. AFM has an advantage of other types of microscopes as it allows for quantitative data on the vertical structure of the surface to be captured. It is a mechanical method and does not rely on electromagnetic radiation. A sharp probe tip is moved along very close to the surface and interacts with surface features as it moves. Motion of the probe is captured and translated into an image. Multiple modes of operation are available. The operating mode determines what signals are being transmitted to the controller. Non-contact mode is the most basic. The tip has little wear as it does not contact the surface. High resolution images are obtained. In dynamic mode a fixed amplitude is applied to the tip while the excitation frequency is varied. The measured response represents the resonance of the cantilever vibration. The reference amplitude is taken to be that of the cantilever tip while it is not close to the sample surface. Finally in phase contrast mode the phase response of the cantilever is compared to the input signal. This provides additional information about the surface and slightly below the surface of the film. In practice the dynamic mode and phase contrast mode were used throughout this work. Surface roughness was the main quantitative data collected from the AFM, while the images themselves provide some insight into the presence of droplets and morphology of the film (such as crystal size). Effort was taken to standardize measurements for comparison. Most images were taken using a second per line scan time allowing for increased resolution.

## 6.2. Hall Effect

The Hall effect was discovered in 1879 by Edwin Herbert Hall [9]. It is a relatively simple technique for measuring a number of important electrical properties of a film. The method relies on the basic physical principal that a voltage develops when a current is passed through a conductive material under the presence of a magnetic field. This phenomenon can be exploited to gather many electrical properties of a material. For this work an Ecopia HMS-3000 was used at room temperature.

Conductive samples must be used. Once the sample is mounted in the system, an IV test is performed to determine suitable test conditions and verify the integrity of the four contacts. The Hall effect test can then be performed. The mobility is easily calculated from the obtained sheet carrier density and the sheet resistance

$$\mu = \frac{1}{q} \frac{R_s}{n_s} \quad (3)$$

Where  $q$  is the charge,  $n_s$  is the sheet carrier density,  $R_s$  is the sheet resistance and the resulting units are in  $\text{cm}^2/\text{Vs}$ . An example result is shown in Figure 63.

Note that the film thickness must be known and can be obtained from UV-Vis or more accurate by SEM. Hall effect is a very powerful tool providing key details about the films electrical characteristics.

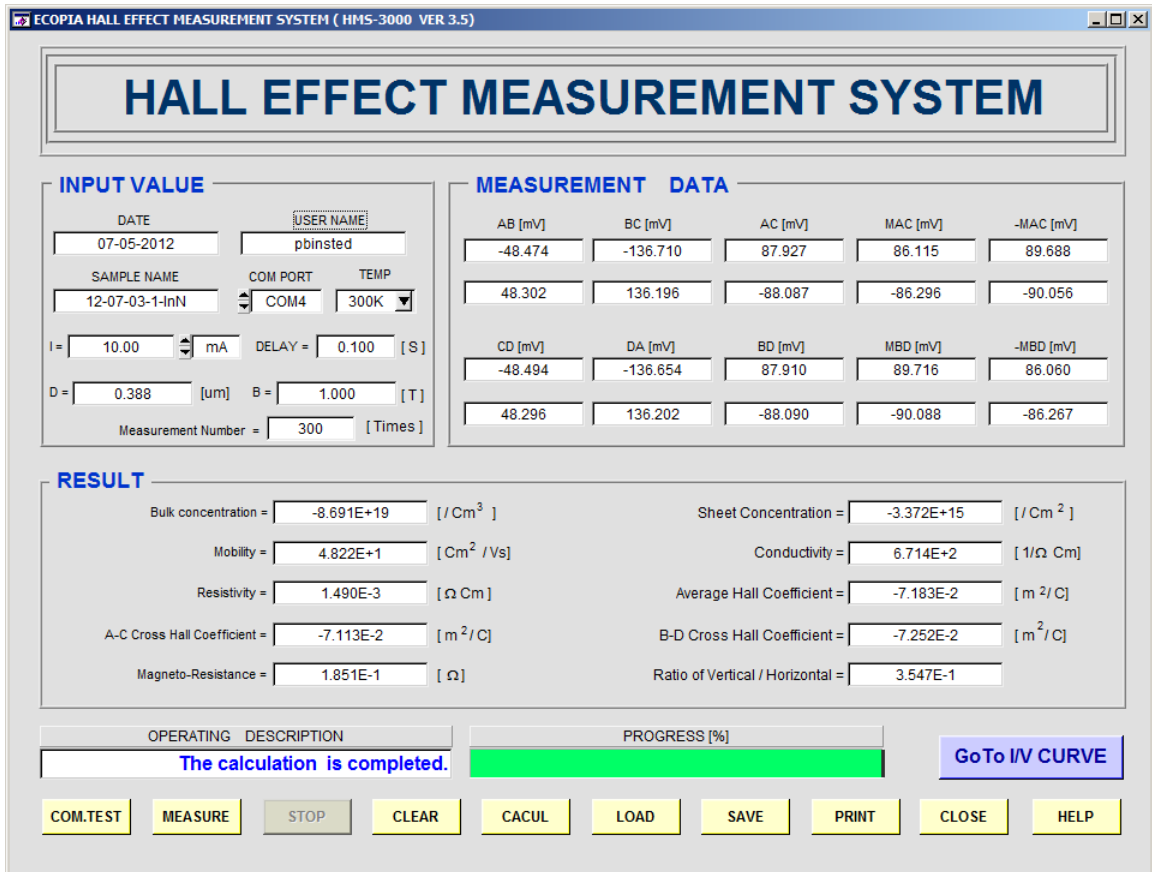


Figure 63. Sample Hall effect screen.

### 6.3. Scanning Electron Microscopy (SEM)

The Lakehead University Instrumentation Lab recently acquired a Hitachi SU-70 SEM unit. This powerful machine allows for collection of a number of important film characteristics. Profile and surface images are acquired. Profile images allow for the film thickness to be directly and accurately observed. The crystal morphology and a general impression of the surface roughness are also acquired. The surface imaging allows for the detection of defects such as pinholes, and gives an impression of whether the film experienced 2D or 3D growth.

Samples are scored and snapped for mounting on the sample holder. A carbon based conductive paint allows for conductivity between the film surface and the holder which is required to obtain suitable quality images. Conductive samples such as indium nitride are more easily scanned than insulating samples. For this work one piece of sample was mounted flat on the holder, while another was mounted sideways allowing for profile imaging. Effort was taken throughout to obtain sample pieces near the centre of the substrate such that edge effects due to heat during growth would be avoided.

#### **6.4. Spectroscopy (UV-Vis)**

One of the most important tools in the evaluation of semiconductor material parameters is the UV-Vis-NIR spectrophotometer. This instrument allows us to extract optical data from the sample throughout the ultraviolet – visible – near infrared spectrum. Our primary instrument for this work was the Varian Cary 5e which can measure a range from 190 to 3200 nm.

The procedure is simple. A bare sapphire substrate is used to perform a baseline calibration followed by any samples required to be measured.

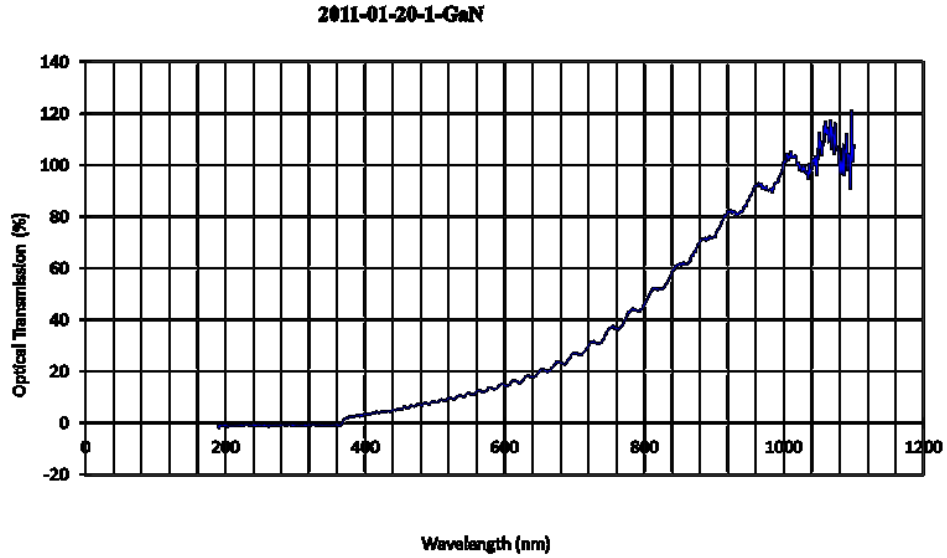


**Figure 64. Typical optical transmission data.**

An example is shown in Figure 64. In order to evaluate the band gap of the material we need to look at the optical density squared, and for each wavelength we calculate [54] the optical density squared

$$T = \frac{I}{I_0} \quad (4)$$

And convert the wavelength into Energy:

$$(5)$$

We then plot the resulting curve and observe the tangents as indicated.

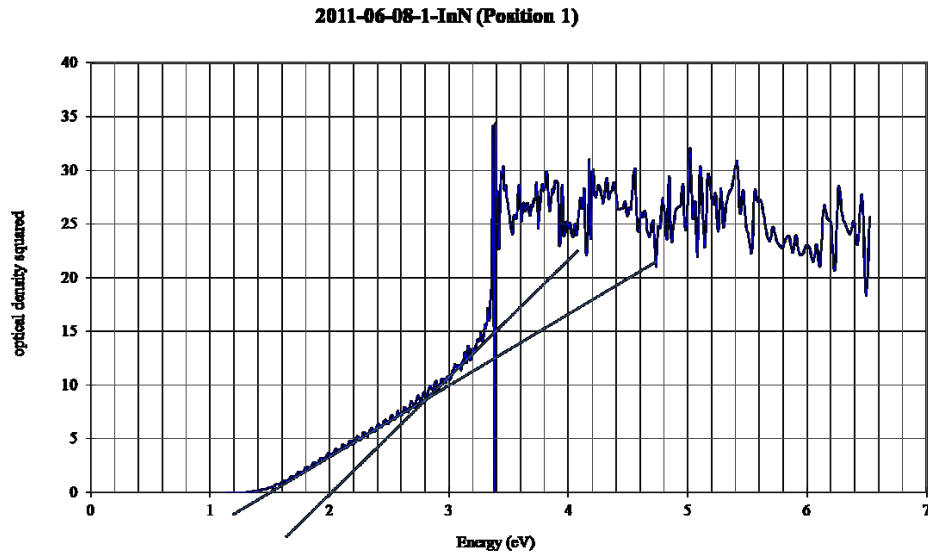


**Figure 65. Typical optical density squared plot.**

The data shown in Figure 65 shows an estimated band gap of about 1.6 eV for the top layer of indium nitride, but it is interesting to note that the band gap of the underlying buffer layer of gallium nitride is visible at about 3.4 eV.

## 6.5. X-Ray Diffraction (XRD)

XRD analysis allows us to understand the crystal arrangement of our materials. It is an extremely powerful technique in that with little effort it provides many useful results. It is a non-destructive technique which relies on the constructive and destructive nature of waves. Scans are performed to obtain counts or counts per second versus angle charts. These graphs provide full width half maximums (FWHM) which are used for judging the quality of the crystalline structure. Narrow FWHMs indicate the film is high quality and epitaxial, whereas broad FWHMs indicate that the film is perhaps strained or polycrystalline. FWHM are easily obtained through analysis of a  $2\theta$  scan.

The Lakehead University Instrumental Lab (LUIL) features an X'Pert PRO MPD. This is a state of the art, fully featured system.

The basic scan is performed by applying an incident x-ray to the surface of the film and measuring the reflected x-ray intensity. The measured angle is fixed at twice the incident angle, while the incident angle is programmed to sweep through a predetermined range. Various parameters are configurable to obtain a scan of maximum resolution and accuracy.

The foundation of XRD analysis relies on Bragg's law

(6)

where  $n$  is an integer,  $\lambda$  is incident wavelength,  $d$  is spacing between planes of the atomic lattice, and  $\theta$  is the angle between the incident wave and the scattering planes.

Applying Bragg's law along with Bragg's conditions (derived from vector form) provides us with the following

$$\sqrt{h^2 + k^2 + l^2} \frac{a}{n} = d \quad (7)$$

where  $a$  is the lattice parameter,  $n$  is as per above, and  $h$ ,  $k$ , and  $l$  are the plane indices.

The flat sample stage used for analysis has the advantage that it requires no alignment prior to use. However, since no alignment is available there is always an error introduced due to the height mismatch between the instruments sample plane and the actual sample.

The error introduced is translated into a horizontal shift of the results which varies with the angle. Luckily it is fairly straightforward to correct this error in software.

Our substrates are typically about \_\_\_\_\_ thick and this thickness is provided by the substrate supplier. The displacement correction is given by:

$$\text{_____} \quad (8)$$

Where \_\_\_\_\_ is the displacement from the focusing circle (equal to approximately the substrate thickness) in \_\_\_\_\_, \_\_\_\_\_ is the goniometer radius (equal to \_\_\_\_\_ for our instrument), \_\_\_\_\_ is the incident angle in radians. The X'Pert HighScore Plus software supplied with the instrument can easily implement this, and all that is required is the substrate thickness.

XRD measurement produces a k-alpha emission which distorts results. It is due to an electron transitioning to the innermost k shell and is a fundamental property of the material used for x-ray generation. However it can be easily removed with software.

All results shown in this dissertation have been corrected for k-alpha removal and sample mounting displacement.

# **Chapter 7**

## **Theoretical Treatment of the Results**

### **7.1. Calculation of the Electron Band Structure of Compound**

#### **Semiconductor Alloys**

Semiconductor compound alloys based on the binary compounds InN, GaN, and AlN are very important in semiconductor physics and in the design of next generation semiconductor devices. As such these three binary alloys have been the subject of much investigation [55]–[60] during the last ten years. This section contains theoretical investigations in the calculation of the electronic band structures of InN, and GaN[55], [56], [61]–[64] in comparison to the results obtained experimentally during the course of this research project.

The relatively recent observation of photoluminescence for InN and the absorption features near this energy have been the subject of a number of publications [10], [65], [66]. It has been proposed that the low energy features indicate a band-gap. However, InN has long been recorded as having a much higher band-gap of . The large difference between these values is not presently completely understood. The Moss-Burstein effect does not explain the variation observed for material of low carrier concentration, and Vegard's law indicates that oxygen levels in the higher band-gap material are insufficient to account for the difference[10]. Sample inhomogeneity offers a

strong possible explanation. Existing growth methods are known to produce non-stoichiometric indium nitride. This section investigates the possibility that these low energy features arise as growth artifacts due to an alloy formed by non-stoichiometric InN containing both single In substitutions on N sites and single N substitutions on In sites.

**7.1.1. Electron Band Structure of a Generic Crystal  $A_xB_{1-x}C$  where (A and B are cationic atoms, and C is anionic atom)[67]**

For analysis purposes is considered to be a periodic crystal with a large primitive super-cell. The primitive super-cell contains a finite number of elementary cells. Each elementary cell has symmetry equal to the primitive cell of crystals comprised of AC and BC if the positions of the cations and anions have no consideration for the nature of the atoms. For binary crystals the elementary cell would therefore be equal to the primitive cell. Consider the number of orbitals in the elementary cell to be equal to . For simplicity the number of elementary cells in the primitive super-cell in each direction of the crystal axis to be odd number i.e. . Only interactions between the orbitals belonging to the primitive super-cell of the multinary crystal are considered. Using the one-electron approximation we express the electron wave function of the crystal as a linear combination of atomic orbitals (LCAO) such that

$$\sum \sum \sum \tag{9}$$

Where by definition  $\mathbf{r}$  and  $\mathbf{R}$ , integers  $n_x$  and  $n_y$  run over  $-\infty$  to  $\infty$ ,  $\mathbf{r}$  is the radius vector of the electron,  $\sum_{\mathbf{R}}$  is the sum over all primitive super-cells of the crystal,  $\sum_{\mathbf{r}}$  is the sum over all orbitals belonging to the elementary cell,  $\sum_{\mathbf{r}'}^{\mathbf{r}}$  is the shorthand notation for  $\sum_{\mathbf{r}'} \sum_{\mathbf{R}'} \sum_{\mathbf{r}''}$ ,  $\phi_{\mathbf{r}}(\mathbf{r})$  is the atomic orbital (corresponding to an atom having positional vector  $\mathbf{r}$ ) in the elementary cell characterized by vector  $\mathbf{R}$ , where  $\mathbf{a}_1$ ,  $\mathbf{a}_2$  and  $\mathbf{a}_3$  are three basis vectors of the primitive super-cell defined by the elementary cell.

This means that only the interactions between orbitals belonging to the primitive super-cell will be considered and electron orbital  $\phi_{\mathbf{r}}(\mathbf{r})$  belonging to the primitive super-cell will be used. For a one electron approximation applied to the primitive super-cell the orbital  $\psi_{\mathbf{r}}(\mathbf{r})$  becomes

$$\psi_{\mathbf{r}}(\mathbf{r}) = \sum_{\mathbf{R}} \sum_{\mathbf{r}'} \phi_{\mathbf{r}'}(\mathbf{r} - \mathbf{R}) \quad (10)$$

The expectation value of the electron energy is

$$\langle \psi_{\mathbf{r}} | \hat{H} | \psi_{\mathbf{r}} \rangle \quad (11)$$

Where  $\hat{H}$  is Hamiltonian. The Ritz variation procedure over (11) can be performed for the coefficients in (10) and the result is the matrix equation for the primitive super-cell

(12)

The hyper-matrix of dimension  $N$  has sub-matrices of dimension  $n$  and the overlap hyper-matrix has sub-matrices  $S_{ij}$ . In conformity with the translational symmetry of the primitive super-cell and the Born–von Karman boundary conditions, matrices  $\mathbf{H}$  and  $\mathbf{S}$  are cyclic hyper-matrices for which a unitary transformation always exists which makes these hyper-matrices become diagonal hyper-matrices. The transformations of both matrices  $\mathbf{H}$  and  $\mathbf{S}$  are similar and only these connected with  $\mathbf{H}$  will be given. The unitary matrix  $\mathbf{U}$  of dimension  $N$  having  $n$  blocks defined as

$$U_{ij} = \frac{1}{\sqrt{n}} \exp\left(\frac{2\pi i j i}{N}\right) \quad (13)$$

will transform  $\mathbf{H}$  and  $\mathbf{S}$  in block-diagonal forms ( $\mathbf{I}$  is a unit matrix having dimension  $n$ ):

$$(14)$$

The definition in (13) proves that  $\mathbf{U}^{-1} \mathbf{H} \mathbf{U} = \mathbf{H}'$ , where the unit matrix  $\mathbf{I}$  has dimensions  $n$

. The diagonal block of the block-diagonal matrix (14) has the form

$$\sum_{i=1}^n \epsilon_i \mathbf{I}_i \quad (15)$$

where matrix  $\mathbf{H}'$  is a sub-matrix of the matrix  $\mathbf{H}$  before the unitary transformation.

This sub-matrix corresponds to the elementary cell having radius-vector  $\mathbf{r}$ . The equation (12) can be multiplied on the left by  $\mathbf{U}^{-1}$  and the unit matrix can be inserted in both sides of the same equation

$$(16)$$

Matrix  $\mathbf{H}'$  can be defined as  $\mathbf{H}' = \mathbf{U}^{-1} \mathbf{H} \mathbf{U}$ . The equation (16) can be expressed by  $\mathbf{H}' \mathbf{c} = E \mathbf{c}$  and by equation (14) in the following way

$$(17)$$

However matrices  $\mathbf{H}'$  and  $\mathbf{S}'$  are block-diagonal and equation (17) can be decomposed to simpler equations

$$(18)$$

Where  $\mathbf{H}'(\mathbf{p})$  is given by (15). Since the primitive super-cell is very large the number of elementary cells, numbered  $N$ , is also large. This leads the electron wave vector to be defined as

$$(19)$$

where  $\mathbf{a}_1, \mathbf{a}_2, \mathbf{a}_3$  are the basis vectors of the reciprocal elementary lattice and

$$\text{-----} \tag{20}$$

where ( ). Equation (18) can be re-written as

$$\tag{21}$$

Where

$$\Sigma \tag{22}$$

The electron band structure of the multinary crystal can be found from (21) as Eigen-values of the matrix  $\mathbf{H}(\mathbf{k})$ . According to (22) every energy Eigen-value of  $\mathbf{H}(\mathbf{k})$  contains the corresponding Eigen-values of the matrices  $\mathbf{H}(\mathbf{q})$  and the electron energy is

$$\Sigma \tag{23}$$

Expression (23) shows that the electron energy in the multinary crystal  $E(\mathbf{k})$  can be defined as a set of energies  $E(\mathbf{q})$ . Each element  $E(\mathbf{q})$  of this set is electron energy in the elementary cell having a radius-vector .

Performing a Fourier transform to both sides of (23) reveals the dependence of the electron energy on the coordinates expressed by

$$\sum - \quad (24)$$

Where  $\delta(\mathbf{r})$  is a delta function. (24) shows that the electron energy depends on the electron radius-vector and the elementary cell where the elementary cells are equivalent.

We can determine the electron band structure of a multinary crystal through interactions within the primitive super-cell, which allows for determination of the corresponding sub-bands. We now introduce a quasi-elementary cell with the same structure as the elementary cell but constructed from atoms of In, Ga, and N. Expressions (23) and (24) show the resulting electron band structure to be the sum of electron band structures calculated for each elementary cell. These expressions can be applied to the quasi-elementary cell. Orbital interactions within the quasi-elementary cell provide approximately  $\frac{1}{N}$  of the contributions in electron energy. These contributions further increase if the interactions between second neighbouring orbitals are taken into consideration. Ignoring localization of interactions, the multinary crystal electron band structure determined using this method contains the same sub-bands as the primitive super-cell. However, the sub-bands are localized to the corresponding quasi-elementary cell so the electron band structure of the crystal depends on  $\mathbf{k}$  and  $\mathbf{r}$ . This conforms with (23) and (24) with the approximation of the quasi-elementary cell. Electron band structure is determined using this method for a continuous sequence of electron band sub-structures. Calculations are done for each of the corresponding quasi-elementary cells.

### 7.1.2. Electron Band Structure of a GaN Crystal with Defects

A film with defects may be modelled as an alloy expressed as  $\text{Ga}_{1-x}\text{N}_x$  where the material properties depend on the content of  $x$ .  $\text{N}$  is an atom different from both  $\text{Ga}$  and  $\text{N}$  which substitutes on the  $\text{N}$  sites. For this case we only consider alloyed species with substituting on the nitrogen site and not segregated species in the wurtzite crystal. For this arrangement a new ternary semiconductor expressed as  $\text{Ga}_{1-x}\text{N}_x$  with  $x$  is used which has two binary constituents at the extremes of  $x = 0$  and  $x = 1$ . This condition allows the introduction of a primitive cell of binary constituent  $\text{Ga}_{1-x}\text{N}_x$  satisfying the following conditions:

- a)  $\text{N}$  atom substitutes for a  $\text{N}$  atom retaining the tetrahedral symmetry of the crystal cell;
- b)  $x$  of the valence electrons of the isolated  $\text{N}$  atom occupy the valence  $s$ -orbital and other  $x$  valence electrons occupy the valence  $p$ -orbital. Both  $s$ - and  $p$ - orbitals form the  $sp^3$  hybrid orbital.

Some of the electrons of the above orbitals are inherited from other orbitals belonging to the same atom. The charge transfer from  $p$  orbital of the atom to the  $sp^3$  hybrid orbital of the  $\text{N}$  atom is calculated by using the following expression, which comes from the perturbation theory

$$\frac{\sqrt{c} (E_p - E_{sp^3})}{[E_p - E_{sp^3}]} - \dots \quad (25)$$

Where  $\epsilon_{\text{hybrid}}$  is the energy of the hybrid orbital,  $\epsilon_{\text{orbital}}$  is the energy of the orbital, and  $V_{\text{hybrid-orbital}}$  and  $V_{\text{orbital-orbital}}$  are the matrix elements for -interaction of hybrid and -interaction of orbital respectively. Normally the matrix element  $V_{\text{hybrid-orbital}}$  of -interaction has negligible value if the interaction occurs in a tetrahedral cell. (It has to be considered that  $s$  and  $p$  orbitals form the hybrid orbital of the gallium atom). Equation (25) determines the charge transfer is  $q$  electrons, which could have a significant value in determining that one or more electrons can be replaced from the orbital of the atom to the neighboring hybrid orbital of the Ga atom. Two conclusions can be made:

- i) The orbital of the atom does not participate in the ion-covalent bond although this orbital provides an electron for this bond; and
- ii) the ion-covalent bond is of type and it takes place on the basis of two hybrid orbitals – of the Ga atom and corresponding orbital of the atom. For the purpose of calculation the energy of the valence -orbital of the atom and be determined by Hartree-Fock method [68] under consideration of Koiller-Falicov assumption [69].

Localized wave functions must be used for calculation of the electron band structure of a quasi-elementary cell. LCAO methods from [70] are then used to calculated the electron band sub-structures. The primitive super-cell wurtzite is comprised of two cations and two anions. To represent the interactions between nearest neighbouring orbitals a tetrahedral cell of wurtzite is used. This cell also contains two cations and two anions, with each neighbouring its opposite type. We consider this quasi-elementary

cell to have the cations as  $\text{Ga}^{3+}$  atoms, and the anions to be atoms of either  $\text{As}^{3-}$  or  $\text{S}^{2-}$ . The same applies to the tetrahedron cell. The  $s$ - and  $p$ - state orbitals of the valence electrons of the Ga, As, and N atoms are used. Non-zero matrix elements represent interactions between the nearest neighbouring orbitals and the second neighbouring orbitals if the corresponding interaction exists. One (1) valence electron state exists for the  $s$ -orbital while three (3) exist for the  $p$ -orbital (  $p_x, p_y, p_z$  ). This corresponds to the LCAO Hamiltonian matrix of the tetrahedral cell having 16 rows and 16 columns.

There are five (5) different types of matrix elements in matrix  $H$ . Matrix elements for  $H_{ii}$  represent orbital energy terms when the atom is in the crystal. Energy terms for the  $s$ - and  $p$ - states of the isolated atoms  $A$ ,  $Ga$ , and  $N$  are designated by  $\epsilon_s$  and  $\epsilon_p$  respectively.

The matrix elements  $H_{ij}$  are connected with the widths of energy bands and they are defined as

(26)

Where  $\alpha$  and  $\beta$  is a real number. The coefficients  $C_i$  are obtained using the fitting method for wurtzite  $\text{GaAs}$  and wurtzite  $\text{GaS}$ . The energy terms  $\epsilon_s$  are taken from Herman and Skillman [70] for atoms  $\text{Ga}$ ,  $\text{As}$  and  $\text{N}$ .

Matrix elements  $H_{ij}$  for both (  $i, j = s, p_x, p_y, p_z$  ) and (  $i, j = p_x, p_y, p_z, s$  ) represent the interaction between atomic orbitals belonging to the tetrahedral cell and atomic orbitals of the second neighbors. These can be divided in two

types – interaction between two orbitals of one and the same kind of atoms – anion-anion and cation-cation, and interaction between two orbitals of different kind of atoms – anion-cation. The first type of interaction in the case of  $\text{Ga-N}$  is the interaction between atomic orbitals belonging to a tetrahedral cell and atomic orbitals, which are their second neighbors  $A-A$ ,  $Ga-Ga$ ,  $A-N$  and  $N-N$ . The corresponding matrix elements are  $V_{ll'}$  for both (  $\text{Ga-N}$  ) and (  $\text{Ga-N}$  ). The second type of interaction in the case of  $\text{Ga-N}$  is between orbitals  $A-Ga$  and  $Ga-N$ . The corresponding matrix elements are  $V_{ll'}$  for both (  $\text{Ga-N}$  ) and (  $\text{Ga-N}$  ). The matrix elements of both types can be defined in the following way

$$(27)$$

Where  $\vec{r}_{ll'}$  is the vector-distance between orbitals  $l$  and  $l'$  engaged in interaction and  $r_{ll'}$  is the module of the matrix element. The sum in (27) is over all parts of interacting orbitals  $l$  and  $l'$ . The module  $V_{ll'}$  is equal to zero if there is no interaction between two orbitals. If  $V_{ll'}$  is not zero there are a few possible expressions depending on the interacting orbitals  $l$  and  $l'$ :

- i) Between two  $s$  orbitals  $V_{ll'} = V_{ss}$ ;
- ii) Between the  $s$  orbital and  $p$  orbital [  $V_{sp}$  ], where  $V_{sp}$  is a numerical value depending on angle  $\theta$  between  $p$  orbital and the vector-distance  $\vec{r}_{ll'}$ ;

iii) Between two  $p$  orbitals [  $\dots$  ], where the meaning of numerical values [  $\dots$  ], and  $\dots$  are the same like  $\dots$ . The terms  $\dots$ ,  $\dots$  and  $\dots$  are matrix elements representing the interaction between corresponding orbitals. These terms are designated by  $\dots$  where  $\dots$  respectively and  $\dots$  represents each type of the corresponding  $p$  orbital.

The matrix elements  $\dots$  are given in [70] for interacting orbitals belonging to the tetrahedral cell. However the determinations in [70] cannot be used for the matrix elements  $\dots$  between orbitals belonging to second neighboring atoms. The muffin-tin orbital [71], [72] approach is used for determination of  $\dots$  in case of interactions between second neighboring orbitals in  $\dots$  (The matrix elements  $\dots$  corresponding to anion-anion orbital interactions and cation-cation orbital interactions are taken to be equal to zero because of orthogonal conditions of LCAO Bloch orbitals. The matrix element  $\dots$  for  $\dots$  has two values. The first one corresponds to a case  $\dots$  - interaction in  $\dots$  and the second – to a case  $\dots$  - interaction in  $\dots$ .)

The matrix elements  $\dots$  for (  $\dots$  &  $\dots$  &  $\dots$  ) are found using [70] for interactions between orbitals of atoms, which are nearest-neighbors (here  $\dots$  —, where  $\dots$  is structural factor, and  $\dots$  is mass of the electron). In this case the inter-atomic distances are taken to be equal to the corresponding distances of  $\dots$ , if there is  $\dots$  - interaction, and of  $\dots$  if the interaction is  $\dots$  - . The matrix elements  $\dots$  for (  $\dots$  &  $\dots$  ) are taken to be equal to zero

because only the interactions between nearest-neighboring orbitals and second-neighboring orbitals are being considered. The LCAO Hamiltonian matrix of a tetrahedral cell is determined by all cases of matrix elements discussed above.

$$H = \begin{vmatrix} H_{1\ 1} & H_{1\ 2} & \dots & H_{1\ 8} & H_{1\ 9} & H_{1\ 10} & \dots & H_{1\ 16} \\ H_{2\ 1} & H_{2\ 2} & \dots & H_{2\ 8} & H_{2\ 9} & H_{2\ 10} & \dots & H_{2\ 16} \\ \dots & \dots \\ H_{8\ 1} & H_{8\ 2} & \dots & H_{8\ 8} & H_{8\ 9} & H_{8\ 10} & \dots & H_{8\ 16} \\ \hline H_{9\ 1} & H_{9\ 2} & \dots & H_{9\ 8} & 0 & 0 & \dots & 0 \\ H_{10\ 1} & H_{10\ 2} & \dots & H_{10\ 8} & 0 & 0 & \dots & 0 \\ \dots & \dots \\ H_{16\ 1} & H_{16\ 2} & \dots & H_{16\ 8} & 0 & 0 & \dots & 0 \end{vmatrix} \quad (28)$$

The electron band sub-structure of a quasi-elementary cell can be calculated by Hamiltonian matrix (28) for tetrahedral cell of this quasi-elementary cell. There are five different Hamiltonian matrix (28) for wurtzite and they are determined by corresponding five different tetrahedral cells. Detailed investigation shows that both the optical absorption and the photoluminescence spectra for semiconductor compound alloys can respectively be taken as the parts of the LCAO electron band structures corresponding to configurations of the quasi-elementary cells giving deepest energy pockets for the electrons in the conduction band, deepest energy pockets for the holes in the valence band, and that these energy pockets are on shortest distances. In order for these three conditions to satisfy the five different configurations of the wurtzite quasi-elementary cells (determining corresponding sectors of the LCAO electron band structure) taken in the following order must be used for :

- 1) pure quasi-elementary cell surrounded by second neighboring cations;

2) mixed                    quasi-elementary cell containing    atoms of    and    atoms of  
surrounded by second neighboring    cations;

3) mixed                    quasi-elementary cell containing    atom of    and    atom of  
surrounded by second neighboring    cations;

4) mixed                    quasi-elementary cell containing    atoms of    and    atoms of  
surrounded by second neighboring    cations;

5) pure                    quasi-elementary cell surrounded by second neighboring    cations.

### 7.1.3. Optical properties of $\text{GaA}_y\text{N}_{1-y}$

The optical properties of disordered semiconductors are investigated in [67]. There are two main types:

i) Tunnel optical absorption (Figure 66). The basis of this phenomenon is the overlapping between the electron wave function  $|i\rangle$  of the initial electron state and the electron wave function  $|f\rangle$  of the final electron state in terms of the optical transition. The red circle represents the initial state of the electron wave function while the blue is the final for the crystal. It is important to note that the state    is an electron state).

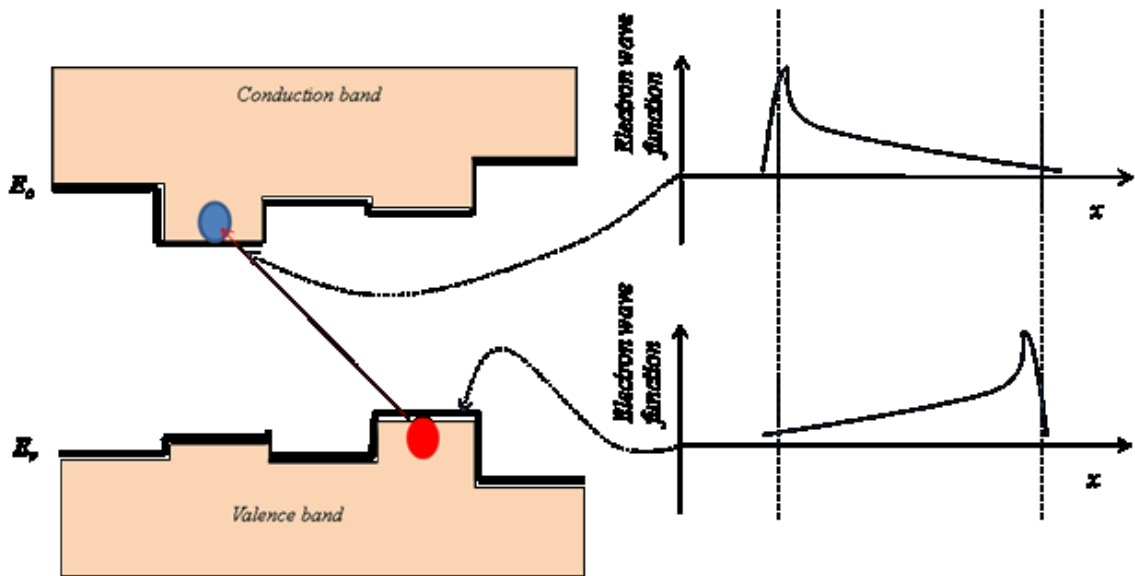


**Figure 66. Tunnel Optical Absorption.**

ii) Excitons of the structure (Figure 67). The basis of this phenomenon is the Coulomb interaction between an electron located in a pocket of the conduction band and a hole located in pocket of the valence band. This quasi-particle can be characterized by two parameters: binding energy and hydrogen like energy levels.

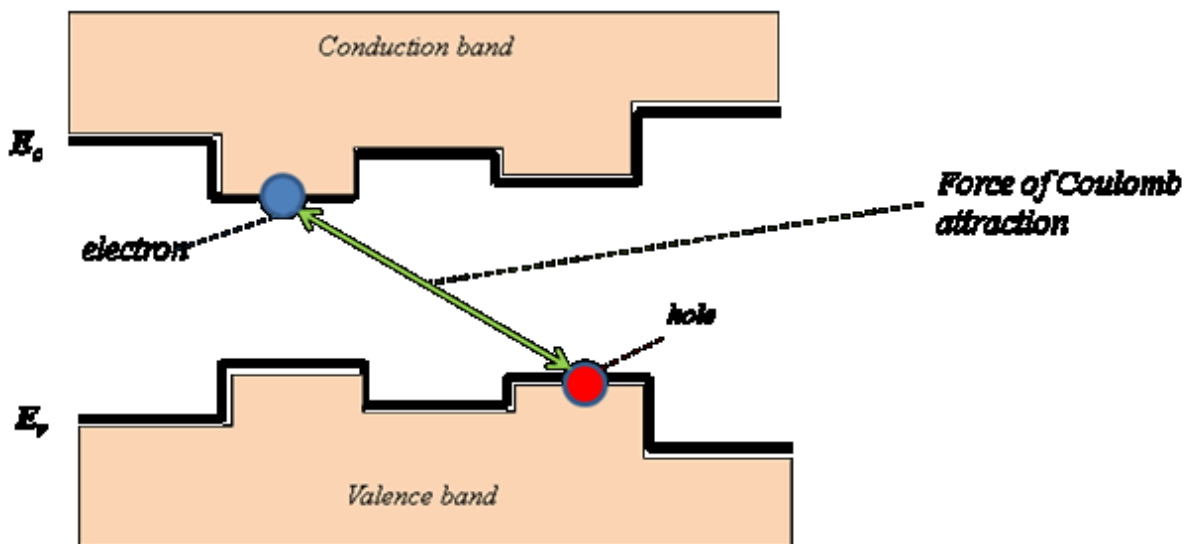


**Figure 67. Excitation of the structure.**

## 7.2. Structure of Isolated Oxygen Impurity States in GaN

Oxygen is a common contaminant in GaN. There are two possible positions for oxygen atoms incorporating into the structure of GaN:

- 1) The oxygen atom can be alloyed to form the ternary compound GaN<sub>1-x</sub>O<sub>x</sub> where oxygen is substituting on the nitrogen site.
- 2) The oxygen atom can be an isolated as an interstitial atom in the GaN matrix, or it can be a non-isolated interstitial atom in the same structure if the concentration of the non-alloyed O impurities is higher. The electron state structures of isolated interstitial O atoms in real GaN (containing clusters of O<sub>2</sub>, clusters of O<sub>3</sub> and clusters of non-stoichiometric GaN) is currently a subject of investigation. The hydrogen like impurity atom analysis is applied and the behavior of interstitial O atom is investigated for following cases:
  - i) Incorporation of the oxygen atom in a cluster of pure GaN;
  - ii) Incorporation of the oxygen atom in a cluster of GaN;
  - iii) Incorporation of the oxygen atom in cluster of non-stoichiometric GaN where gallium atoms substitute on nitrogen sites. The corresponding impurity levels are calculated and their positions in the electron band structure of real GaN are shown.

### 7.2.1. Electron Band Structures of wurtzite $\text{GaO}_y\text{N}_{1-y}$ and of Non-Stoichiometric GaN:Ga

LCAO electron band structures of both wurtzite  $\text{GaO}_y\text{N}_{1-y}$  and wurtzite non-stoichiometric GaN:Ga for points  $\Gamma$  are calculated by the method given in [67]. In the case of  $\text{GaO}_y\text{N}_{1-y}$  it is considered that oxygen is the atom  $A$  introduced above (i.e.

$\text{GaO}_y\text{N}_{1-y}$ ). Detailed investigation shows that for the purpose of inter-band electron transitions for semiconductor compound, alloys can be taken from parts of the LCAO electron band structures. The corresponding configurations of the quasi-elementary cells giving deepest energy pockets for electrons in the conduction band, and deepest energy pockets for holes in the valence band. These energy pockets are situated between the shortest distances. In order for these three conditions to be satisfied, configurations of five different types of wurtzite quasi-elementary cells are taken in the following order:

- i) For  $\text{GaO}_y\text{N}_{1-y}$  (refer to the energy separations are shown in Figure 68) the sectors are identified as the following: Sector 1)  $\text{GaO}_y\text{N}_{1-y}$  quasi-elementary cell which is surrounded by second neighboring  $\text{O}^{2-}$  anions; Sector 2)  $\text{GaO}_y\text{N}_{1-y}$  quasi-elementary cell having second neighboring anions  $\text{O}^{2-}$  and  $\text{N}^{3-}$ ; Sector 3) a mixed  $\text{GaO}_y\text{N}_{1-y}$  quasi-elementary cell containing two atoms of  $\text{Ga}^{3+}$ , one atom of  $\text{O}^{2-}$  and one atom of  $\text{N}^{3-}$  having second neighboring anions  $\text{O}^{2-}$  and  $\text{N}^{3-}$ ; Sector 4)  $\text{GaO}_y\text{N}_{1-y}$  quasi-elementary cell having second neighboring anions  $\text{O}^{2-}$  and  $\text{N}^{3-}$ ; Sector 5)  $\text{GaO}_y\text{N}_{1-y}$  quasi-elementary cell surrounded by second neighboring  $\text{O}^{2-}$  anions.
- ii) For non-stoichiometric GaN:Ga (refer to the energy separation shown in Figure 70): Sector 1) pure GaN:Ga quasi-elementary cell surrounded by second neighboring  $\text{N}^{3-}$  anions; Sector 2) mixed GaN:Ga quasi-elementary cell

containing atoms of and atoms of having second neighboring anions; Sector 3) mixed quasi-elementary cell containing atoms of and atom of having second neighboring anions; Sector 4) mixed quasi-elementary cell containing atoms of and atoms of with second neighboring anions; Sector 5) pure quasi-elementary cell surrounded by second neighboring anions.

The LCAO electron band structure calculations for each quasi-elementary cell are performed by the method [67] described above. The electron energy terms and for both atom and atoms are taken from [73] and the same energy terms for the atom substituting on the site in the structure of are determined to be and . It is found that the charge transfer from the atom in direction to the atom is . This value is derived on the basis of preliminary determined matrix elements and . (It must be noted that the derived value of charge transfer implies that the valence electron cloud of the atom is partially displaced in direction towards the atom in the corresponding quasi-elementary cell). The nearest-neighbor matrix elements are determined according to [70] and the required inter-atomic distances are calculated on the basis of the tetrahedral radii of atoms , and . MATLAB software has been used for all calculations. The calculated electron band structures are provided in Figure 68 for and in Figure 70 for non-stoichiometric . The energy levels and are determined by taking the vacuum energy level as zero. The energy difference gives the energy band gap of sector 5. Shifting of the boundaries for the energy band gaps in Figure 68 and

in Figure 70 and the corresponding energy intervals is due to defects in the crystal lattices of both  $\text{GaO}_y\text{N}_{1-y}$  and  $\text{Ga}_2\text{O}_3$  – i.e. the existence of two sorts of atoms on anionic sites.

The LCAO electron band structure of pure  $\text{Ga}_2\text{O}_3$  is taken from sectors 5 of both Figure 68 and Figure 70.

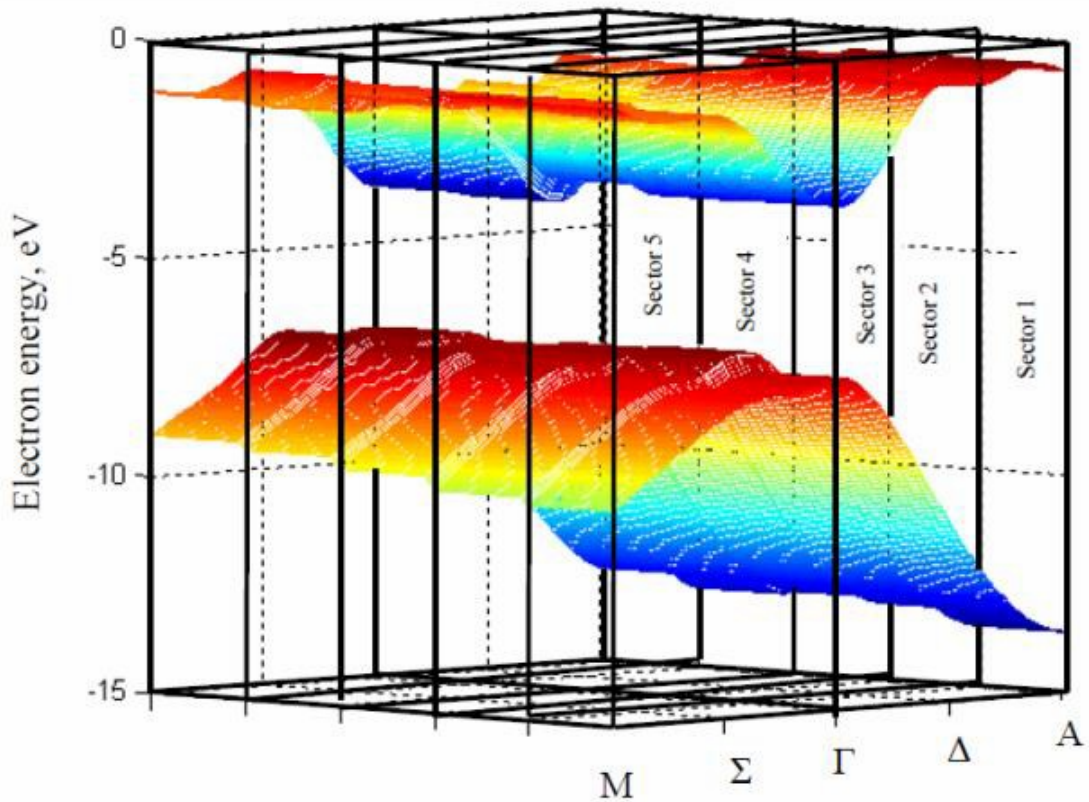


**Figure 68. Electron band structure for wurtzite  $\text{GaO}_y\text{N}_{1-y}$ . Only the sub bands corresponding to the bottom of the conduction band and to the top of the valence band are provided.**

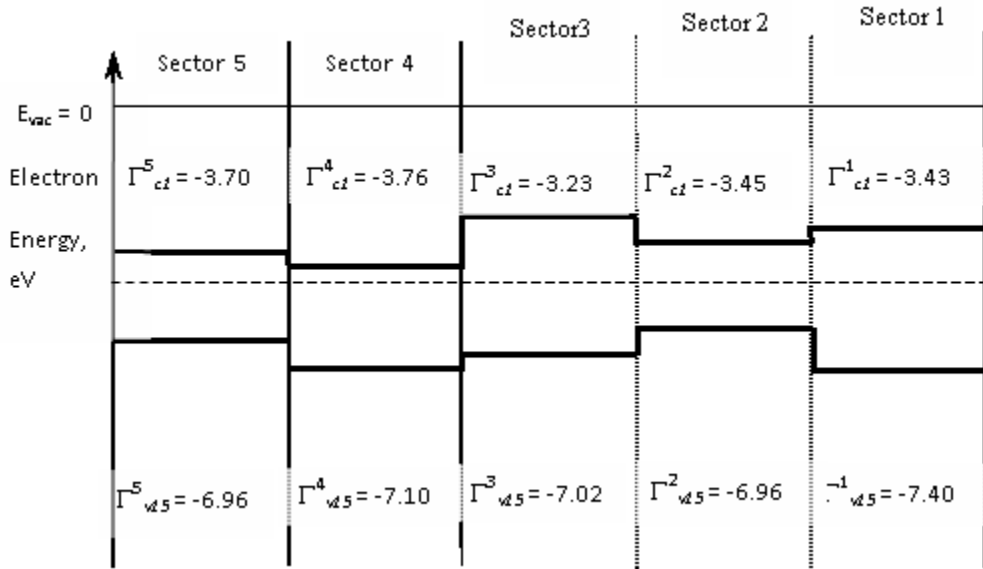


**Figure 69. Electron band structure of  $\text{GaO}_y\text{N}_{1-y}$  for point only and donor level  $E_d = -3.87$  eV (not to scale)**

### 7.2.2. Electronic Structures of Isolated Oxygen Impurity States

The electronic structure of isolated oxygen impurity states can be found by considering that the valence electrons of an incorporated interstitial atom are not engaged in forming of ion-covalent bonds in , and . Therefore a relatively long distance influence of the valence states in the above clusters can be expected and the hydrogen like impurity atom analysis in [74] can be applied for isolated interstitial atoms hosted in a real lattice. This means that the Schrödinger equation for a hydrogen atom, with effective electron mass and dielectric constant having values for clusters , and , can be used.

$$(29)$$

Where is ground-state wave function of the form

$$- - - \tag{30}$$

Where  $a_0$  is an effective Bohr radius, which determines the localization radius of the wave function and

$$\text{---} \tag{31}$$

The solution of (30) gives the isolated electron states of the impurity atom

$$\text{-----} \tag{32}$$

Where  $n$  is integer number greater than zero. For determination of the isolated electron states

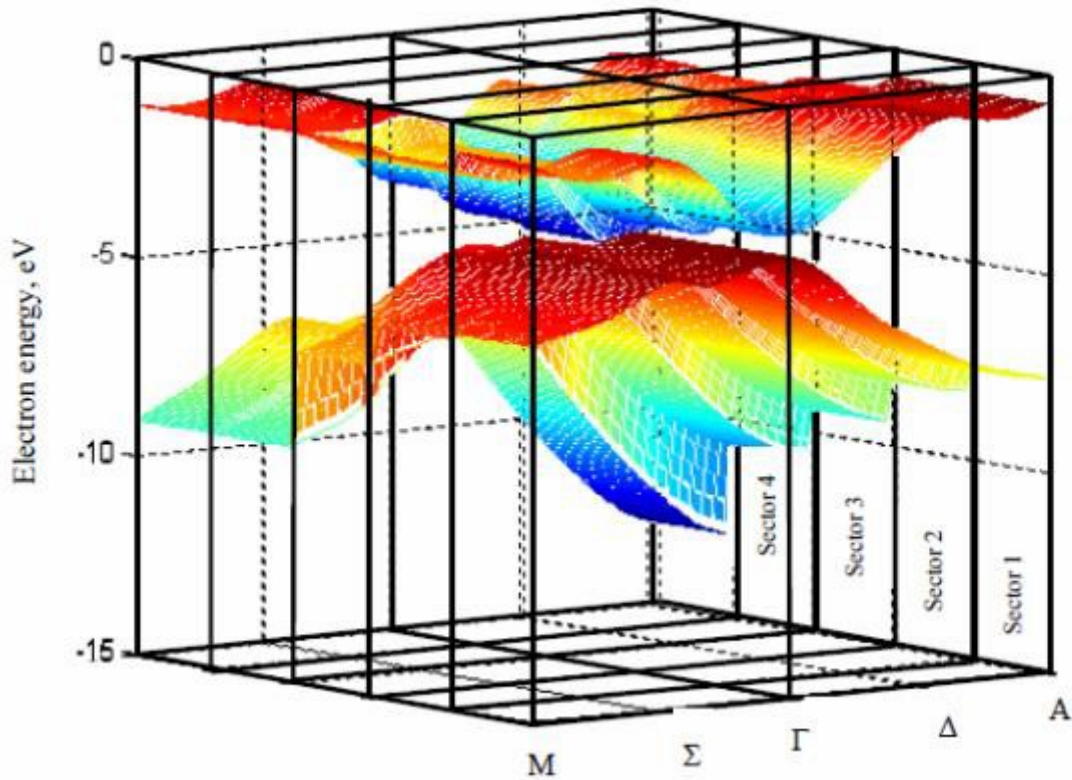


**Figure 70. Electron band structure for wurtzite non-stoichiometric GaN:Ga. Only the sub bands corresponding to the bottom of the conduction band and to the top of the valence band are provided.**

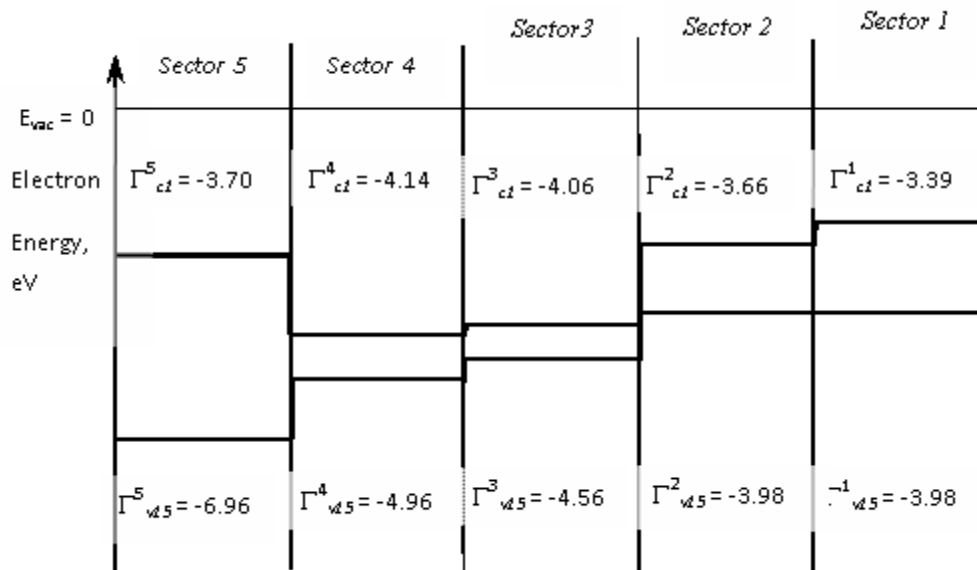


**Figure 71. Electron band structure of non-stoichiometric GaN:Ga for point  $\Gamma$  only and donor level  $E_d = -3.79$  eV (not to scale)**

Equations (31) and (32) are used for determination of the localization radii and electron energy states respectively of interstitially incorporated atoms in clusters, and . Values for are taken from [70] and [67] respectively. The following results have been obtained (relative to zero energy at the vacuum level):

i) If the atom is interstitially incorporated in a cluster of pure the impurity state has an energy of (Figure 72), which acts as a donor level with ionization energy . Also this state is a donor level (Figure 68) with an ionization energy of for a cluster of .

ii) The impurity state has energy if the atom is interstitially incorporated in a cluster of , which acts as a donor level with ionization energy . Also this state is a donor level with ionization energy of for a cluster of (Figure 73).

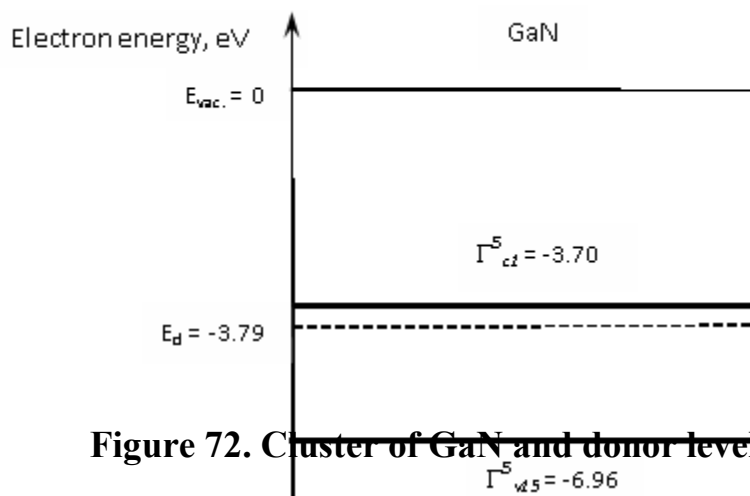


**Figure 72. Cluster of GaN and donor level  $E_d = -3.79$  eV.**

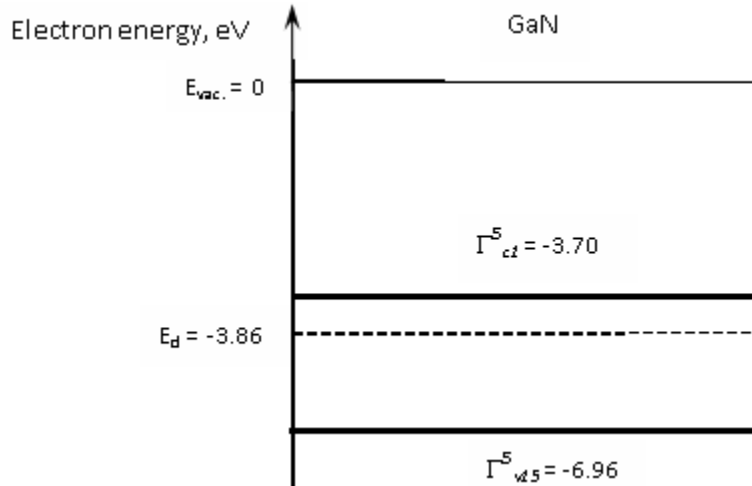


**Figure 73. Cluster of GaN and donor level  $E_d = -3.86$  eV.**

- iii) Interstitial incorporation of an atom into a cluster of wurtzite non-stoichiometric is not investigated. Also the influence of interstitial incorporations of atoms in clusters of both and on the conductivity of cluster is not investigated. This is because there is an overlap of the conduction band of sector 3 and the valence band of sector 2 of the electron band structure of non-stoichiometric (shown in Figure 71). This overlap ensures that the conduction band of that cluster is populated at all times with electrons coming from the valence band such that the impact of any impurities has no effect.

### 7.3. Optical Absorption Spectra of GaN

In this section the above LCAO electron band structure calculations are connected with the optical properties of a real semiconductor. It is shown that:

- i) The results of non-stoichiometric  $\text{Cu}_2\text{O}$  show that these clusters have metal behavior in terms of the conductivity due to the overlap between the conduction band of the Sector 3 and the valence band of Sector 2 despite the pure  $\text{Cu}_2\text{O}$  quasi-elementary cell (Sector 1) showing existence of an energy band gap. It implies that it is expected that these clusters have contributions to the electrons in the conduction band and do not have contributions to the optical absorption edge.
- ii) The results from the  $\text{Cu}_2\text{O}$  crystal show that these clusters save the semiconductor nature of the real  $\text{Cu}_2\text{O}$  and that they have contributions to the variation of the energy band gap due to both: inter-band absorption in Sector 5 of Figure 68) and tunnel optical absorption occurring between states  $\Gamma_1$  and  $\Gamma_2$  of Figure 69. The calculations shows a change of the energy band gap of real  $\text{Cu}_2\text{O}$  in the range of 0.5 eV to 1.5 eV due to influence of oxygen contamination. As such we can consider that the range of the energy band gaps from our lab grown samples in Table 7 from 0.5 eV to 1.5 eV is due to the incorporation of  $\text{Cu}$  atoms substituting on  $\text{O}$  sites forming cluster of  $\text{Cu}_2\text{O}$ .
- iii) The optical absorption in direction  $\Gamma_1$  in the  $k$ -space (Figure 68 and Figure 70 above and Figure 74 below) determines the optical absorption peak  $\Gamma_1$  in Table 7. This peak is connected mainly with both matrix elements  $\Gamma_1$  and  $\Gamma_2$  which are the result of the interactions between neighboring atomic orbitals which depend on the inter-atomic distance between nearest neighbors. The experimental results show that the energy interval  $\Gamma_1$  to  $\Gamma_2$

dominates in these absorptions. Due to this reason one can conclude that the average inter-atomic distances are relatively stable because there is not a significant change in the dominating values of  $\langle r \rangle$ .

- iv) Table 7 shows that the peak  $\epsilon_2$  remains relatively stable, but at the same time the optical absorption edge changes significantly in range  $\lambda_{opt}$  to  $\lambda_{opt}^0$  which leads to the following conclusions: a) the change of the optical absorption edge below  $\lambda_{opt}^0$  is due to incorporation of other (other than  $\text{Ga}^{3+}$ ) impurity atoms and other defects in the structure of the real  $\text{GaAs}$ . These defects determine the tunnel optical absorption for point  $\Gamma$  of the electron band structure. b) No tunnel optical absorption exists in direction  $[100]$  because the electron states are not localized in the corresponding energy pockets in this direction.
- v) The optical absorption in direction  $[100]$  in the  $k$ -space (Figure 68 and Figure 70 above and Figure 74 below) determines the optical absorption peak  $\epsilon_2$  from Table 7. The results shown in Table 7 related to this absorption confirm the conclusions made in above section iv).

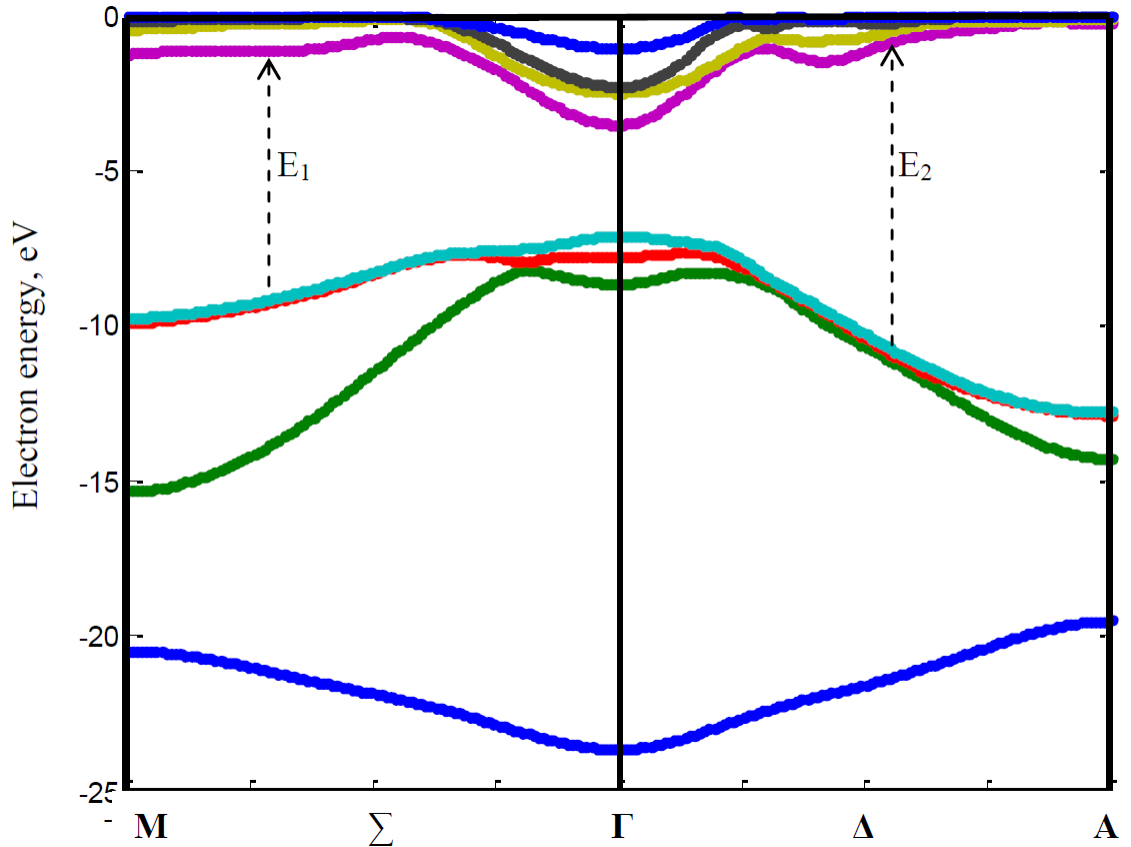


**Figure 74. Electron band structure of GaN in  $k$ -space only.**

**Table 7. Summary of GaN Sample Data.**

Sample Name	Band Gap		
2012-02-15-2-GaN	3.2500	6.5600	6.6600
2012-02-15-3-GaN	3.0500	6.5600	6.6350
2012-02-15-4-GaN	3.0400	6.4400	6.6590
2012-02-16-1-GaN	3.0500	6.4800	6.5800
2012-02-16-2-GaN	2.5000	6.4000	6.4800
2012-02-17-1-GaN	2.7000	6.2900	6.4800
2012-02-17-2-GaN	2.5000	6.4600	6.5300

2012-02-17-3-GaN	2.6500	6.5950	6.7020
2012-02-26-1-GaN	2.8250	6.3910	6.4920
2012-02-27-1-GaN	2.7500	6.4920	6.5950
2012-02-27-2-GaN	2.9000	6.5950	6.6660
2012-02-27-3-GaN	2.6500	6.6300	6.7020
2012-02-28-1-GaN	2.7000	6.5260	6.5950
2012-02-28-2-GaN	2.5000	6.5260	5.5600
2012-02-29-3-GaN	2.4000	6.5600	6.6300
2012-03-06-1-GaN	2.9000	6.4580	6.5600
2012-03-06-2-GaN	2.8500	6.4920	6.6300
2012-03-07-1-GaN	2.9500	6.4920	6.6660
2012-03-07-2-GaN	3.1500	6.5600	6.6660
2012-03-09-1-GaN	2.9000	6.2620	6.3910
2012-03-12-2-GaN	3.1000	6.1380	6.2310
2012-03-13-2-GaN	2.7500	6.5600	6.6300
2012-03-14-1-GaN	3.0000	5.9900	6.1380
2012-03-14-2-GaN	2.8750	6.0480	6.1380
2012-03-14-3-GaN	3.2500	6.3260	6.4580
2012-03-15-1-GaN	2.8800	5.7400	5.8210
2012-03-15-2-GaN	3.2000	6.0480	6.1690
2012-03-16-2-GaN	3.1000	6.0480	6.1380
2012-03-18-2-GaN	3.1000	5.6880	5.7670

## **Chapter 8 Conclusion**

The MEAgrow growth system offers some key advantages over traditional MOCVD and MBE type reactors. Compatible pressures and temperatures for the growth of both indium nitride and gallium nitride within the same system have been established and documented. High quality materials of both types have been obtained. A number of challenges in the III-Nitride material system have been overcome. The plasma system has also been thoroughly tested and well documented.

The MEAgrow reactor has been documented throughout a broad range of parameter space for both indium nitride and gallium nitride films including growth temperature, chamber pressure, nitrogen flow through the plasma head, plasma RF power, metalorganic input flux.

The effects of program operation have been evaluated. Addition of a desorption stage in the gallium nitride film growth provides a marked advantage with film morphology at the cost of prolonging growth time. Increasing the “plasma only” time during growth can impart improvements to the film though droplet formation remains a challenge. For indium nitride growths the addition of a cooling stage during growth improves the quality of the film. Segregating the “plasma only” and “plasma + setup” times can reduce the

amount of expensive TMI required for growth, but care must be taken to allow for adequate “plasma + setup” for the MO gas lines to stabilize or film quality suffers.

Buffer layers have been developed which improve the quality of subsequent films grown. These layers have been compared to commercially available templates and have been shown to provide an equal advantage.

Heterostructures have been created using previously developed single film indium nitride and gallium nitride film growths as templates. Optimising metalorganic input flux, the addition of an alumina mask around the substrate, and use of a buffer layer has led to a sharp interface between the two films. The addition of a titanium backing to the substrates to even out heat distribution during growth, changes to program parameters, addition of a nitridation period prior to growth, and baking the substrates to reduce damage from substrate polishing has led to a further improved heterostructure.

Growth parameters have been established to produce self-catalytic indium nitride nanowires. These nanowires consist of an indium nitride shaft with a metal droplet at the top which can be etched away. Growth occurs under metal rich conditions.

Initial experiments into contact development have been performed through a collaboration between the University of Manitoba and Lakehead University. Though conditions have been established for deposition of contacts, the structures themselves require further improvement. Specifically, v-pitting defects must be reduced and the top gallium nitride layer must be grown free of indium contamination.

The results of many samples grown have been subjected to a thorough theoretical treatment. By breaking down the composition of the films and impurities into 5 sectors

and analysing the interactions between these quasi-primitive cells a thorough understanding of electrical and optical behaviour has been established. Non-stoichiometric GaN:Ga acts similar to a metal due to the overlap between the conduction band of GaN-A (with 1:1 N:A ratio) and the valence band of GaA-N (with 1.5:0.5 A:N ratio). A GaN crystal with oxygen impurities substituting for nitrogen still acts as a semiconductor but the bandgap varies with the content of the impurity. Impurities other than oxygen and other crystal defects contribute to the lower than optical absorption edge.

Future work should include:

- i) Much of the effort of this research project has been spent on the optimization of individual indium nitride and gallium nitride films, as well as the heterostructure development. However, the limits of the system have not been reached and the best yet films have yet to be obtained.
- ii) Plasma models are still a very active area of research. Modelling of the MEAgrow plasma source is far beyond the scope of this work however may present a unique project for a future student of the Lakehead Semiconductor Research Lab.

It is hoped that this research project has made a contribution in the field of III-Nitride semiconductors. The MEAgrow method of thin film production overcomes many of the challenges in the production of these important next generation semiconductor devices.

## Chapter 9

### References

- [1] J. W. Orton, *The Story of Semiconductors*. Oxford University Press, 2008.
- [2] T. Tansley, C. Foley, and M. Tokuda, “Electron mobility in indium nitride,” *Electron. Lett.*, vol. 20, no. 25, pp. 1066–1068, 1984.
- [3] X. Sun, W. B. Liu, D. S. Jiang, Z. S. Liu, S. Zhang, L. L. Wang, H. Wang, J. J. Zhu, L. H. Duan, Y. T. Wang, D. G. Zhao, S. M. Zhang, and H. Yang, “Photoelectric characteristics of metal/InGaN/GaN heterojunction structure,” *J. Phys. D. Appl. Phys.*, vol. 41, no. 16, p. 165108, Aug. 2008.
- [4] K. S. A. Butcher, “Aluminium Nitride Insulating Thin Films Grown on Damage Susceptible Semiconductors,” Macquarie University, Sydney, 1997.
- [5] P. T. Terziyska, K. S. A. Butcher, D. Gogova, D. Alexandrov, P. W. Binsted, and G. Wu, “InN nanopillars grown from In-rich conditions by migration enhanced afterglow technique,” *Mater. Lett.*, vol. 106, pp. 155–157, May 2013.
- [6] R. Eden, “Market Forecasts for Silicon Carbide & Gallium Nitride Power Semiconductors,” in *The World Market for Silicon Carbide & Gallium Nitride Power Semiconductors*, 2013.
- [7] S. C. Jain, M. Willander, J. Narayan, and R. Van Overstraeten, “III–nitrides: Growth, characterization, and properties,” *J. Appl. ...*, vol. 87, no. 3, p. 965, 2000.
- [8] M. Winter, “WebElements,” 2011. [Online]. Available: <http://www.webelements.com/>.
- [9] L. Gustavsson, “Hollow Cathode Deposition of Thin Films,” Uppsala University, 2006.
- [10] K. S. A. Butcher, *InN, a historic review From obscurity to controversy*. Research Signpost, 2004.
- [11] J. Chu and A. Sher, *Physics and properties of narrow gap semiconductors*. Springer, 2007.

- [12] S. M. Rossnagel, "Glow Discharge Plasmas and Sources for Etching and Deposition," in *Thin Film Processes II*, J. L. Vossen and W. Kern, Eds. San Diego: Academic Press, Inc., 1991.
- [13] A. G. Bhuiyan, A. Hashimoto, and A. Yamamoto, "Indium nitride (InN): A review on growth, characterization, and properties," *J. Appl. Phys.*, vol. 94, no. 5, p. 2779, 2003.
- [14] O. Ambacher and R. Article, "Growth and applications of group III-nitrides," *J. Phys. D. Appl. Phys.*, vol. 31, pp. 2653–2710, 1998.
- [15] K. S. A. Butcher and T. L. Tansley, "InN, latest development and a review of the band-gap controversy," *Superlattices Microstruct.*, vol. 38, no. 1, pp. 1–37, Jul. 2005.
- [16] D. Neumayer and J. Ekerdt, "Growth of group III nitrides. A review of precursors and techniques," *Chem. Mater.*, no. 14, pp. 9–25, 1996.
- [17] F. Ponce and D. Bour, "Nitride-based semiconductors for blue and green light-emitting devices," *Nature*, vol. 386, no. 6623, pp. 351–359, 1997.
- [18] S. Strite and H. Morko, "GaN, AlN, and InN: A review," *J. Vac. Sci. Technol. B Microelectron. Nanom. Struct.*, vol. 4, no. 10, pp. 1237–1266, 1992.
- [19] A. Rockett, *The Materials Science of Semiconductors*. Springer, 2008.
- [20] M. F. Schubert, J. Xu, J. K. Kim, E. F. Schubert, M.-H. Kim, S. Yoon, S. M. Lee, C. Sone, T. Sakong, Y. Park, and H. Kim, "Polarization-matched GaInN/AlGaInN multi-quantum-well light-emitting diodes with reduced efficiency droop," *Appl. Phys. Lett.*, vol. 93, no. 4, p. 041102, 2008.
- [21] K. S. A. Butcher, D. Alexandrov, P. Terziyska, V. Georgiev, D. Georgieva, and P. W. Binsted, "InN grown by migration enhanced afterglow (MEAglow)," *Phys. Status Solidi*, vol. 209, no. 1, pp. 41–44, Jan. 2012.
- [22] R. Quay, "Epitaxy for III-N-Based Electronic Devices," in *Gallium Nitride Electronics*, Springer, 2008.
- [23] D. Alexandrov, "Semiconductor Compound Alloys Related to InN and Their Application in Design of Semiconductor Lasers," in *CCECE/CCGEI, Saskatoon, May 2005*, 2005, no. May, pp. 332–339.
- [24] G. Lucovsky and D. V. Tsu, "Formation of Inorganic Films by Remote Plasma-Enhanced Chemical-Vapor Deposition," in *Thin Film Processes II*, 1991, pp. 565–619.

- [25] K. S. A. Butcher, B. W. Kemp, I. B. Hristov, P. Terziyska, P. W. Binsted, and D. Alexandrov, "Gallium Nitride Film Growth Using a Plasma Based Migration Enhanced Afterglow Chemical Vapor Deposition System," *Jpn. J. Appl. Phys.*, vol. 51, no. 1, p. 01AF02, Jan. 2012.
- [26] T. F. Kuech and K. F. Jensen, "OMVPE of Compound Semiconductors," in *Thin Film Processes II*, 1991, pp. 369–442.
- [27] A. Timoshkin, "DFT modeling of chemical vapor deposition of GaN from organogallium precursors. 1. Thermodynamics of elimination reactions," *J. Phys. Chem. A*, pp. 3240–3248, 2001.
- [28] A. Fridman, L. A. Kennedy, A. Alexander, A. Lawrence, F. Routledge, and P. Square, *Plasma physics and engineering*. Taylor & Francis Routledge, 2004.
- [29] K. S. A. Butcher, D. Alexandrov, P. Terziyska, V. Georgiev, and D. Georgieva, "Initial experiments in the migration enhanced afterglow growth of gallium and indium nitride," *Phys. Status Solidi*, vol. 9, no. 3–4, pp. 1070–1073, Mar. 2012.
- [30] J. Hopwood, C. R. Guarnieri, S. J. Whitehair, and J. J. Cuomo, "Langmuir probe measurements of a radio frequency induction plasma," *J. Vac. Sci. Technol. A Vacuum, Surfaces, Film.*, vol. 10598, no. April 1992, pp. 152–156, 1993.
- [31] B. Yacobi, *Semiconductor Materials: An Introduction to Basic Principles*. Kluwer Academic Publishers, 2003.
- [32] P. Chen, R. Zhang, Z. M. Zhao, D. J. Xi, B. Shen, Z. Z. Chen, Y. G. Zhou, S. Y. Xie, W. F. Lu, and Y. D. Zheng, "Growth of high quality GaN layers with AlN buffer on Si(111) substrates," *J. Cryst. Growth*, vol. 225, no. 2–4, pp. 150–154, May 2001.
- [33] S. Karmalkar, M. S. Shur, and R. Gaska, "GaN-Based Power High Electron Mobility Transistors," in *Wide Energy Bandgap Electronic Devices*, F. Ren and J. C. Zolper, Eds. World Scientific, 2003, pp. 173–213.
- [34] B. Liu, T. Kitajima, D. Chen, and S. R. Leone, "Growth modes of InN (000-1) on GaN buffer layers on sapphire," *J. Vac. Sci. Technol. A Vacuum, Surfaces, Film.*, vol. 23, no. 2, p. 304, 2005.
- [35] C. Poblenz, P. Waltereit, and J. S. Speck, "Uniformity and control of surface morphology during growth of GaN by molecular beam epitaxy," *J. Vac. Sci. Technol. B Microelectron. Nanom. Struct.*, vol. 23, no. 4, p. 1379, Jul. 2005.
- [36] E. Trybus, "Molecular Beam Epitaxy growth of InN and InGaN Materials for Photovoltaic Applications," Georgia Institute of Technology, 2009.

- [37] M. Yang, “Nitriding – fundamentals , modeling and process optimization,” Worcester Polytechnic Institute, 2012.
- [38] J.-S. Paek, K.-K. Kim, J.-M. Lee, D.-J. Kim, M.-S. Yi, D.-Y. Noh, H.-G. Kim, and S.-J. Park, “Nitridation of sapphire substrate and its effect on the growth of GaN layer at low temperature,” *J. Cryst. Growth*, vol. 200, no. 1–2, pp. 55–62, Apr. 1999.
- [39] A. B. Communications, “Compound Semiconductor,” vol. 17, no. 7, 2011.
- [40] R. S. Pengelly, S. M. Wood, J. W. Milligan, S. T. Sheppard, and W. L. Pribble, “A Review of GaN on SiC High Electron-Mobility Power Transistors and MMICs,” *IEEE Trans. Microw. Theory Tech.*, vol. 60, no. 6, pp. 1764–1783, Jun. 2012.
- [41] S. S. Li, *Semiconductor physical electronics*, 2nd ed. New York: Springer Science+Business Media LLC, 2006.
- [42] V. Siklitsky, “New Semiconductor Materials. Characteristics and Properties.” [Online]. Available: <http://www.ioffe.rssi.ru/SVA/NSM/>.
- [43] P. Specht, R. Armitage, J. Ho, E. Gunawan, Q. Yang, X. Xu, C. Kisielowski, and E. . Weber, “The influence of structural properties on conductivity and luminescence of MBE grown InN,” *J. Cryst. Growth*, vol. 269, no. 1, pp. 111–118, Aug. 2004.
- [44] K. S. Dicks, “Concentrated PV,” *PV Insider*, Nov-2011.
- [45] Lakehead Communications, “MEAGlow Semiconductor Research Laboratory Opens.” Lakehead University, Thunder Bay, 2011.
- [46] J. Briones, “The Bright Road Ahead for Ontario Company Meaglow.” MaRS, 2011.
- [47] K. S. A. Butcher, P. Terziyska, D. Alexandrov, V. Georgiev, and D. Georgieva, “Nitride Film Growth by Migration Enhanced Afterglow (MEAGlow).”
- [48] H. Tang, Z. Q. Fang, S. Rolfe, J. A. Bardwell, and S. Raymond, “Growth kinetics and electronic properties of unintentionally doped semi-insulating GaN on SiC and high-resistivity GaN on sapphire grown by ammonia molecular-beam epitaxy,” *J. Appl. Phys.*, vol. 107, no. 10, p. 103701, 2010.
- [49] R. Gergova, K. S. A. Butcher, P. W. Binsted, and D. Gogova, “Initial results for epitaxial growth of InN on gallium oxide and improved Migration-Enhanced Afterglow Epitaxy growth on gallium nitride,” *J. Vac. Sci. Technol. B Microelectron. Nanom. Struct.*, vol. 32, no. 3, p. 031207, May 2014.

- [50] S. Suihkonen, J. Sormunen, V. T. Rangel-Kuoppa, H. Koskenvaara, and M. Sopanen, "Growth of InN by vertical flow MOVPE," *J. Cryst. Growth*, vol. 291, no. 1, pp. 8–11, May 2006.
- [51] P. W. Binsted, K. S. A. Butcher, D. Alexandrov, P. Terziyska, D. Georgieva, R. Gergova, and V. Georgiev, "InN on GaN Heterostructure Growth by Migration Enhanced Epitaxial Afterglow (MEAglow)," *MRS Proc.*, vol. 1396, Jan. 2012.
- [52] P. W. Binsted, D. Alexandrov, K. S. A. Butcher, R. Gergova, D. R. Oliver, M. Mcclarty, and I. Yahyaie, "Gallium nitride on indium nitride heterostructure growth by migration enhanced afterglow (MEAglow) (submitted only)," *Phys. Status Solidi*, 2013.
- [53] M. Mcclarty and D. R. Oliver, "Substrate Characterization and Metallic Contact Selection and Deposition on Compensated InN / GaN Wafers (Private Correspondance)," Winnipeg.
- [54] P. P.-T. Chen, K. S. A. Butcher, E. M. Goldys, T. L. Tansley, and K. E. Prince, "High energy Urbach characteristic observed for gallium nitride amorphous surface oxide," *Thin Solid Films*, vol. 496, no. 2. pp. 342–345, Feb-2006.
- [55] Y. C. Yeo, T. C. Chong, and M. F. Li, "Journal of Applied Physics," *J. Appl. Phys.*, vol. 83, p. 1429, 1998.
- [56] K. Karch, J. M. Wagner, and F. Bechstadt, "Ab initio study of structural, dielectric, and dynamical properties of GaN," *Phys. Rev. B*, vol. 57, p. 7043, 1998.
- [57] C. Noguez, "Spectroscopic theoretical study of the atomic reconstruction of GaN(101 $\bar{0}$ )," *Phys. Rev. B*, vol. 58, p. 12641, 1998.
- [58] K. Amimer, A. Georgakilas, T. Tsagaraki, M. Androulidak, D. Cengher, L. Toth, B. Pecz, and M. Calamiotou, "Single-crystal hexagonal and cubic GaN growth directly on vicinal (001) GaAs substrates by molecular-beam epitaxy," *Appl. Phys. Lett.*, vol. 76, p. 2580, 2000.
- [59] E. Stach, M. Kelsch, W. S. Wong, E. C. Nelson, T. Sands, and N. W. Cheung, "Structural Characterization of Laser Lift-off GaN," in *Materials Research Society Symposium*, 2000, p. 614.
- [60] S. Pantelides and W. Harrison, "Structure of the valence bands of zinc-blende-type semiconductors," *Phys. Rev. B*, vol. 11, no. B, p. 3006, 1975.
- [61] D. J. Dugdale, S. Brand, and R. A. Abram, "Direct calculation of k·p parameters for wurtzite AlN, GaN, and InN," *Phys. Rev. B*, vol. 61, p. 12933, 2000.

- [62] Z. Yang and Z. Xu, “Electronic and optical properties of unstrained and strained wurtzite GaN,” *Phys. Rev. B*, vol. 54, p. 17577, 1996.
- [63] D. Vogel, P. Kruger, and J. Pollmann, “Structural and electronic properties of group-III nitrides,” *Phys. Rev. B*, vol. 55, p. 12836, 1997.
- [64] D. E. Boucher, G. G. DeLeo, and W. B. Fowler, “Simulations of GaN using an environment-dependent empirical tight-binding model,” *Phys. Rev. B*, vol. 59, p. 10064, 1999.
- [65] J. Wu, W. Walukiewicz, K. M. Yu, J. W. Ager, E. E. Haller, H. Lu, W. J. Schaff, Y. Saito, and Y. Nanishi, “Unusual properties of the fundamental band gap of InN,” *Appl. Phys. Lett.*, vol. 80, no. 21, p. 3967, 2002.
- [66] V. Y. Davydov, A. A. Klochikhin, V. V. Emtsev, S. V. Ivanov, V. A. Vekchin, F. Bechsted, J. Furthmuller, J. Aderhold, J. Graul, A. V. Mudryi, H. Harima, A. Hashimoto, Y. Yamamoto, and E. E. Haller, “Raman Spectroscopy as a Tool for Characterization of Strained Hexagonal GaN/Al<sub>x</sub>Ga<sub>1-x</sub>N Superlattices,” *Phys. Status Solidi*, vol. 234, p. 787, 2002.
- [67] D. Alexandrov, “Excitons of the structure in wurtzite InGaN and their properties,” *J. Cryst. Growth*, vol. 246, pp. 325–340, 2002.
- [68] F. London and F. Zeit, “No Title,” *J. Phys.*, vol. 42, p. 375, 1927.
- [69] L. O’Raifeartaigh, *The Dawning of Gauge Theory*, Part I. Princeton: Princeton University Press, 1997.
- [70] W. A. Harrison, *Electronic Structure and the Properties of Solids*. Dover Publishing Incorporated, 1989.
- [71] O. K. Andersen, “Simple approach to the band-structure problem,” *Solid State Commun.*, vol. 13, p. 133, 1973.
- [72] O. K. Andersen, W. Klose, and H. Nohl, “Electronic structure of Chevrel-phase high-critical-field superconductors,” *Phys. Rev. B*, vol. 17, p. 1209, 1978.
- [73] F. Herman and B. Skillman, *Atomic Structure Calculations*. Prentice Hall, 1963.
- [74] L. D. Landau and E. M. Lifshitz, *Quantum Mechanics (Non-Relativistic Theory)*, 2nd ed. Oxford: Pergamon Press, 1965.

## Chapter 10

### List of Publications

P. W. Binsted, K. S. A. Butcher, D. Alexandrov, P. Terziyska, D. Georgieva, R. Gergova, and V. Georgiev, "InN on GaN Heterostructure Growth by Migration Enhanced Epitaxial Afterglow (MEAglow)," *MRS Proc.*, vol. 1396, Jan. 2012.

K. S. A. Butcher, D. Alexandrov, P. Terziyska, V. Georgiev, D. Georgieva, and P. W. Binsted, "InN grown by migration enhanced afterglow (MEAglow)," *Phys. Status Solidi*, vol. 209, no. 1, pp. 41–44, Jan. 2012.

K. S. A. Butcher, B. W. Kemp, I. B. Hristov, P. Terziyska, P. W. Binsted, and D. Alexandrov, "Gallium Nitride Film Growth Using a Plasma Based Migration Enhanced Afterglow Chemical Vapor Deposition System," *Jpn. J. Appl. Phys.*, vol. 51, no. 1, p. 01AF02, Jan. 2012.

P. W. Binsted, D. Alexandrov, K. S. A. Butcher, R. Gergova, D. R. Oliver, M. McClarty, and I. Yahyaie, "Gallium nitride on indium nitride heterostructure growth by migration enhanced afterglow (MEAglow) (submitted only)," *Phys. Status Solidi*, 2013.

K. S. A. Butcher, R. Gergova, V. Georgiev, D. Georgieva, P. W. Binsted, G. Togtema, and D. Alexandrov, "Using the Moss - Burstein effect to induce the condition of semiconductor transparency for super - luminescent InGaN," *Phys. Status Solidi*, 2013.

P. T. Terziyska, K. S. A. Butcher, D. Gogova, D. Alexandrov, P. W. Binsted, G. Wu, K. Scott, and A. Butcher, "InN nanopillars grown from In-rich conditions by migration enhanced afterglow technique," *Mater. Lett.*, vol. 106, pp. 155–157, May 2013.

R. Gergova, K. S. A. Butcher, P. W. Binsted, and D. Gogova, "Initial results for epitaxial growth of InN on gallium oxide and improved Migration-Enhanced Afterglow Epitaxy growth on gallium nitride," *J. Vac. Sci. Technol. B Microelectron. Nanom. Struct.*, vol. 32, no. 3, p. 031207, May 2014.

# Chapter 11

## Appendix

### 11.1. Sample Loading Procedure

Samples must be carefully loaded into the system to prevent atmospheric contamination as well as prevent sudden changes in pressure within the system.

1. Verify that the RGA gate valve (automatic) is closed.
2. Verify that the two (2) RHEED gate valves (manual) are closed.
3. Verify that the load lock to turbo pump gate valve is closed. (manual)
4. Clean the substrate holder.
5. Load substrate onto sample holder in load lock chamber and close lid.
6. Close bottom (turbo) manual valve.
7. Open top (load lock) manual valve.
8. Watch load lock chamber pressure drop to approx.
9. Close top (load lock) manual valve.
10. Open bottom (turbo pump) manual valve.
11. Open load lock to turbo pump manual gate valve.
12. Watch load lock chamber pressure drop further.
13. Open load lock to chamber gate valve.
14. Verify transfer arm is at top position. Transfer sample into chamber using transfer arm. Carefully rotate to drop sample holder onto chamber pedestal. Retract arm.
15. Close load lock to chamber gate valve.

## 11.2. Sample Unloading Procedure

1. Disable plasma.
2. Disable heater.
3. Wait for system to cool.
4. Disable rotation.
5. Open load lock to chamber gate valve.
6. Verify arm is at top position, push in, rotate , withdraw arm.
7. Close load lock to chamber gate valve.
8. Close load lock to turbo manual gate valve.
9. Close bottom (turbo pump) manual valve.
10. Open top (load lock) manual valve.
11. Turn green knob to induce nitrogen into the chamber.
12. When hatch makes noise, it's ok to remove. Turn off green knob.
13. Close top valve, open bottom. (turbo one should be open when possible)
14. Wait for it to cool.

### 11.3. Sample Baking Procedure

Sample baking is used to burn off the oxide which forms naturally when the sample has been exposed to air for some time. This procedure is used to improve subsequent film growths on that sample, or to improve results from various analysis techniques. This procedure may also be used to prepare substrates prior to film growth. The MEAgrow reactor is used for sample baking.

1. Verify that the RF power supply and associated matching network are turned on.
2. Verify that the heater power supply is on.
3. Load the sample or substrate into chamber. Refer to the Sample Loading Procedure herein.
4. Set the heater for            and enable.
5. Enable substrate rotation at            .
6. Enable Nitrogen flow at            .
7. Allow the system to reach the heater set point and remain on for at least 1 hour prior to reversing the procedure.

## 11.4. Chamber Cleaning

There are many cases in which the system chamber must be cleaned prior to growth to prevent contamination during subsequent film growth. This is particularly important in the case where an indium nitride, or indium gallium nitride film growth has occurred previously due to the nature of indium. It is also important when one cannot be sure what the system had previously been used to grow.

1. Verify that the RF power supply and associated matching network are turned on.
2. Verify that the heater power supply is on.
3. Verify that the RGA gate valve is closed.
4. Verify that the RHEED gate valves are closed.
5. Clean sample holder with ethanol.
6. Load sample holder into chamber without sample. See Sample Loading Procedure herein.
7. Close chamber load lock gate valve.
8. Enable heat ( ).
9. Enable rotation ( ).
10. Enable Nitrogen at .
11. Enable RF power supply at (maximum).
12. Allow the system to reach the heater set point and remain on for at least 1 hour prior to reversing the procedure.
13. The RGA may be used to observe the contamination within the system during cleaning.

## **11.5. Procedure for Use of RGA During Growth**

The RGA is a powerful tool for assistance in film growth and leak detection. Care must be taken to prepare the system for RGA operation in order to reduce damage to the delicate filament used in the RGA system.

1. Close RGA automatic gate valve.
2. Turn on RGA master power switch.
3. Open manual valve on RGA sample line.
4. Turn on filament in software.
5. Format axis etc. in software.
6. Click on “go” in software.

## **11.6. Procedures for Using RHEED System**

### **11.6.1. Turning on RHEED system.**

1. Wait until process is complete. Leave sample in system.
2. Check RHEED power supply knobs to make sure they are at (Voltage and Current).
3. Turn on RHEED power supply.
4. Turn up voltage slowly to .
5. Turn up current slowly to .
6. Open both manual gate valves.
7. Turn off lights, walk around to display area.
8. Turn off beam blanking, screen should be green.
9. Rotate sample manually while adjusting RHEED parameters to get a clear image.

### **11.6.2. Putting on Standby**

1. Enable beam blanking.
2. Close both manual gate valves.
3. Turn current down to .

### **11.6.3. Taking off Standby**

1. Turn current up to .
2. Open both gate valves.
3. Turn off lights, walk around to display area.
4. Turn off beam blanking, screen should be green.
5. Rotate sample manually while adjusting RHEED parameters to get a clear image.

### **11.6.4. Turning off RHEED system**

1. Enable beam blanking.
2. Close both manual gate valves.
3. Lower current slowly to .
4. Lower voltage slowly to .
5. Turn off power.

## 11.7. Sample Etching

Sample etching is critical in obtaining high quality films.

It is of paramount importance to put on lab coat and gloves, and eye protection. All lab safety precautions must be followed.

1. Rinse a 250mL beaker very thoroughly as it may have had an acid or solvent in it.
2. Add chemicals to beaker in order:
  - a. (3 parts) distilled water
  - b. (1 part)
  - c. (1 part)
3. Rinse out and put some distilled water in the white plastic beaker for rinsing.
4. Clear fume hood and plug in stirring machine.
5. Place beaker on stirring machine.
6. Drop magnetic stirrer into beaker.
7. Place sample in beaker film side up.
8. Turn on stirrer set for to .
9. Wait to minutes.
10. Take out sample and rinse.
11. Add baking soda slowly to neutralize solution. Check with pH paper. Put in appropriate container.

### Important Notes

Don't mix solvents and acids, they explode.

Pour chemicals into beaker under fume hood.

Use plastic tweezers.

Don't pour waste into glass bottles which contain unknown contents.